# Colloidal Magnetic Fluids as Extractants for Chemical Processing Applications

by

Geoffrey D. Moeser

B.Sc. Eng. Chem., Queen's University, Kingston, ON, Canada (1998)

M.S.C.E.P. Chem. Eng., Massachusetts Institute of Technology, Cambridge, MA (2000)

*Submitted to the Department of Chemical Engineering in partial fulfillment of the requirements for the degree of*

Doctor of Philosophy

at the
Massachusetts Institute of Technology
September 2003





Signature of Author..... .....
Department of Chemical Engineering
August 22, 2003

Certified by.....
T. Alan Hatton
Ralph Landau Professor of Chemical Engineering Practice
Thesis Supervisor

Certified by.....
William H. Green, Jr.
Texaco-Mangelsdorf Assistant Professor of Chemical Engineering
Thesis Supervisor

Certified by.....
Paul E. Laibinis
Associate Professor of Chemical Engineering, Rice University
Thesis Supervisor

Accepted by.....
Daniel Blankschtein
Professor of Chemical Engineering
Chairman, Committee for Graduate Students

# Colloidal Magnetic Fluids as Extractants for Chemical Processing Applications

by

Geoffrey D. Moeser

Submitted to the Department of Chemical Engineering on August 22, 2003,
in partial fulfillment of the requirements for the degree of
Doctor of Philosophy in Chemical Engineering

## Abstract

This focus of this thesis is a novel class of water-based magnetic fluids that are specifically tailored to extract soluble organic compounds from water. Magnetic fluids are colloidal dispersions of magnetic nanoparticles that do not settle in gravitational or moderate magnetic fields due to their small size and do not aggregate because of their surface coatings. These materials offer several potential advantages over traditional methods of organic separation, such as activated carbon adsorption. For example, magnetic fluids possess a large surface area for separation while avoiding porous structures that introduce a high mass transfer resistance.

The magnetic fluids were prepared by precipitation and consist of a suspension of ~7.5 nm diameter magnetite ($Fe_3O_4$) nanoparticles coated with a ~9 nm thick bifunctional polymer layer comprised of an outer hydrophilic polyethylene oxide (PEO) region for colloidal stability, and an inner hydrophobic polypropylene oxide (PPO) region for solubilization of organic compounds. Characterization of these materials revealed the particle dimensions and magnetic properties. In addition, we examined the colloidal stability of the magnetic fluids over a broad range of conditions. The structure of the polymer shell, which was examined with neutron scattering and lattice calculations, shows some evidence of segregation of the PEO and PPO chains. The magnetic fluids exhibit a high capacity for organic solutes, with partition coefficients between the polymer coating and water on the order of $10^3$ to $10^5$, which is consistent with values reported for solubilization of these organics in PEO-PPO-PEO block copolymer (Pluronic) micelles.

The feasibility of using high gradient magnetic separation (HGMS) to separate the $Fe_3O_4$ nanoparticles was studied in this work. We present a general model for nanoparticle capture based on calculating the limit of static nanoparticle buildup around the collection wires in an HGMS column. Model predictions were compared successfully with experimental results from a bench-scale HGMS column. Permanent capture of individual nanoparticles is limited by diffusion away from the wires; however, 60-125 nm aggregates of particles can be captured permanently in the bench-scale column. The model provided estimates of the minimum particle size for permanent capture of individual nanoparticles and nanoparticle aggregates.

Thesis Supervisor: T. Alan Hatton
Title: Ralph Landau Professor of Chemical Engineering Practice

Thesis Supervisor: William H. Green, Jr.
Title: Texaco-Mangelsdorf Assistant Professor of Chemical Engineering

Thesis Supervisor: Paul E. Laibinis
Title: Associate Professor of Chemical Engineering, Rice University

# Acknowledgements

I would first like to sincerely thank my advisors Alan Hatton, Paul Laibinis, and Bill Green for all of their guidance during my time at MIT. Without their ideas, advice, suggestions, and support, this project would never have been completed. I also want to thank them for the independence that I was allowed, as I believe it made me a much better researcher. The final direction of this project was not what we anticipated when we began, but I hope and think that this work will stand as a useful contribution to those who follow. I would also like to thank my thesis committee members, Professors Tester and Hammond, for all of their contributions during my committee meetings. Your opinions came from a different viewpoint and were extremely useful in shaping the direction of the project.

I also need to thank all of the people who helped me in conducting the experimental work in this thesis. Without a doubt, the most important of these was Kaitlin Roach, who during her three years in the UROP program became an excellent researcher and certainly contributed more to this work than anyone. Her enthusiasm and tireless effort will be greatly missed. In addition, I would like to thank those researchers who assisted me, including Mike Frongillo and Fangcheng Chou of the MIT CMSE, Steve Kline and John Barker of NIST, MD, Paul Johnson of the University of Rhode Island, Monique Dubois of CEA, France, and Per Linse of the University of Lund. It goes without saying that I need to thank Hatton group members past and present for their help. In particular, I need to thank Lifen Shen and Seif-Eddeen Fateen for sharing their knowledge of magnetic fluids with me in the early stages, Tim Finegan for keeping the computers and lab running smoothly, and Sonja Sharpe for being an understanding cubicle neighbor. In addition, this department would not and will not function without people like Carol Phillips, Arline Benford, Beth Tuths, and Susan Lanza. I must also say thanks to all of my friends in the department with whom I shared everything from party planning to White Mountain hikes.

Without my family I wouldn't be here (literally!), so I would like to thank my parents Cathy and Doug Moeser for their unrelenting emotional and financial support for so many years. I'd also like to thank my brother Andrew Moeser for his inspiring way of living life, even if we don't see each other enough. Thanks also to Ethel-Rose and Edward Steinberger for always treating me like a party of your family, even if I technically wasn't for a very long time.

A final thank you goes to my fiancée Stacie Steinberger, for the incredible support throughout the last ten years, but particularly for the last five years, when we lived together, but when it sometimes seemed like all we shared was the same mailing address and a very needy cat. Without your support, I would never have been able to make it to this point.

# Table of Contents

# List of Figures

# List of Tables

# Chapter 1

# Introduction

## 1.1 Motivation and Approach

Synthetic organic compounds are common contaminants in both plant wastewater and drinking water, and must be removed before the water can be discharged or consumed. These contaminants include volatile organic compounds such as toluene and dichlorobenzene, as well as non-volatile compounds like polyaromatic hydrocarbons (PAH) and polychlorinated biphenyls (PCB). Organic compounds can enter drinking water supplies through leaking underground tanks, agricultural and urban runoff, or improperly disposed waste.[1] In water, these species are often soluble in low concentration, making standard coagulation and sedimentation techniques ineffective. In addition, their extremely low concentration (1 ppb to 1 ppm)[1] makes traditional separation methods like distillation and solvent extraction infeasible.

The most commonly used techniques for the removal of synthetic organics from water are activated carbon adsorption and air stripping. While these techniques have been widely implemented, they have several drawbacks associated with them. One important limitation of activated carbon adsorption is the highly porous structure of the carbon beads, which leads to long contacting times because of the high mass transfer resistance.[2] Additional disadvantages include a high pressure drop across the bed, the possibility of bacterial growth in the carbon, the potential for clogging due to suspended solids, and the difficulty of regenerating activated carbon without degrading the porous structure.[2,3] Air stripping, which is only suitable for volatile organics, also suffers from clogging due to suspended solids and produces a contaminated air stream that must be either discharged or further treated.[3] Newer techniques for organic removal from water include oxidation with ozone[4] or UV radiation,[5] anaerobic microbial decomposition,[6] reverse osmosis,[7] and micellar separation.[8,9] These techniques have the potential to overcome many of the negative aspects of activated carbon adsorption. However, they present additional processing problems. Ozonolysis, for example, has high operating

costs associated with ozone production and in some cases the ozonolysis products are more toxic than the original organics.[4] Reverse osmosis processes are complicated by membrane fouling,[7] while micellar separation requires a complicated ultrafiltration process[9] or precise control of temperature and pH to form a dense surfactant phase.[8] As an alternative strategy, we have developed water-based magnetic fluids for organic extraction that could offer several advantages over traditional separation techniques.

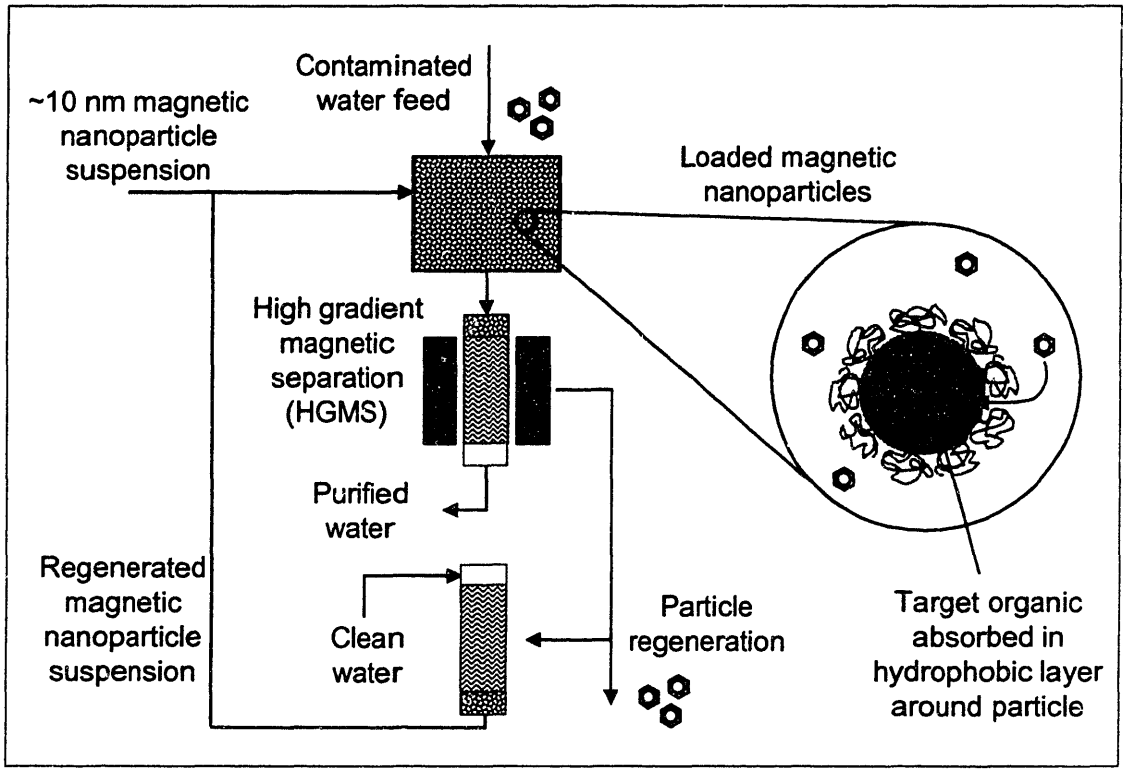


**Figure 1-1.** A process using functionalized magnetic nanoparticles as separation agents to remove organic compounds from water. After contacting the particles with a contaminated water stream, the organic-loaded particles are removed with high gradient magnetic separation. Following regeneration of the particles by removing the organics, the nanoparticles can be recycled to the contacting stage. Note that this figure is conceptual and features are not necessarily to scale.

Magnetic fluids, which are reviewed in detail in the next section, are stable colloidal dispersions of magnetic nanoparticles ~10 nm in diameter. Our magnetic fluids are water-based and consist of magnetite ($Fe_3O_4$) nanoparticles coated with a polymer that is specifically tailored to separate soluble organic compounds from water. This polymer coating consists of an outer hydrophilic region that provides colloidal stability in

water and an inner hydrophobic region that provides an extraction medium for organic compounds. Figure 1-1 illustrates conceptually how these magnetic fluids could be used in a separation process for dilute synthetic organic compounds. In the contacting stage, a concentrated suspension of the magnetic nanoparticles is added to a contaminated water stream, where the particles disperse and absorb organics in the hydrophobic part of their polymer coating. After the particles are loaded with the target organics, the suspension is passed through a high gradient magnetic separation (HGMS) column that traps the particles but allows purified water to flow through. When the HGMS column is saturated with particles, the magnetic field is removed and the particles are regenerated or disposed of.

Magnetic fluids offer several potential advantages for organic separation, many of which arise from the nanometer size of the particles. These materials provide very high surface area, even when the nanoparticles are dispersed at low volume fractions. For example, a 0.1 vol% suspension of 10 nm particles has an accessible surface area/solution volume ratio of $6 \times 10^5$ $m^2/m^3$, whereas 10 μm particles at the same volume fraction have an area of only $6 \times 10^2$ $m^2/m^3$. The high surface area of these nanoparticles is obtained without the incorporation of a porous structure like in activated carbon beads that also introduces a high mass transfer resistance. The result is that the kinetics of organic absorption will be rapid for the nanoparticles. For an organic diffusivity of $5 \times 10^{-10}$ $m^2/s$, a 0.1 vol% suspension of 10 nm particles has a characteristic diffusion time ($\sim R^2/D\phi^{2/3}$, where $R$ is the particle radius, $D$ is the solute diffusivity, and $\phi$ is the particle volume fraction) of 5 μs, while 10 μm particles at the same concentration have a characteristic diffusion time of 5 s. Thus, the transport-limiting process is the rate of dispersion of these nanoparticles in the separation mixture. Our proposed process in Figure 1-1 offers several additional advantages over traditional processes for organic removal. The relatively open structure of an HGMS column could allow suspended solids to be passed without clogging, whereas activated carbon requires that streams be clarified before processing.[3] An HGMS system can also be cycled rapidly on and off to regenerate the filter, while activated carbon requires a time-consuming thermal treatment that can degrade the porous structure.[2] As a result of the low mass transfer resistance of

the particles and ease of regeneration of the HGMS column, magnetic fluids could allow more rapid processing of contaminated streams than conventional fixed bed systems like activated carbon adsorption.

## 1.2 Background: Magnetic Fluids

### 1.2.1 Structure

Magnetic fluids, also known as ferrofluids, are colloidal dispersions of magnetic nanoparticles that do not settle in gravitational or moderate magnetic fields due to their small size and do not aggregate because of their surface coatings. The structure of a magnetic fluid is shown schematically in Figure 1-2. The nanoparticles can be either ferromagnetic materials such as iron or cobalt, or ferrimagnetic materials, the most common of which is magnetite ($Fe_3O_4$).[10] This compound is a spinel iron oxide species with a 2:1 molar ratio of Fe ions in their III and II oxidation states.[11] Magnetite is not

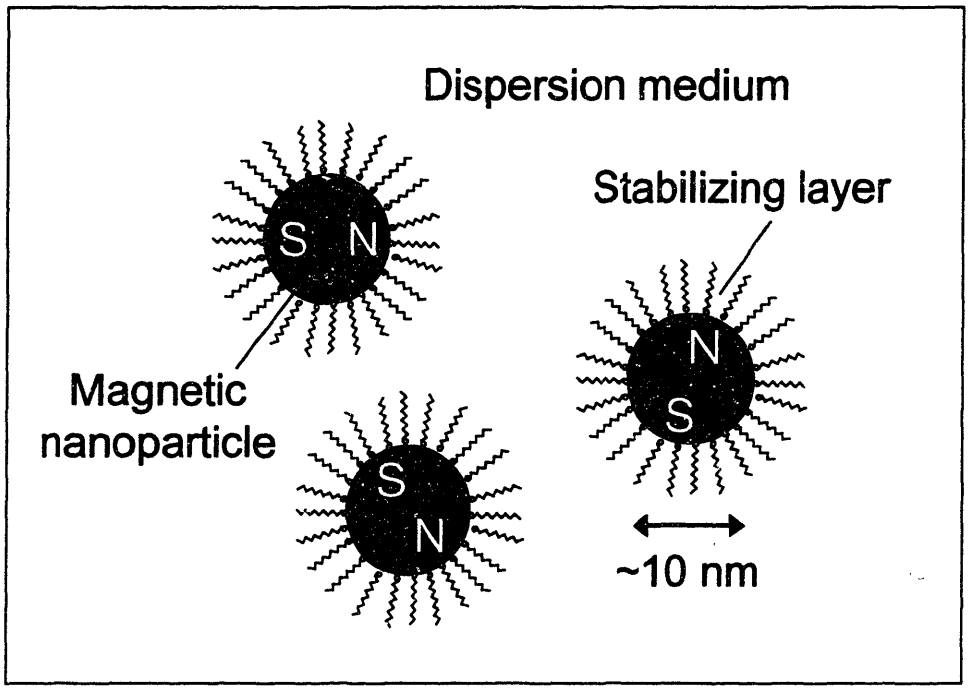


**Figure 1-2.** General structure of a magnetic fluid. Magnetic fluids consist of magnetic nanoparticles dispersed in a liquid medium, with a stabilizing layer around the particles to prevent flocculation. Each particle has a magnetic dipole but the suspension as a whole has zero net magnetization due to dipole fluctuations.

prone to oxidation, which is an advantage over magnetic fluids based on cobalt or iron nanoparticles, which tend to lose their magnetic properties over time.[12] The typical particle size is ~10 nm, which is sufficiently small to prevent sedimentation of the particles, as Brownian motion will dominate the gravitational force and the magnetic force from a typical handheld magnet for a particle of this size.[10]

Without a stabilizing layer, the ~10 nm particles in a magnetic fluid would rapidly flocculate due to the van der Waals attractive force that exists between particles in a dispersion medium and then settle. The van der Waals force is more important than interparticle magnetic attraction at short range for a moderately magnetic material like magnetite.[13] The role of the stabilizing layer is to prevent flocculation by exerting a repulsive force between particles at short range. The nature of the stabilizing layer depends on the dispersion medium. If the dispersion medium is a hydrocarbon, steric stabilization from an attached surfactant or polymer is typically used.[14] In an aqueous magnetic fluid, where water is the dispersion medium, steric stabilization, electrostatic stabilization, or a combination of both can be used to prevent the particles from agglomerating. Aqueous magnetic fluids with no physical stabilizing layer have been produced, but require careful control of the ionic strength and pH to maintain sufficient surface charge on the bare particles for electrostatic stabilization.[15] Stabilizing agents for electrostatic stabilization must possess functional groups that are ionized at the pH of the magnetic fluid, while stabilizing agents for steric stabilization must be sufficiently well solvated by the dispersion medium to induce repulsive interactions when the stabilizing layers of two particles overlap. In addition, all stabilizing polymers or surfactants require a means of attachment to the nanoparticles. In some cases, the stabilizer is attached physically with a moiety that is insoluble in the dispersion medium. For example, block copolymers that contain a soluble block for steric stabilization and an insoluble block for physical attachment have been used successfully to stabilize magnetic fluids.[12,16] A far more common method of stabilizer attachment to the particles is through the incorporation of a functional group that forms an electrostatic or covalent bond to the particle surface. For magnetite-based magnetic fluids, the most common functional group for attachment is carboxylic acid, which is known to form a strong *d*-orbital chelation to iron atoms on the magnetite surface,[17] as shown in Figure 1-3. This

attachment mechanism was used in the earliest magnetic fluids,[18,19] which consisted of fatty acid-stabilized magnetite nanoparticles in kerosene, where the carboxyl head group of the fatty acid attached to the magnetite surface and the alkyl tail provided steric stabilization.

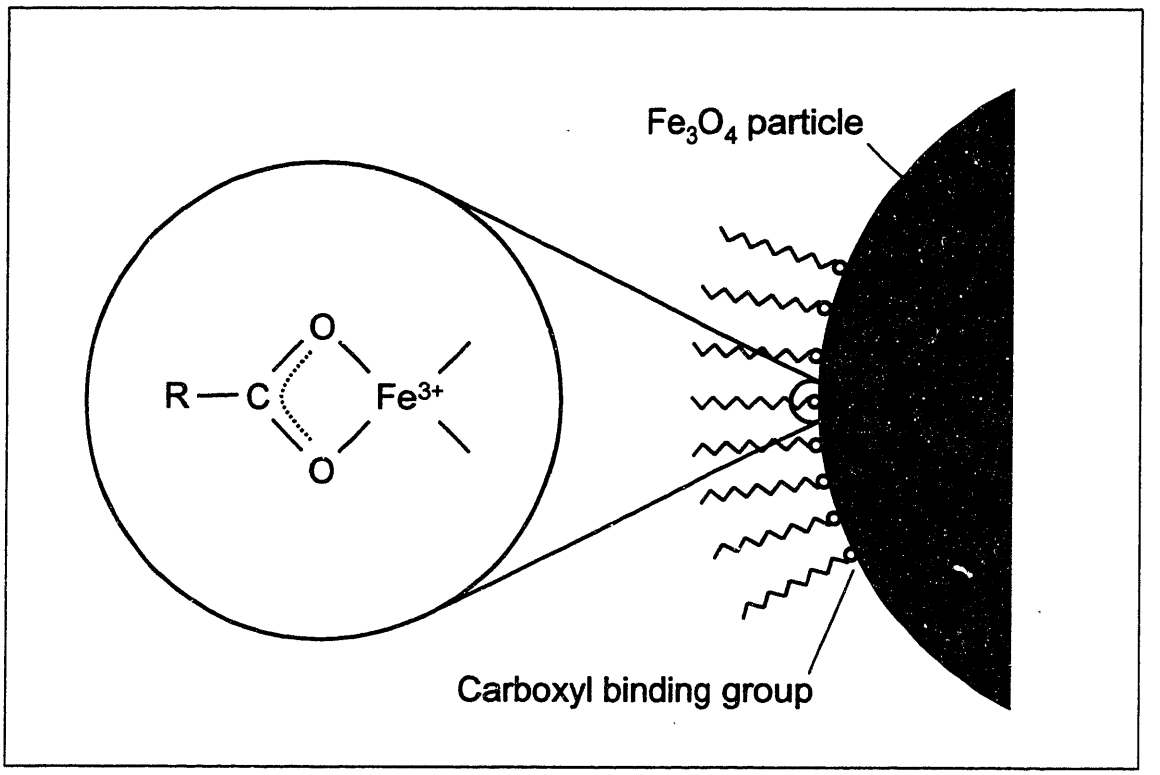


**Figure 1-3.** Attachment of carboxyl groups to the surface of a magnetite particle. The carboxyl group forms a chelate bidentate structure with surface iron atoms.[17]

Another important property of magnetic fluids is that the nanoparticles are sufficiently small to be single domain particles. The domain size of magnetite is ~25 nm,[20] which indicates that 10 nm particles are composed of a single crystal of magnetite, each having a permanent magnetic dipole similar to that of the bulk material. In a magnetic fluid, these dipoles are randomized due to either Brownian relaxation (particle rotation) or Néel relaxation (spontaneous fluctuation of the dipole direction within the particle). The dominant mechanism depends on the size of the particle.[10] Magnetic fluids exhibit superparamagnetism, in that they have approximately zero net magnetization in the absence of an applied field, but become strongly magnetized in an applied field due to alignment of the particle dipoles with the field.

## 1.2.2 Magnetic Fluid Synthesis

### 1.2.2.1 General Concepts

The synthesis of magnetic fluids requires two steps: formation of the nanoparticles and coating the nanoparticles with the stabilizing layer. Usually, the synthesis is performed in the eventual dispersion medium, but in some cases the nanoparticles are synthesized in one solvent and then transferred to another.[19] In addition, the synthesis of the nanoparticles is usually conducted in the presence of a stabilizing polymer or surfactant to prevent agglomeration during synthesis. This section reviews the three most common methods of magnetic fluid production, although it should be noted that other techniques such as spark erosion[21] and plasma generation[22] have been used to produce magnetic fluids.

### 1.2.2.2 Size Reduction

The oldest and most basic method of magnetic fluid synthesis is through size reduction. In this technique, bulk magnetic materials are ground in a ball mill with the dispersion medium and the stabilizing surfactant. The surfactant must be present during grinding to produce stable nanoparticles. Size reduction was first described by Papell,[18] who ground a 30 μm magnetite powder in heptane with oleic acid to produce a magnetic fluid with a final particle diameter of approximately 10 nm. The primary benefit of size reduction is that it is simple and flexible, in that any type of particle can be produced if a bulk powder is available.[10] However, size reduction is a time-consuming and energy intensive process, requiring approximately 1000 hours of grinding at 45 rpm in order to reduce the particles to the required dimension.[23]

### 1.2.2.3 Organometallic Decomposition

Magnetic fluids can also be prepared by thermal decomposition of organometallic compounds in an organic solvent.[12,24-27] In this technique, an organometallic compound and stabilizing surfactant are dissolved in a solvent and heated to an elevated temperature (approximately 200-300 °C, depending on the compound), at which point the organometallic species decomposes and the insoluble metal precipitates. The surfactant

binds to the particles just after nucleation, limiting the growth and forming nanoparticles. A variety of magnetic fluids have been produced by this method, including cobalt particles from dicobalt octacarbonyl,[12,26] iron particles from iron pentacarbonyl,[25] and magnetite particles from iron acetylacetonate[24] or iron pentacarbonyl followed by oxidation.[27] Magnetic fluids produced from organometallic decomposition tend to be nearly monodisperse, which is likely a result of the elevated temperature used in the synthesis. This method of particle synthesis cannot be performed in water due to the high temperatures and insolubility of the organometallic compounds; however, aqueous magnetic fluids can be produced by subsequently transferring the particles to water with a new stabilizing surfactant.

#### 1.2.2.4 Chemical Coprecipitation

A less energy intensive technique that is well suited for making aqueous magnetic fluids is the chemical coprecipitation of metal salts, which was first achieved by Reimers and Khallafalla.[19] This technique is limited to the production of ferrite particles, such as magnetite ($Fe_3O_4$),[19] maghemite ($\gamma$-$Fe_2O_3$),[15] or cobalt ferrite ($CoFe_2O_4$),[28] and is probably the most common method for preparing magnetic fluids due to its simplicity and relatively low cost. The discussion here is limited to magnetite nanoparticle formation, as it is the basis of the magnetic fluids used in this study and of most magnetic fluids in the literature.

Magnetite is formed by basic precipitation of an aqueous solution of iron (III) chloride and iron (II) chloride in a 2:1 molar ratio, forming a spinel structure of $Fe^{3+}$ and $Fe^{2+}$ ions that results in a net magnetic dipole.[11] Magnetite nanoparticles are formed when this reaction is conducted in the presence of a dissolved stabilizing surfactant or polymer that binds to the particles just after nucleation, limiting the growth of the particles to ~10 nm. The overall stoichiometry of this reaction is shown in Equation 1-1, for the case where ammonium hydroxide is used as the precipitating agent.

$$2\,FeCl_3 + FeCl_2 + 8\,NH_4OH \rightarrow Fe_3O_4 + 8\,NH_4Cl + 4\,H_2O \qquad (1\text{-}1)$$

The base is usually added in excess so that the pH of the reaction medium is strongly basic (pH of 12-14). The size, composition, and magnetization of the nanoparticles are affected by the reagent concentrations, stabilizer concentration, temperature, and pH during synthesis.[29-33] The optimal reaction temperature for the formation of magnetite is generally thought to be approximately 80 °C,[32,33] although magnetite formation at room temperature has also been reported.[34]

## 1.2.3 Applications of Magnetic Fluids

### 1.2.3.1 Industrial Applications

Magnetic fluids have found commercial use in a variety of industrial applications. These applications usually take advantage of the magnetic properties of the bulk liquids, as opposed to the particular chemistry of the stabilizing layer. Three industrial applications in which magnetic fluids have found the most commercial success are sealing, damping, and heat transfer.[35] Magnetic fluids are commonly used as rotary shaft seals in hard drives because they provide a means of preventing gas leakage while avoiding rubber parts. In this application, rings of magnetic fluid are held in place around the shaft with external magnets that form a high pressure gas barrier.[14] Likewise, a film of magnetic fluid held in place with an external magnet is used in place of an oil film in stepper motors to damp vibrations and oscillations as the motor moves.[35] The damping properties of magnetic fluids are also used in loudspeakers,[36] where they also act as an improved coolant fluid due to their high thermal conductivity and their development of magnetically-driven convection cells in the presence of a magnetic field.[10] The magnetic fluids used in these industrial applications are usually organic-based.[35] A relatively new application is the use of cobalt-based magnetic fluids to increase microwave absorption in the heating of nonpolar systems.[26]

### 1.2.3.2 Biomedical Applications

Aqueous magnetic fluids have the potential to be used in a range of biomedical applications, in which the nanoparticles generally require a coating that provides colloidal stability in the body and is biocompatible. Magnetic fluids with biocompatible stabilizing polymers have been developed as magnetic resonance imaging (MRI) contrast

agents that have improved imaging properties in the body compared to conventional ferric salt solutions.[37,38] Magnetic fluids have also been used in drug delivery applications, which requires the absorption or covalent attachment of drugs to the nanoparticles.[39,40] Anti-cancer drugs absorbed on the stabilizing layer of magnetite nanoparticles have been directed *in vivo* to a tumor by applying an external magnetic field to concentrate the magnetic fluid in the affected area.[39] Magnetite particles with attached monoclonal antibodies have also been developed that are able to simultaneously deliver the antibody and generate heat by applying an alternating magnetic field to the particles.[40]

#### 1.2.3.3 Biological Separations

Magnetic fluids (or suspensions of submicron magnetic particles) have been applied to many different biological systems to separate cells[41] and proteins.[42-46] In most biological separation applications, the magnetic nanoparticles are used as tagging-agents for the biological species, which usually have a negligible magnetic moment. Cell separation with magnetic particles has been reviewed extensively by Safarik and Safarikova.[41] Most techniques for cell separation involve functionalizing the magnetic nanoparticles with ligands that bind reversibly to cells. When added to a fermentation broth, for example, the magnetic particles bind specifically to the target cells, which can then be removed by magnetic separation. In most cases, 1-5 μm polymer beads with imbedded nanoparticles, such as the commercial product Dynabeads, are used,[41] which are not technically magnetic fluids due to the large particle size. In some cases, magnetic fluids have been used in cell separations. For example, a magnetic fluid with functionalized maghemite nanoparticles has been used to separate erythrocyte cells.[47] The cells are many orders of magnitude larger than the nanoparticles and are therefore covered by many nanoparticles. Proteins, which are significantly smaller than the nanoparticles, can be separated with magnetic fluids on the basis of charge interactions[42,46] or specificity of ligands attached to the nanoparticles.[43-45] Recently, magnetic fluids based on phospholipid-coated magnetite nanoparticles have been produced that are capable of protein loadings as high as 1200 mg/cm$^3$ of particles.[42] The

magnetic separation of biological products remains an extremely active area of research due to the high value of these compounds.

### 1.2.3.4 Environmental Separations

Several techniques involving magnetic particles for environmental separations have been proposed and demonstrated at the research level.[48-52] Usually, these processes use micron-sized particles composed of magnetite (or composites of magnetite and other materials) that are used as magnetic tagging agents by coating them with a selective adsorbent for targeted solutes, such as radionuclides,[48] heavy metal ions,[49] or water-soluble organic dyes.[50,51] Other techniques include using highly porous magnetic beads that are effective in removing metal ions from water[52] and using charged magnetic particles that aggregate with bacteria and solids to purify wastewater.[53] Environmental separations with true magnetic fluids (i.e. suspensions of individually dispersed magnetic nanoparticles) have not generally been a focus of previous research but are the goal of this thesis.[54]

### 1.2.3.5 Magnetophoretic Separations with Magnetic Fluids

In magnetophoretic separations, a magnetic fluid is used to exert body forces on nonmagnetic particles in order to separate them on the basis of size or density. This approach is different from the biological and environmental separations discussed in the previous sections, in which the magnetic particles serve as tagging agents. This process, also known as magnetoflotation, has been used to separate coal particles of different densities by suspending the particles in a magnetic fluid and applying a vertical magnet field gradient.[55] The field gradient causes the particles to experience a body force that acts opposite to gravity, changing the effective density of the fluid. By changing the magnetic field gradient, the effective fluid density can be set between the density of two types of particles, causing one to float and the other to sink.[55] Recently, this concept has been extended to cell separations.[56] By suspending nonmagnetic cells in a magnetic fluid, the cells can be driven against a magnetic field gradient; transport is opposed by the drag force on the cells, allowing sorting based on the cell size.[56]

## 1.3 Background: Magnetic Separation

### 1.3.1 Types of Magnetic Separation

Magnetocollection, the most common form of magnetic separation, involves the application of a magnetic field gradient that causes magnetic material to move toward a region of higher field strength, thereby allowing the magnetic material to be separated from a nonmagnetic medium.[57] Originally, magnetocollection was applied in the mineral industry[57] for the removal of desired magnetic materials, such as iron ore, from waste rock, or for the removal of magnetic contaminants from nonmagnetic minerals. An example of the latter case is kaolin clay purification, in which dark iron and titanium-containing minerals are removed magnetically from kaolin by magnetic separation.[58]

More recently, many other types of magnetic separation have been developed at the research and commercial level. A comprehensive review of the different types of magnetic separation is given by Moffat et al.[57] Some of these techniques, such as magnetoflotation and magnetic tagging, involve magnetic fluids and were discussed in Section 1.2.3. Examples of other types of magnetic separation include magnetoflocculation,[57] in which a magnetic field causes magnetic particles to form aggregates that then settle under gravity, and magnetoanisotropic sorting,[57] in which a magnetic field is used to orient an array of magnetic particles that allows separation of molecules, such as DNA,[59] based on size or shape.

### 1.3.2 High Gradient Magnetic Separation

Magnetocollection becomes increasingly difficult as the particle size or magnetic susceptibility decreases. Typical magnetocollection devices, such as drum separators, are unable to separate particles less than approximately 75 μm in size efficiently from a liquid medium.[58] High gradient magnetic separation (HGMS) has been developed as an effective method of separating small and weakly magnetic particles. A number of commercial HGMS systems have been developed and are currently used in a broad range of applications, including kaolin clay purification, the separation of metallic particles

from waste streams in steel and power plants, iron ore recovery, and water treatment (through magnetic seeding).[53,58]

An HGMS system generally consists of a column packed with a bed of magnetically susceptible wires (~50 μm diameter) that is placed inside an electromagnet. When a magnetic field is applied across the column, the wires dehomogenize the magnetic field in the column, producing large field gradients around the wires that attract magnetic particles to the surfaces of the wires and trap them there.[58] The collection of particles depends strongly on the creation of these large magnetic field gradients, as well as the particle size and magnetic properties, as shown by the equation for the magnetic force on a particle in an applied field:[58]

$$\mathbf{F_m} = \mu_o V_p \mathbf{M_p} \cdot \nabla \mathbf{H} \qquad (1\text{-}2)$$

where $\mu_o$ is the permeability of free space, $V_p$ is the volume of the particle, $\mathbf{M_p}$ is the magnetization of the particle, and $\mathbf{H}$ is the magnetic field at the location of the particle. For successful collection of magnetic particles by HGMS, the magnetic force attracting particles towards the wires must be dominant compared to the fluid drag, gravitational, inertial, and diffusional forces as the particle suspension flows through the separator.[58] HGMS is a good candidate for separating magnetic nanoparticles from a magnetic fluid because of the strong magnetic field gradients that are needed to overcome the diffusional forces that are significant because of the small particle size.

### 1.3.3 Magnetic Fluids and HGMS

In this work, HGMS was used to remove magnetic nanoparticles from a magnetic fluid. Typically, HGMS has been used to separate micron-scale or larger particles or aggregates. When magnetic nanoparticles have been used as separation agents, the nanoparticles have usually been present as micron-scale aggregates[43] or encapsulated into larger polymer beads.[52] The larger volume of these particles makes magnetic collection by HGMS (or other means) relatively straightforward. The application of HGMS to suspensions of individually dispersed magnetic nanoparticles has been studied in much less depth.

Several experimental studies on high gradient magnetic separation of magnetic fluids have been performed. However, the majority of these studies used HGMS to fractionate the nanoparticles based on size[60-62] or to remove large aggregates from magnetic fluids as a quality control step.[63] While a number of studies have investigated the use of HGMS to separate individually dispersed magnetic nanoparticles, the majority of this work has been purely theoretical and limited to simulating the behavior of nanoparticles around a single magnetized collection wire[64-66] or sphere.[67-69] Recently, simulations of magnetic nanoparticles in a three-dimensional array of magnetized collection spheres have been performed.[70] These theoretical studies have suggested that the collection of magnetic nanoparticles by HGMS may be possible but the small size of the particles presents challenges due to nanoparticle diffusion. Recently, theoretical predictions of submicron particle capture have been compared with experimental results, but diffusion was neglected as the minimum particle size considered was approximately 100 nm.[71]

## 1.4 Research Overview

The overall goals of this research were: i) to prepare magnetic fluids that could be used to separate organic compounds from water, ii) to characterize the structure, magnetic properties, and organic affinity of these materials, and iii) to demonstrate the feasibility of using high gradient magnetic separation to remove the nanoparticles from water. Chapter 2 details the preparation of the water-based magnetic fluids, including the method used to create the bifunctional polymer layer around the nanoparticles that provides both steric stabilization and a hydrophobic region for extraction. The particles were characterized in terms of their dimensions, magnetic properties, and colloidal stability. Chapter 3 contains a detailed study of the structure of the bifunctional polymer shell using small angle neutron scattering and self-consistent mean-field lattice calculations. The affinity of the nanoparticles for several model organics is presented in Chapter 4, where we also present a simple model for the organic solubility based on a linear free energy relationship. Chapter 5 contains a feasibility study on the use of HGMS for separating the nanoparticles from water that involves both modeling and

experimental data from a bench scale HGMS system. A brief discussion of using these magnetic fluids in a practical separation process is given in Chapter 6.

## 1.5 Bibliography


(1) Cohn, P. D.; Cox, M.; Berger, P. S. Health and Aesthetic Aspects of Water Quality. In *Water Quality and Treatment*, 5th ed.; Letterman, R. D., Ed.; McGraw-Hill: New York, 1999.

(2) Snoeyink, V. L.; Summers, R. S. Adsorption of Organic Compounds. In *Water Quality and Treatment*, 5th ed.; Letterman, R. D., Ed.; McGraw-Hill: New York, 1999.

(3) Smith, J. E. J.; Hegg, B. A.; Renner, R. C.; Bender, J. H. *Upgrading Existing or Designing New Drinking Water Treatment Facilities*; Noyes Data Corporation: Park Ridge, NJ, 1991; Vol. 198.

(4) Gottschalk, C.; Libra, J. A.; Saupe, A. *Ozonation of Water and Waste Water*; Wiley-VCH: Weinheim, Germany, 2000.

(5) Oppenlander, T. *Photochemical Purification of Water and Air*; Wiley-VCH: Weinheim, Germany, 2003.

(6) Speece, R. E. *Anaerobic Biotechnology for Industrial Wastewaters*; Archae Press: Nashville, TN, 1996.

(7) Eisenberg, T. N.; Middlebrooks, E. J. *Reverse Osmosis Treatment of Drinking Water*; Butterworths: Boston, MA, 1986.

(8) Gotlieb, I.; Bozzelli, J. W.; Gotlieb, E. Soil and Water Decontamination by Extraction with Surfactants. *Sep. Sci. Technol.* **1993**, *28*, 793-804.

(9) Hurter, P. N.; Hatton, T. A. Solubilization of Polycyclic Aromatic Hydrocarbons by Poly(ethylene oxide-propylene oxide) Block Copolymer Micelles: Effects of Polymer Structure. *Langmuir* **1992**, *8*, 1291-1299.

(10) Rosensweig, R. E. *Ferrohydrodynamics*; Dover Publications, Inc.: Mineola, NY, 1985.

(11) Gokon, N.; Shimada, A.; Kaneko, H.; Tamaura, Y.; Ito, K.; Ohara, T. Magnetic Coagulation and Reaction Rate for the Aqueous Ferrite Formation Reaction. *J. Magn. Magn. Mater.* **2002**, *238*, 47-55.

(12) Pathmamanoharan, C.; Philipse, A. P. Preparation and Properties of Monodisperse Magnetic Cobalt Colloids Grafted with Polyisobutene. *J. Colloid Interface Sci.* **1998**, *205*, 340-353.

(13) Shen, L. F.; Stachowiak, A.; Fateen, S. E. K.; Laibinis, P. E.; Hatton, T. A. Structure of Alkanoic Acid Stabilized Magnetic Fluids. A Small-Angle Neutron and Light Scattering Analysis. *Langmuir* **2001**, *17*, 288-299.

(14) Rosensweig, R. E. Magnetic Fluids: Phenomena and Process Applications. *Chem. Eng. Prog.* **1989**, *85*, 53-61.

(15) Massart, R.; Dubois, R.; Cabuil, V.; Hasmonay, E. Preparation and Properties of Monodisperse Magnetic Fluids. *J. Magn. Magn. Mater.* **1995**, *149*, 1-5.

(16) Elkafrawy, S.; Hoon, S. R.; Bissell, P. R.; Price, C. Polymeric Stabilization of Colloidal Magnetite Magnetic Fluids. *IEEE Trans. Magn.* **1990**, *26*, 1846-1848.

(17) Mikhailik, O. M.; Povstugar, V. I.; Mikhailova, S. S.; Lyakhovich, A. M.; Fedorenko, O. M.; Kurbatova, G. T.; Shklovskaya, N. I.; Chuiko, A. A. Surface Structure of Finely Dispersed Iron Powders. I. Formation of Stabilizing Coating. *Colloids Surf.* **1991**, *52*, 315-324.

(18) Papell, S. S. Low Viscosity Magnetic Fluid Obtained by the Collodial Suspension of Magnetic Particles. U.S. Patent 3,215,572, 1965.

(19) Reimers, G. W.; Khalafalla, S. E. "Preparing Magnetic Fluids by a Peptizing Method," Twin Cities Metallurgy Research Center, U.S. Department of the Interior, 1972.

(20) Lee, J.; Isobe, T.; Senna, M. Preparation of Ultrafine Fe3O4 Particles by Precipitation in the Presence of PVA at High pH. *J. Colloid Interface Sci.* **1996**, *177*, 490-494.

(21) Berkowitz, A. E.; Walter, J. L. Ferrofluids Prepared by Spark Erosion. *J. Magn. Magn. Mater.* **1983**, *30*, 75-78.

(22) Bica, I.; Muscutariu, I. Physical Methods in Obtaining the Ultrafine Powders for Magnetic Fluids Preparation. *Mater. Sci. Eng., B* **1996**, *B40*, 5-9.

(23) Berkowitz, A. E.; Lahut, J. A.; VanBuren, C. E. Properties of Magnetic Fluid Particles. *IEEE Trans. Magn.* **1980**, *16*, 184-190.

(24) Sun, S. H.; Zeng, H. Size-Controlled Synthesis of Magnetite Nanoparticles. *J. Am. Chem. Soc.* **2002**, *124*, 8204-8205.

(25) Park, S. J.; Kim, S.; Lee, S.; Khim, Z. G.; Char, K.; Hyeon, T. Synthesis and Magnetic Studies of Uniform Iron Nanorods and Nanospheres. *J. Am. Chem. Soc.* **2000**, *122*, 8581-8582.

(26) Holzwarth, A.; Lou, J. F.; Hatton, T. A.; Laibinis, P. E. Enhanced Microwave Heating of Nonpolar Solvents by Dispersed Magnetic Nanoparticles. *Ind. Eng. Chem. Res.* **1998**, *37*, 2701-2706.

(27) Kumar, R. V.; Koltypin, Y.; Cohen, Y. S.; Cohen, Y.; Aurbach, D.; Palchik, O.; Felner, I.; Gedanken, A. Preparation of Amorphous Magnetite Nanoparticles Embedded in Polyvinyl Alcohol using Ultrasound Radiation. *J. Mater. Chem.* **2000**, *10*, 1125-1129.

(28) Giri, A. K.; Pellerin, K.; Pongsaksawad, W.; Sorescu, M.; Majetich, S. A. Effect of Light on the Magnetic Properties of Cobalt Ferrite Nanoparticles. *IEEE Trans. Magn.* **2000**, *36*, 3029-3031.

(29) Feltin, N.; Pileni, M. P. New Technique for Synthesizing Iron Ferrite Magnetic Nanosized Particles. *Langmuir* **1997**, *13*, 3927-3933.

(30) Blums, E.; Cebers, A.; Maiorov, M. M. *Magnetic Fluids*; Walter de Gruyter and Co.: Berlin, Germany, 1996.

(31) Shimoiizaka, J. Method of Preparing a Water-Based Magnetic Fluid. U.S. Patent 4,094,804, 1978.

(32) Shen, L.; Laibinis, P. E.; Hatton, T. A. Bilayer Surfactant Stabilized Magnetic Fluids: Synthesis and Interactions at Interfaces. *Langmuir* **1999**, *15*, 447-453.

(33) Bica, D. Preparation of Magnetic Fluids for Various Applications. *Romanian Rep. Phys.* **1995**, *47*, 265-272.

(34) Cabuil, V.; Hochart, N.; Perzynski, R.; Lutz, P. J. Synthesis of Cyclohexane Magnetic Fluids Through Adsorption of End-functionalized Polymers on Magnetic Particles. *Prog. Colloid Polym. Sci.* **1994**, *97*, 71-74.

(35) Raj, K.; Moskowitz, B.; Casciari, R. Advances in Ferrofluid Technology. *J. Magn. Magn. Mater.* **1995**, *149*, 174-180.

(36) Raj, K.; Moskowitz, R. Commercial Applications of Ferrofluids. *J. Magn. Magn. Mater.* **1990**, *85*, 233-245.

(37) Kawaguchi, T.; Yoshino, A.; Hasegawa, M.; Hanaichi, T.; Maruno, S.; Adachi, N. Dextran-Magnetite Complex: Temperature Dependence of its NMR Relaxivity. *J. Mater. Sci. - Mater. Med.* **2002**, *13*, 113-117.

(38) Douglas, T.; Bulte, J. W. M.; Dickson, D. P. E.; Frankel, R. B.; Pankhurst, Q. A.; Moskowitz, B. M.; Mann, S. Inorganic-Protein Interactions in the Synthesis of a Ferrimagnetic Nanocomposite. In *Hybrid Organic-Inorganic Composites*; Mark, J. E., Lee, C. Y., Bianconi, P. A., Eds.; ACS-Oxford University Press: New York, 1995; Vol. 585, pp. 19-28.

(39) Lubbe, A. S.; Bergemann, C.; Brock, J.; McClure, D. G. Physiological Aspects in Magnetic Drug-Targeting. *J. Magn. Magn. Mater.* **1999**, *194*, 149-155.

(40) Suzuki, M.; Shinkai, M.; Kamihira, M.; Kobayashi, T. Preparation and Characteristics of Magnetite-Labeled Antibody with the Use of Poly(Ethylene Glycol) Derivatives. *Biotechnol. Appl. Biochem.* **1995**, *21*, 335-345.

(41) Safarik, I.; Safarikova, M. Use of Magnetic Techniques for the Isolation of Cells. *J. Chromatogr. B* **1999**, *722*, 33-53.

(42) Bucak, S.; Jones, D. J.; Laibinis, P. E.; Hatton, T. A. Protein Separations using Colloidal Magnetic Nanoparticles. *Biotechnol. Prog.* **2003**, *19*, 477-484.

(43) Hubbuch, J. J.; Thomas, O. R. T. High-gradient Magnetic Affinity Separation of Trypsin from Porcine Pancreatin. *Biotechnol. Bioeng.* **2002**, *79*, 301-313.

(44) Tong, X. D.; Xue, B.; Sun, Y. A Novel Magnetic Affinity Support for Protein Adsorption and Purification. *Biotechnol. Prog.* **2001**, *17*, 134-139.

(45) Khng, H. P.; Cunliffe, D.; Davies, S.; Turner, N. A.; Vulfson, E. N. The Synthesis of Sub-Micron Magnetic Particles and their Use for Preparative Purification of Proteins. *Biotechnol. Bioeng.* **1998**, *60*, 419-424.

(46) DeCuyper, M.; DeMeulenaer, B.; VanderMeeren, P.; Vanderdeelen, J. Catalytic Durability of Magnetoproteoliposomes Captured by High-Gradient Magnetic Forces in a Miniature Fixed-Bed Reactor. *Biotechnol. Bioeng.* **1996**, *49*, 654-658.

(47) Halbreich, A.; Roger, J.; Pons, J. N.; Geldwerth, D.; Da Silva, M. F.; Roudier, M.; Bacri, J. C. Biomedical Applications of Maghemite Ferrofluid. *Biochimie* **1998**, *80*, 379-390.

(48) Buchholz, B. A.; Nunez, L.; Vandegrift, G. F. Radiolysis and Hydrolysis of Magnetically Assisted Chemical Separation Particles. *Sep. Sci. Technol.* **1996**, *31*, 1933-1952.

(49) Kaminski, M. D.; Nunez, L. Extractant-Coated Magnetic Particles for Cobalt and Nickel Recovery from Acidic Solution. *J. Magn. Magn. Mater.* **1999**, *194*, 31-36.

(50) Safarik, I. Removal of Organic Polycyclic Compounds from Water Solutions with a Magnetic Chitosan Based Sorbent Bearing Copper Phthalocyanine Dye. *Water Res.* **1995**, *29*, 101-105.

(51) Safarik, I.; Safarikova, M. Copper Phthalocyanine Dye Immobilized on Magnetite Particles: An Efficient Adsorbent for Rapid Removal of Polycyclic Aromatic Compounds from Water Solutions and Suspensions. *Sep. Sci. Technol.* **1997**, *32*, 2385-2392.

(52) Leun, D.; Sengupta, A. K. Preparation and Characterization of Magnetically Active Polymeric Particles (MAPPs) for Complex Environmental Separations. *Environ. Sci. Technol.* **2000**, *34*, 3276-3282.

(53) Mitchell, R.; Bitton, G.; Oberteuffer, J. A. High Gradient Magnetic Filtration of Magnetic and Non-Magnetic Contaminants from Water. *Sep. Purif. Methods* **1975**, *4*, 267-303.

(54) Moeser, G. D.; Roach, K. A.; Green, W. H.; Laibinis, P. E.; Hatton, T. A. Water-Based Magnetic Fluids as Extractants for Synthetic Organic Compounds. *Ind. Eng. Chem. Res.* **2002**, *41*, 4739-4749.

(55) Fofana, M.; Klima, M. S. Use of a Magnetic Fluid Based Process for Coal Separations. *Miner. Metall. Process.* **1997**, *14*, 35-40.

(56) Fateen, S. E. K. Magnetophoretic Focusing of Submicron Particles Dispersed in a Polymer-Stabilized Magnetic Fluid. Ph.D. Thesis, Department of Chemical Engineering; Massachusetts Institute of Technology: Cambridge, MA, 2002.

(57) Moffat, G.; Williams, R. A.; Webb, C.; Stirling, R. Selective Separations in Environmental and Industrial-Processes Using Magnetic Carrier Technology. *Miner. Eng.* **1994**, *7*, 1039-1056.

(58) Gerber, R.; Birss, R. R. *High Gradient Magnetic Separation*; Research Studies Press: London, United Kingdom, 1983.

(59) Doyle, P. S.; Bibette, J.; Bancaud, A.; Viovy, J. L. Self-Assembled Magnetic Matrices for DNA Separation Chips. *Science* **2002**, *295*, 2237-2237.

(60) Rheinlander, T.; Kotitz, R.; Weitschies, W.; Semmler, W. Magnetic Fractionation of Magnetic Fluids. *J. Magn. Magn. Mater.* **2000**, *219*, 219-228.

(61) Rheinlander, T.; Kotitz, R.; Weitschies, W.; Semmler, W. Different Methods for the Fractionation of Magnetic Fluids. *Colloid Polym. Sci.* **2000**, *278*, 259-263.

(62) Kelland, D. R. Magnetic Separation of Nanoparticles. *IEEE Trans. Magn.* **1998**, *34*, 2123-2125.

(63) O'Grady, K.; Stewardson, H. R.; Chantrell, R. W.; Fletcher, D.; Unwin, D.; Parker, M. R. Magnetic Filtration of Ferrofluids. *IEEE Trans. Magn.* **1986**, *22*, 1134-1136.

(64) Takayasu, M.; Gerber, R.; Friedlaender, F. J. Magnetic Separation of Submicron Particles. *IEEE Trans. Magn.* **1983**, *19*, 2112-2114.

(65) Gerber, R.; Takayasu, M.; Friedlaender, F. J. Generalization of HGMS Theory: The Capture of Ultra-fine Particles. *IEEE Trans. Magn.* **1983**, *19*, 2115-2117.

(66) Fletcher, D. Fine Particle High Gradient Magnetic Entrapment. *IEEE Trans. Magn.* **1991**, *27*, 3655-3677.

(67) Moyer, C.; Natenapit, M.; Arajs, S. Magnetic Filtration of Particles in Laminar-Flow through a Bed of Spheres. *J. Magn. Magn. Mater.* **1984**, *44*, 99-104.

(68) Ebner, A. D.; Ritter, J. A.; Ploehn, H. J. Feasibility and Limitations of Nanolevel High Gradient Magnetic Separation. *Sep. Purif. Technol.* **1997**, *11*, 199-210.

(69) Cotten, G. B.; Eldredge, H. B. Nanolevel Magnetic Separation Model Considering Flow Limitations. *Sep. Sci. Technol.* **2002**, *37*, 3755-3779.

(70) Ebner, A. D.; Ploehn, H. J.; Ritter, J. A. Magnetic Field Orientation and Spatial Effects on the Retention of Paramagnetic Nanoparticles with Magnetite. *Sep. Sci. Technol.* **2002**, *37*, 3727-3753.

(71) Ying, T. Y.; Yiacoumi, S.; Tsouris, C. High-Gradient Magnetically Seeded Filtration. *Chem. Eng. Sci.* **2000**, *55*, 1101-1113.

# Chapter 2

# Magnetic Fluid Synthesis and Characterization

## 2.1 Introduction

The goal of this research was the synthesis of water-based magnetic fluids that are tailored to separate organic compounds from water. These magnetic fluids consist of an aqueous suspension of nanoparticles coated with a polymer shell that provides colloidal stability in water and a hydrophobic region for extraction. Our magnetic fluids have the potential to be used in tandem with high gradient magnetic separation as a novel method for separating small organic molecules from water. These materials offer many potential advantages over traditional methods of organic removal, such as activated carbon adsorption, because they offer an extremely large exposed surface area without requiring porous materials that introduce a high mass transfer resistance.

The synthesis of the aqueous magnetic fluids involved two specific tasks: precipitation of the nanoparticles and coating them with the desired polymer structure. We achieved both these goals in a single-step process by chemical coprecipitation of iron chlorides[1] in an aqueous solution of graft copolymer, as illustrated in Figure 2-1. The precipitation of $Fe^{3+}$ and $Fe^{2+}$ ions in a 2:1 ratio under appropriate basic conditions produces solid magnetite. The key to the formation of magnetite nanoparticles is the graft copolymer, which limits magnetite particle growth to approximately 10 nm. In this work, the graft copolymer contained a backbone composed of polyacrylic acid (PAA) and a mixture of polyethylene oxide (PEO) and polypropylene oxide (PPO) side chains. Shortly after nucleation, carboxylic acid groups along the PAA backbone coordinate to the particle surface, preventing further growth. The PEO and PPO side chains on the graft copolymer then form a shell around the particle. Since the PEO chains are longer and more hydrophilic, they should extend into the water, providing steric stabilization. The PPO chains, being shorter and more hydrophobic, are expected to collapse onto the particle surface, forming an inner PPO layer around the particle surface that provides an extraction medium for organic compounds in water. This chapter discusses

characterization of the magnetic fluids in terms of their dimensions, magnetic properties, and colloidal stability.

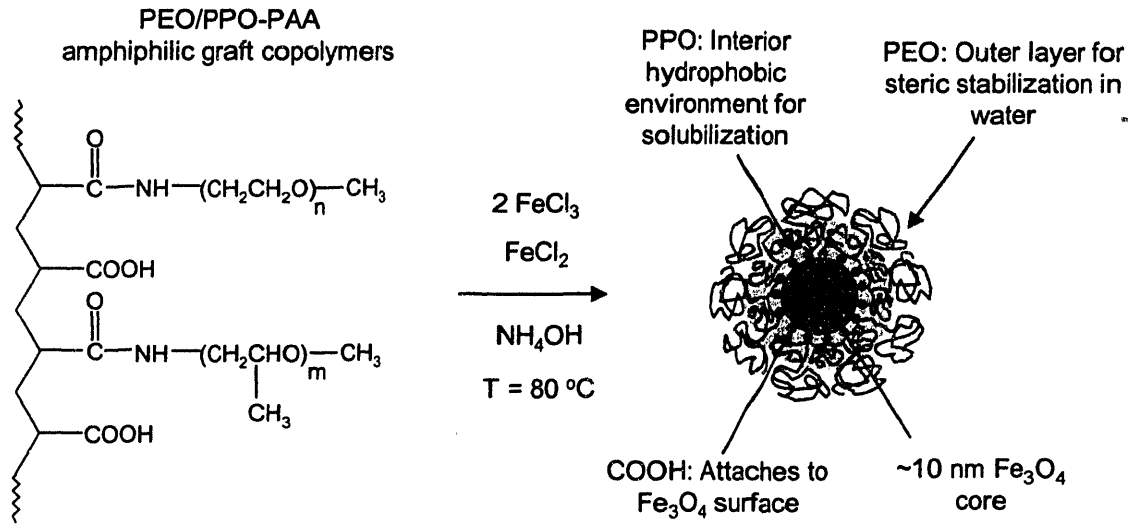


**Figure 2-1.** Aqueous magnetic fluid synthesis. The magnetic nanoparticles are produced by chemical coprecipitation of iron salts in an aqueous solution of the PEO/PPO-PAA graft copolymer. Soon after $Fe_3O_4$ nucleation begins, carboxylic acid groups on the polymer backbone bind to the particle surface, limiting particle growth and forming nanoparticles with a bifunctional polymer coating.

## 2.2 Experimental

### 2.2.1 Materials

Polyacrylic acid (50 wt% in water, $M_w$ = 5000), iron(III) chloride hexahydrate (97%), iron(II) chloride tetrahydrate (99%), and ammonium hydroxide (28 wt% in water) were obtained from Aldrich (Milwaukee, WI). Jeffamine XTJ-234 ($CH_3$-O-PEO/PPO-$NH_2$, EO:PO = 6.1:1, $M_w$ = 3000) and Jeffamine XTJ-507 ($CH_3$-O-PEO/PPO-$NH_2$, EO:PO = 1:6.5, $M_w$ = 2000) were obtained as gifts from Huntsman Corporation (Houston, TX). Magnesium sulfate and sodium chloride were obtained from Mallinckrodt Baker (Paris, KY). All chemicals were used as received.

The amino-terminated PEO and PPO polymers used in this work consisted of random copolymers of ethylene oxide (EO) and propylene oxide (PO) repeat units. XTJ-234 contained 6.1 EO units per PO unit, so its character is similar to that of a pure PEO

chain. The polymer designated XTJ-507 is a random copolymer with 6.5 PO units per EO unit. In this paper, we consider the polymers to be equivalent to pure PEO and PPO polymer chains and designate XTJ-234 as PEO-$NH_2$ and XTJ-507 as PPO-$NH_2$ for simplicity.

### 2.2.2 Polymer Synthesis

Graft copolymers were prepared by reacting polyacrylic acid (PAA) with amino-terminated PEO and PPO, as illustrated in Figure 2-2. This synthetic procedure is similar to that of Darwin et al.[2] for the production of polymers for hydraulic cement, and involves an amidation reaction to graft the amino-terminated chains to carboxylic acid groups on the PAA backbone. A series of polymers with varying numbers of PEO and PPO side chains was prepared with the following nomenclature used to describe the polymers: an *x/y* PEO/PPO polymer was a product in which *x*% of the carboxylic acid groups on the PAA were reacted with PEO-$NH_2$ chains and *y*% reacted with PPO-$NH_2$ chains. 16/0, 12/4, and 8/8 polymers were produced by varying the proportion of PAA,

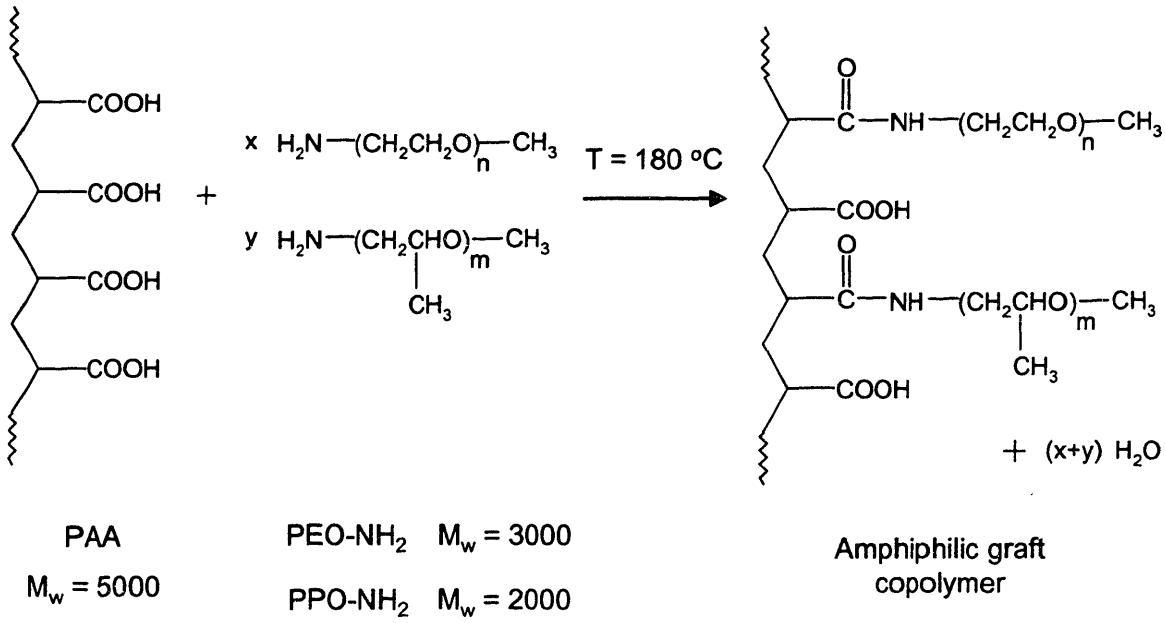


**Figure 2-2.** Amphiphilic graft copolymer synthesis. The graft copolymers are synthesized by attaching amino-terminated PEO and PPO side chains to a PAA backbone via an amidation reaction. The majority of the COOH groups are left unreacted for subsequent attachment to the magnetite nanoparticles.

PEO-$NH_2$, and PPO-$NH_2$ reagents. In a typical reaction, a total of 23 g of the three polymers in the desired stoichiometric ratio was added to a reaction vessel. The mixture was heated to 180 °C and reacted for 2 h under a bubbling flow of nitrogen that provided mixing, prevented oxidation, and expelled water produced by the condensation reaction. The product was cooled to room temperature and dissolved in water to produce a 33 wt% solution.

### 2.2.3 Nanoparticle Synthesis

The magnetite nanoparticles were produced by chemical coprecipitation in a graft copolymer solution. In a typical procedure, an aqueous solution containing 2.35 g of iron(III) chloride hexahydrate, 0.86 g of iron(II) chloride tetrahydrate, and 3.75 g of the 33 wt% graft copolymer solution was prepared by dissolving the reagents in 37.5 mL of deoxygenated water. Deoxygenation was achieved by sparging with nitrogen under vigorous stirring for 30 min before reaction. The resulting $Fe^{3+}$ and $Fe^{2+}$ concentrations were 0.22 and 0.11 M, respectively, which provided the 2:1 ratio required to produce $Fe_3O_4$ stoichiometrically. To begin the reaction, the aqueous solution was heated to 80 °C with continual nitrogen sparging and stirring. When the temperature reached 80 °C, the flow of nitrogen was stopped, and 5 mL of 28 wt% ammonium hydroxide were added to precipitate iron oxide in the form of magnetite. The mixture was then stirred for 30 min at 80 °C before cooling to room temperature. After cooling, the coated nanoparticles remained suspended in water indefinitely. This procedure produced 1 g of magnetite in 40 mL of water, which is equivalent to a 2.5 wt% suspension of magnetite.

The magnetic fluids were purified in a Centricon-Plus 100,000 molecular weight cutoff centrifugal ultrafiltration cell (Millipore). The suspensions were first diluted to 0.5 wt% $Fe_3O_4$ with distilled water and then concentrated to 2.5 wt% in the filter. The polymer-coated nanoparticles were retained in the filter while unattached polymer and ions were removed in the filtrate. This process of dilution and concentration in the filter was repeated four times to fully remove free polymer and ions, which we confirmed by evaporating the filtrate and measuring the mass of residual solid until none remained.

### 2.2.4 Instrumentation

Infrared (IR) spectroscopy measurements were made on a Bio-Rad FTS175 FT-IR spectrometer. Samples were prepared by evaporating a small volume of polymer solution or magnetic fluid on a polyethylene card (Thermo Spectra-Tech) and evaporating the solvent for 24 h. All samples were equilibrated in the internal nitrogen atmosphere of the spectrometer for 10 min before measurement of the absorbance spectrum. The absorbance of the card was subtracted from the absorbance of all samples.

Thermogravimetric analysis (TGA) was conducted on a Perkin-Elmer TGA 7 instrument. Polymer solutions or magnetic fluid were dried for 24 h to remove solvent. Approximately 15 mg of dried sample was loaded in the sample pan, which was first flamed to remove any residual carbon. The sample pan was then inserted into the furnace filled with an inert helium atmosphere to prevent oxidation. The heating profile in the TGA was as follows: heat to 150 °C at 5 °C/min; hold at 150 °C for 60 min; heat to 900 °C at 5 °C/min. The sample mass was recorded as a function of time and temperature.

Transmission electron microscopy (TEM) experiments were performed on a JEOL 2010 (200 kV) instrument. Samples were prepared by evaporating dilute suspensions on a carbon-coated film. Superconducting Quantum Interference Device (SQUID) experiments using a Quantum Design MPMS instrument were conducted to determine the magnetization of the particle suspensions in an applied magnetic field. Approximately 0.1 mL of magnetic fluid was used in the SQUID measurements and the exact mass was measured before addition to an airtight sample cell. All SQUID measurements were performed at 300 K over a −1 to +1 Tesla range.

Dynamic light scattering (DLS) experiments were performed with a Brookhaven BI-200SM light scattering system at a measurement angle of 90°. The autocorrelation function was fit with an exponential fitting software program to extract the diffusion coefficient, and the Stokes-Einstein equation was used to convert the diffusion coefficient to the hydrodynamic diameter. The intensity-average size distribution provided by the light scattering software was converted to volume-average and number-average size

distributions for further analysis. Quoted particle sizes are the average of five measurements. All samples were filtered with a 0.22 μm syringe filter to remove dust.

Flocculation experiments were performed with a Hewlett-Packard 8453 UV-Visible spectrometer that was used to track the sample turbidity at 520 nm. Washed magnetic fluid was diluted to 0.005 wt% $Fe_3O_4$ and then placed in a quartz cuvette with a 1 cm pathlength. The temperature of the sample was increased from room temperature at 5 °C/min with an attached Peltier element. A thermocouple probe was inserted into the top of the cuvette to track the actual temperature of the sample during measurements. In some experiments, magnesium sulfate was added to the magnetic fluid to observe the effect on stability.

The zeta potential of particle suspensions was measured on a Brookhaven ZetaPals Zeta Potential Analyzer. Particle suspensions were diluted to 0.005 wt% $Fe_3O_4$ with 1 mM NaCl prior to measurement. Approximately 2 mL of the sample was loaded into the electrode cell. The electrophoretic mobility ($\mu_e$) of the particles was measured over fifteen electrode cycles. The Smoluchowski equation was used to convert the electrophoretic mobility to the zeta potential ($\zeta$):

$$\zeta = \frac{\eta}{\varepsilon}\mu_e \tag{2-1}$$

where $\eta$ and $\varepsilon$ are the viscosity and dielectric constant of the dispersion medium. The quoted zeta potential was an average of five measurements.

## 2.3 Characterization Results

### 2.3.1 Polymer Characterization

The amphiphilic graft copolymers, synthesized via the amidation reaction illustrated in Figure 2-2, served as steric stabilizers for the nanoparticles in water while also providing a hydrophobic domain for extraction. Using the nomenclature defined in Section 2.2.2, the 16/0, 12/4, and 8/8 polymers were produced with each polymer retaining 84% of its carboxylic acid groups on the PAA backbone for attachment to the

particle surface. If the fraction of PPO side chains increased beyond 8% (holding the total grafting fraction constant at 16%), the product was found to be much less soluble in water. Since the graft copolymer products were used directly as particle stabilizers without purification, it was important that the polymer synthesis reaction proceeded to near completion. We used two methods to calculate the extent of reaction. Unreacted PEO-$NH_2$ and PPO-$NH_2$ side chains were quantified by a ninhydrin test on the reaction products for primary amines.[3] The concentration of unreacted side chains was low and the conversion was determined to be 93-95% for the 16/0, 12/4, and 8/8 polymers. IR spectroscopy was also used for qualitative confirmation that the reaction had proceeded to near completion. A typical IR absorbance spectrum for the 16/0 polymer is shown in Figure 2-3a. The peak at 1732 $cm^{-1}$ corresponds to unreacted acid C=O groups in the backbone, while the smaller peak at 1673 $cm^{-1}$ corresponds to C=O amide groups formed in the grafting reaction. The large peak at 1110 $cm^{-1}$ is due to the C–O–C ether linkage in the PEO side chains, which make up approximately 90% of the comb polymer by weight. We also observed that the relative size of the amide peak increased and the acid peak decreased as the grafting density of side chains increased, as shown in Figure 2-3b for a series of polymers with increasing numbers of grafted PEO side chains.

### 2.3.2 Particle Formation and Polymer Attachment

Using the 16/0, 12/4, and 8/8 graft copolymers, we synthesized magnetic fluids that we will refer to by the identity of their stabilizing polymer. In all three magnetic fluids, the magnetite particles remained suspended in water after precipitation and did not sediment when brought into contact with handheld magnets, although over the course of many months, a small amount of settling was observed. The settling was most prevalent for the 8/8 particles (~5 wt% of the particles settled after one month), suggesting that the increased hydrophobicity of the stabilizing layer led to a slight loss in stability. The amount of settled particles was much smaller for the 16/0 and 12/4 fluids. We also synthesized a 4/12 polymer, but it was much less water-soluble and could not stabilize the particles, presumably due to an insufficient number of hydrophilic side chains. Unless otherwise noted, all magnetic fluids in this work were synthesized with 1.25 g of

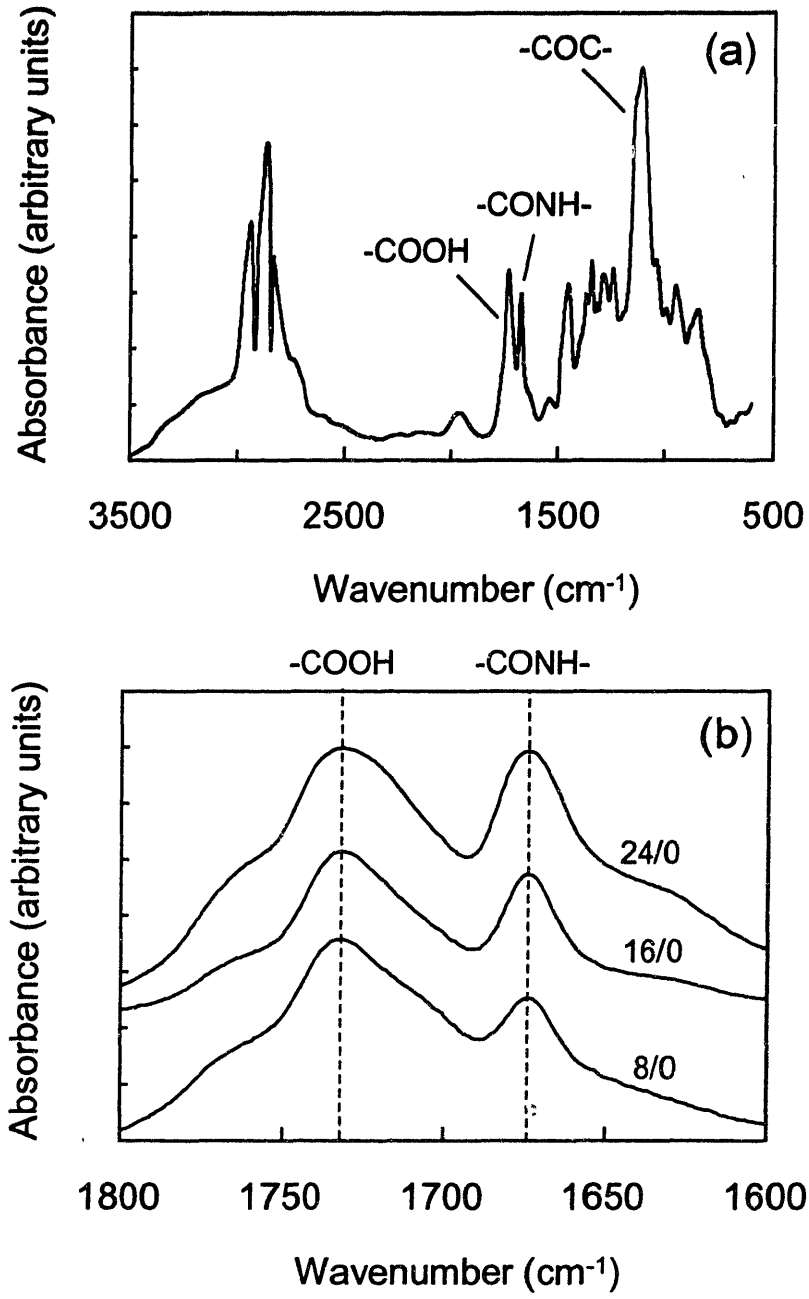


**Figure 2-3.** (a) IR spectrum of the 16/0 graft copolymer. The peak at 1673 $cm^{-1}$ confirms the presence of the amide linkage between the PAA backbone and the PEO side chains. (b) Comparison of the IR spectra of a series of graft copolymers with PEO side chains grafted to 8, 16, and 24% of the carboxylic acid groups in the backbone.

graft copolymer to stabilize 1 g of magnetite. With lower polymer concentrations, a significant amount of particle settling was observed within several hours, which is indicative of large uncoated magnetite aggregates.

To determine the amount of chemically bound polymer on the particles, the magnetic fluids were analyzed with thermogravimetric analysis (TGA) after ultrafiltration to remove unattached polymer and ions. The TGA results are shown in Figure 2-4, where the residual mass is plotted as a function of the temperature. The results for pure 16/0 polymer are also shown in the figure, which illustrate that the polymer decomposed in the inert atmosphere at approximately 400 °C. Less than 5% of the original weight remains as residual carbon after decomposition. The decomposition of the bound polymer appeared to be catalyzed by the magnetite, as it began to decompose between 200 and 300 °C. The attached 16/0 polymer, which contained no PPO side chains, decomposed more rapidly than the attached 12/4 and 8/8 polymers, although all particles were fully stripped of polymer by 400 °C leaving only magnetite.

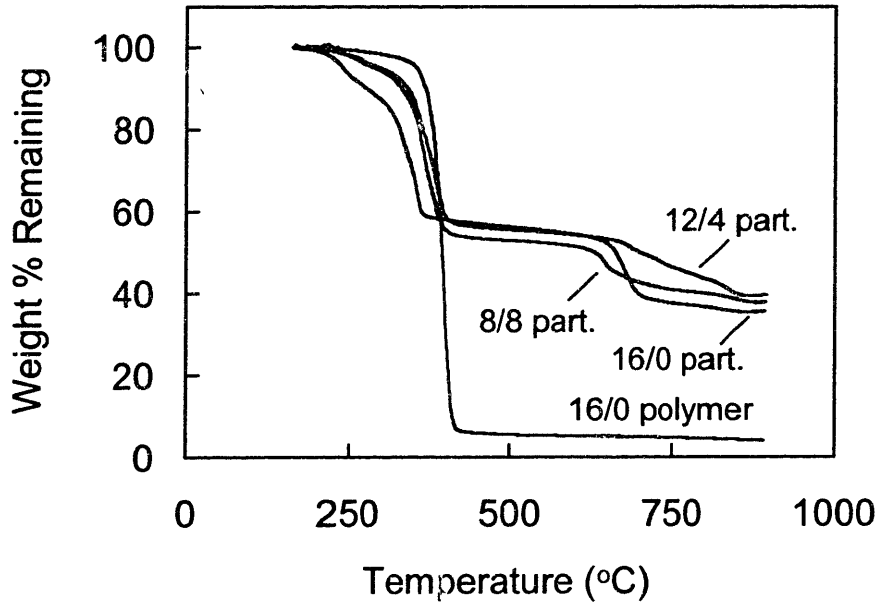


**Figure 2-4.** TGA analysis of graft copolymer and magnetic fluids. In an inert atmosphere, the 16/0 polymer decomposes at approximately 400 °C leaving little residual carbon. The graft copolymer attached to the magnetite nanoparticles also decomposes by 400 °C leaving bare magnetite. Above 650 °C, the magnetite is reduced to elemental iron.

The residual magnetite weight was used to compute the bound-polymer:magnetite mass ratio for three types of particles, which we found to be 0.78 (16/0), 0.80 (12/4), and 0.89 (8/8). We also estimated the amount of bound polymer through a combination of iron titration[4] and gravimetric measurement of solids content. With this alternate method, we obtained an average bound-polymer:magnetite mass ratio of 0.8 for the three fluids, which is consistent with the TGA measurements. Approximately two-thirds of the polymer added during the synthetic procedure is therefore chemically bound to the magnetite. Figure 2-4 also shows that above approximately 650 °C, the remaining magnetite undergoes additional weight loss, which is most likely reduction of $Fe_3O_4$ to elemental Fe. Between 29 and 35% of the remaining mass is lost above 650 °C, which is similar to the oxygen content of magnetite (28 wt%).

Infrared spectroscopy was used to examine the nature of the graft copolymer attachment to the magnetite surface. Previous studies of carboxylic acid attachment to magnetite have indicated that the carboxylate group forms a strong *d*-orbital chelation with surface iron atoms on the magnetite surface.[5] The bond between the carboxylic acid group and magnetite is covalent in nature and has a characteristic IR absorbance at 1440 and 1590 $cm^{-1}$. In our system, these peaks are heavily obscured by IR peaks from the polymer and are difficult to observe. However, the polymer attachment can be observed by the disappearance of the free acid, as shown in Figure 2-5, where the IR trace of free 16/0 polymer is compared with ultrafiltered 16/0 particles in the carbonyl absorption region. The amide peak at 1673 $cm^{-1}$ is relatively unchanged after bonding to the particles while there is a significant reduction in the absorption of the free acid at 1732 $cm^{-1}$. Although it is challenging to quantify the amount of unattached COOH groups in the polymer backbone due to baseline variation, we estimate that 40% of the free COOH groups present in the graft copolymer remain unattached after magnetic fluid synthesis by integration of the peak areas. This result suggests that there are significant loops present in the backbone of the graft copolymer after attachment to the particle.

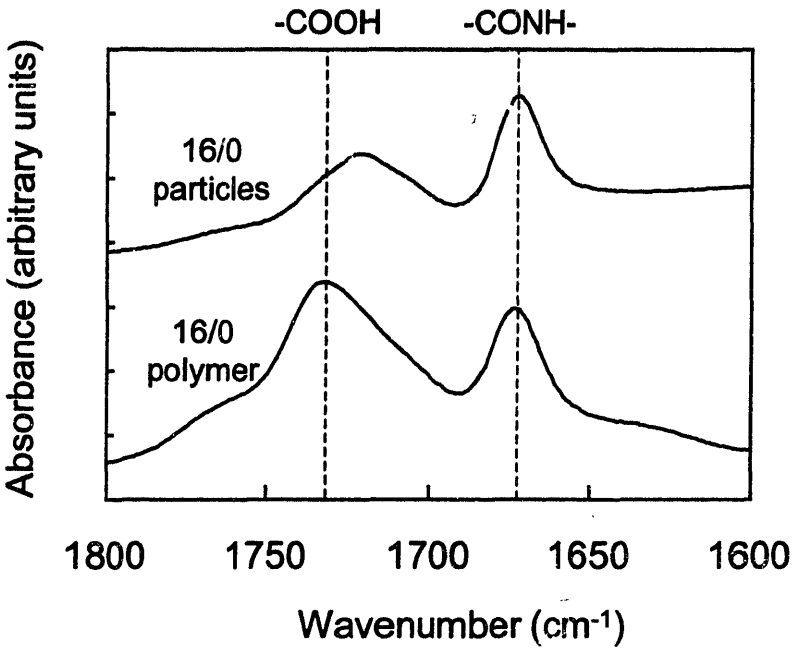


**Figure 2-5.** IR comparison of carbonyl groups before and after attachment of 16/0 graft copolymer to magnetite. After bonding to the magnetite, the IR absorbance from free COOH groups decreases while the absorbance from amide carbonyl stays constant. We estimate that approximately 40% of the original free acid groups remain unattached.

### 2.3.3 Electron Microscopy

The size and size distribution of the $Fe_3O_4$ nanoparticles was measured with TEM, which allowed characterization of the $Fe_3O_4$ core. In the TEM pictures, the contrast for the polymer shell is low and could not be distinguished from the background. Figure 2-6a shows a TEM image of the 16/0 nanoparticles. The apparent particle aggregation in this image is due to artifacts that occur as water is evaporated from the sample during preparation. The dimensions of 500 particles were measured and observed to fit a lognormal distribution:

$$p(x) = \frac{1}{\sqrt{2\pi}\sigma x} e^{-(\ln x)^2/2\sigma^2} \qquad (2\text{-}2)$$

where $p(x)$ is the probability density of the distribution, $x = D/D_p$ is the reduced diameter, $D_p$ is the median diameter, and $\sigma^2$ is the variance of the distribution. This function fit the measured distribution well, as shown in Figure 2-6b. The best fit to the lognormal

distribution was obtained with $D_p$ = 7.5 nm for the 16/0 particles. The fitted $\sigma$ value was found to be 0.32, which represents significant polydispersity as is clear from the TEM image.

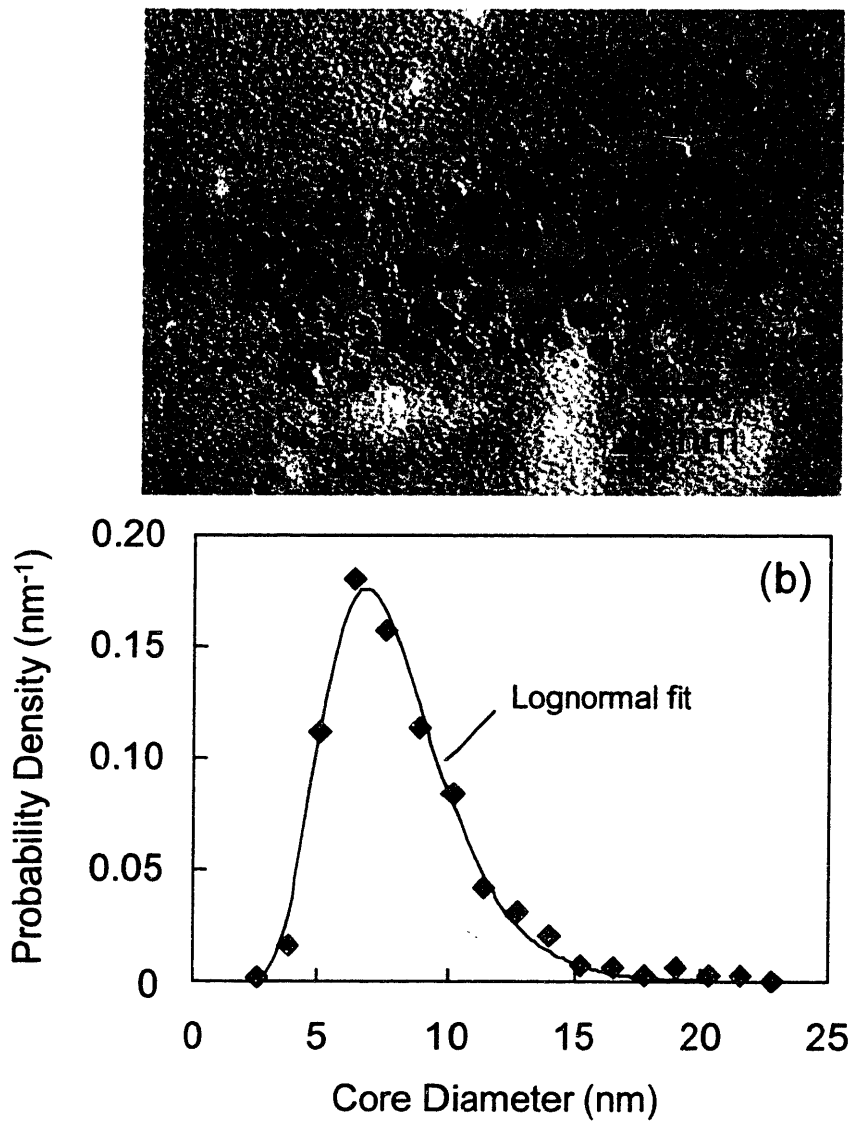


**Figure 2-6.** (a) TEM image and (b) particle size distribution of 16/0 particles as fit by a lognormal particle size distribution. The particle size distribution was determined by measuring the size of 500 nanoparticles over a series of TEM images from different regions of the sample.

High-resolution TEM was able to provide additional information about the internal structure of the magnetite particles. Figure 2-7 shows a TEM image at $10^6\times$ magnification, in which the atom planes are visible in the particles as rows of black dots. The intensity of the atoms in the image varies due to the angle of orientation of the particles with respect to the electron beam. This image suggests that the magnetite particles are crystalline; in addition, the lack of visible grain boundaries within particles implies that the particles are single crystalline domains, which is an important property for particle superparamagnetism.[1]

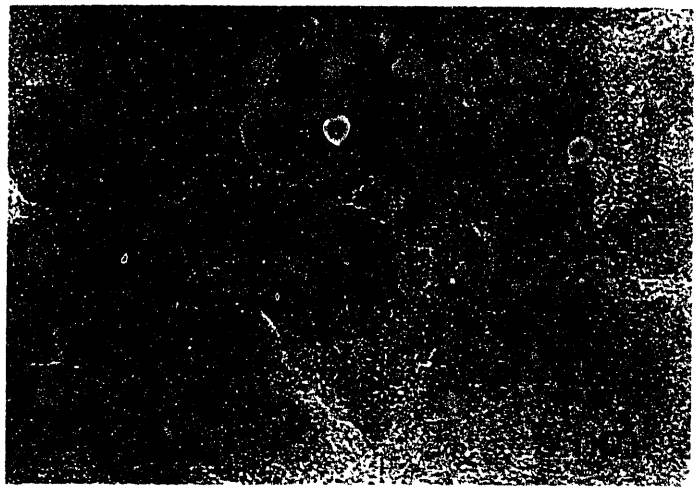

**Figure 2-7.** High resolution TEM image of 16/0 particles. The atomic planes are visible throughout the nanoparticles, suggesting the particles are single crystalline domains of magnetite.

## 2.3.4 Magnetic Properties

SQUID analysis yielded a second independent measurement of the magnetite core size, as well as the particle magnetization. In the SQUID experiments, a variable magnetic field was applied to the sample, and the induced magnetic field was measured, thereby providing the magnetization of the sample. Figure 2-8 shows magnetization curves obtained for 16/0 particles in water at two concentrations. At low applied field strengths, the magnetization response is steep and approximately linear as the particles begin to align with the applied field. At higher fields, the particles are essentially completely aligned with the field, and the magnetization approaches saturation. There is

essentially no magnetic remanence (only 1.2% of the saturation magnetization) at zero applied field since the particle size is sufficiently small that each particle is a single magnetite crystal with a permanent magnetic dipole. This superparamagnetic behavior is expected of $Fe_3O_4$ nanoparticles.[1] If there are no magnetic interactions between particles, the magnetization curves for fluids of different concentrations should scale by the weight fraction of magnetite, as observed in Figure 2-8 where an increase in concentration by a factor of five increases proportionally the measured magnetization. This case is typical for $Fe_3O_4$ particles, which feel a relatively weak interparticle magnetic attraction.[6]

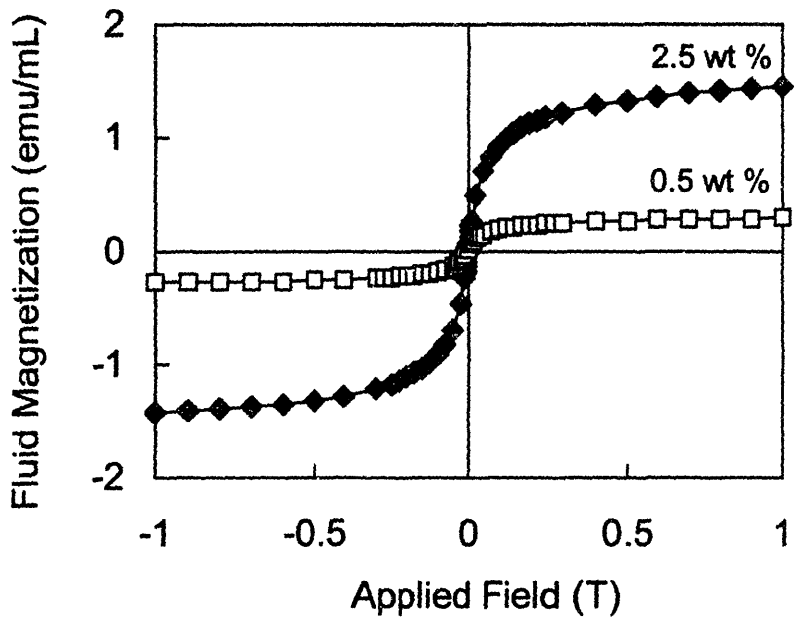


**Figure 2-8.** Magnetization response of 16/0 particles from SQUID measurements. The magnetic fluids show superparamagnetic behavior with approximately zero remanence at zero applied field. At high applied fields, the fluid becomes magnetically saturated due to the alignment of all particles with the magnetic field.

Chantrell et al.[7] showed that the magnetization, *M*, of superparamagnetic suspensions can be used to determine the size distribution of the particles. The theoretical basis of this theory is that the alignment of particles in an applied field is a competition between the magnetic force on the particle and Brownian motion, both of which are functions of particle size. This analysis assumes a lognormal size distribution

of non-interacting particles, which is consistent with the TEM data. The derived median diameter ($D_p$) and standard deviation ($\sigma$) are given by[7]

$$D_p = \left( \frac{18kT}{\pi M_d} \left[ \frac{\chi_i}{3\varepsilon M_d H'} \right]^{1/2} \right)^{1/3} \tag{2-3}$$

$$\sigma = \frac{1}{3} \left( \ln \left( \frac{3\chi_i H'}{\varepsilon M_d} \right) \right)^{1/2} \tag{2-4}$$

In these relationships, $\chi_i$ is the initial magnetic susceptibility on a volume basis (i.e., the slope of the magnetization curve at $H = 0$), $\varepsilon$ is the volume fraction of particles, $M_d$ is the saturation magnetization of bulk magnetite on a volume basis, and $H'$ is determined from the $M = 0$ intercept of a graph of $M$ versus $1/H$ at high applied fields. We performed SQUID experiments on the 16/0, 12/4, and 8/8 magnetic particles to obtain the $Fe_3O_4$ core size. Five 16/0 samples spanning two different concentrations yielded an average $D_p$ of 7.4 ± 0.1 nm and an average $\sigma$ value of 0.35. The SQUID results were highly reproducible and consistent with the TEM results ($D_p$ = 7.5 nm, $\sigma$ = 0.32). The 12/4 and 8/8 samples did not show any significant differences in core size or polydispersity from the 16/0 samples, suggesting that changes in the PEO:PPO side chain ratio had little or no effect on the nanoparticle formation process.

The saturation magnetization of the fluids can be obtained from the magnetization curve by extrapolating the magnetization as $H \rightarrow \infty$. In practice, this is done by extrapolating the magnetization as $1/H \rightarrow 0$ on a graph of $M$ versus $1/H$ at high applied fields. The saturation magnetization of the fluids was directly proportional to the amount of $Fe_3O_4$ in the suspension. After normalizing for the magnetite weight fraction, we found an average value of 63 ± 5 emu/g $Fe_3O_4$ for the 16/0 particles. The magnetization of the 12/4 and 8/8 particles was not significantly different. The core magnetization of our particles is significantly lower than the saturation magnetization of bulk $Fe_3O_4$, 87 emu/g,[8] which is a typical result for $Fe_3O_4$ nanoparticles, which usually have a saturation magnetization of 50-70 emu/g.[8-10] The lower achieved magnetization is usually attributed

to disruption of the magnetic moment of atoms in the outer surface layer, forming a nonmagnetic layer that is a significant fraction of the particle volume for nanoparticles.[11] Usually, this nonmagnetic layer results in the magnetic diameter being significantly smaller than the TEM diameter,[8] but this was not the case with our particles. Other researchers have also observed a magnetic diameter that is equal to or greater than the TEM diameter.[11] The magnetization of the particles was extremely stable as it decreased by less than 4% over six months, possibly due to oxidation of the magnetite to maghemite.

### 2.3.5 Dynamic Light Scattering: Hydrodynamic Size

Dynamic light scattering (DLS) yielded the hydrodynamic diameter of the particles (including the polymer shell), from which we could estimate the thickness of the polymer layer. Figure 2-9 shows the DLS volume- and number-average size distributions for the 16/0 particles, with similar results obtained for the 12/4 and 8/8 particles (not shown). The volume-average distribution consisted primarily of individual particles that ranged from 15 to 40 nm in diameter, although we also observed larger aggregates that were approximately 60 to 150 nm in diameter. The individual particles comprised 89% of the total volume, while 11% consisted of larger aggregates. The number-average hydrodynamic diameter was 26 nm with a ± 3 nm standard deviation in the measured average. The number-average provides a better estimate of the size of individual nanoparticles as it is not biased as greatly by the aggregates as is the volume-average. By subtracting the median core radius from the number-average hydrodynamic radius, we calculated the thickness of the polymer layer to be 9.4 nm for the 16/0 particles. The layer thickness is larger than the magnetite core radius, meaning that the majority of the volume of the total particle is water-swollen polymer. The number-average diameters for the 12/4 and 8/8 particles were found to be 27 and 26 nm, respectively, suggesting that the polymer layer thickness is relatively insensitive to the polymer composition.

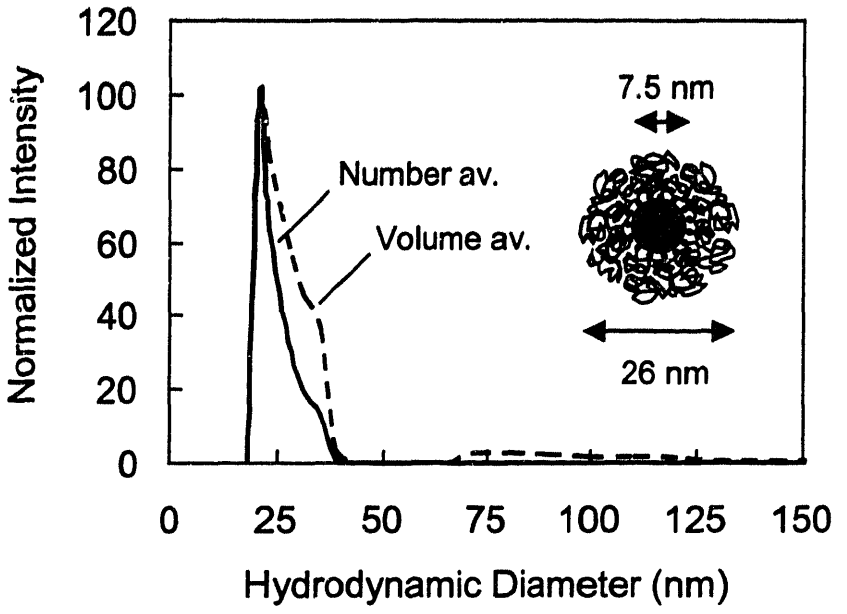


**Figure 2-9.** Size distribution of 16/0 particles from dynamic light scattering. In the volume-average distribution, 11% of the particles by volume are present as large aggregates. The number-average distribution gives a mean hydrodynamic diameter of 26 nm. This value along with the core diameter from TEM (Figure 2-6) yields a polymer layer thickness of 9.4 nm.

Polymer scaling theory allows the measured value of the polymer shell thickness to be compared with theoretical predictions. The thickness of a layer of end-grafted chains on a linear surface is known to scale with the grafting density of the chains to the 1/3 power.[12] On a spherical surface like those of the $Fe_3O_4$ particles, the scaling behavior is more complex and depends on the curvature of the surface, as increases in the curvature decrease the interactions between chains due to spatial effects.[13,14] According to the discrete blob model of Farinha et al.,[14] the thickness of an end-grafted polymer layer, $L$, on a spherical surface is given by

$$L = \left[ Nl^{1/\nu} \frac{(1+2\Xi)^{1/\nu} - 1}{(2\Xi)^{1/\nu}} + R_c^{1/\nu} \right]^{\nu} - R_c \qquad (2\text{-}5)$$

where $N$ is the number of repeat units in the chain, $l$ is statistical length of the monomer unit, $\nu$ is the scaling exponent of the chains (3/5 for a polymer in a good solvent), $R_c$ is the radius of the spherical core, and $\Xi$ is given by

$$\Xi = \frac{\sin\left(\gamma/2\right)}{1-\sin\left(\gamma/2\right)} \tag{2-6}$$

$$\gamma = \arccos\left(\frac{\cos\alpha}{1-\cos\alpha}\right) \tag{2-7}$$

$$\alpha = \pi\frac{f+2}{3f} \tag{2-8}$$

where $f$ is the number of end-grafted chains on the sphere.

To apply this theory for end-grafted polymer chains to the 16/0 nanoparticles, we assumed that all PEO side chains in the graft copolymer were directly end-grafted to the magnetite surface. The parameters for PEO of molecular weight 3000 in water are $N$ = 68, $l$ = 0.40 nm, and $\nu$ = 3/5. To determine the grafting density of PEO side chains, we used the bound-polymer:magnetite mass ratio of 0.8 determined in Section 2.3.2 and computed the total surface area of polydisperse magnetite particles with $D_p$ = 7.5 nm and $\sigma$ = 0.32 (values from TEM). With the known molecular weight and side chain ratio of our 16/0 polymer, we calculated the grafting density of PEO chains to be 1.17 PEO chains/nm$^2$. This is equivalent to $f$ = 206 PEO chains grafted on a median particle that is 7.5 nm in diameter. Equations 2-5 through 2-8 predict that with this grafting density on a particle with a 7.5 nm core diameter, the layer thickness should be 8.7 nm, which is close to the thickness of 9.4 nm measured with DLS. The lower predicted thickness could be the result of our assumption that all chains were end-grafted to the magnetite surface, whereas IR analysis (Section 2.3.2) indicated that significant portions of the PAA backbone were not attached. The thickness from DLS is well below the predicted thickness of the chains on a planar surface (13.4 nm), which represents an upper limit.

Analysis of the 12/4 and 8/8 polymer shells, which contain two types of grafted side chains, requires more complex methods that are discussed in Chapter 3.

## 2.4 Colloidal Stability

The colloidal stability of our aqueous magnetic fluids for organic separation is important because it will determine the range of process conditions over which the magnetic fluids can be used. Napper[15] suggests that sterically stabilized dispersions will flocculate under the theta conditions of the stabilizing polymer, assuming the polymer is sufficiently-well anchored that it does not detach. The theta conditions are defined as the conditions under which a polymer of infinite molecular weight will become insoluble in the dispersion medium.[15] PEO is the stabilizing polymer for all of our magnetic fluids and should therefore determine the stability limits.

Figure 2-10a shows the turbidity of our magnetic fluids at 520 nm as a function of temperature as measured with a UV-Visible spectrometer. The 16/0 magnetic fluid shows little change until the temperature is increased above 90 °C. At approximately 95 °C, there is a rapid increase in turbidity as the 16/0 nanoparticles flocculate and eventually settle. The flocculation temperature is close to the theta temperature of PEO (96 °C) as indicated by the dashed line in Figure 2-10a. The stability of the 16/0 particles is therefore limited by the solubility of PEO in water. The 12/4 and 8/8 particles show a similar trend, in that there is little increase in turbidity at elevated temperature until flocculation occurs. The critical flocculation temperature appears to decrease as the PPO content increases. Because the attachment moiety should not affect the flocculation temperature,[15] the PPO side chains must be somewhat mixed with PEO side chains in the polymer shell. Neutron scattering experiments and lattice calculations that are discussed in Chapter 3 further support this hypothesis. The temperature at which the particle synthesis is conducted (80 °C) is close to the flocculation temperature of the 8/8 particles, indicating that the temperature should be well controlled during synthesis. We also observed that after flocculating all of the magnetic fluids, the particles could be easily redispersed after cooling to room temperature. This observation is consistent with steric stabilization by polymers, which is usually thermodynamic rather than kinetic.[15]

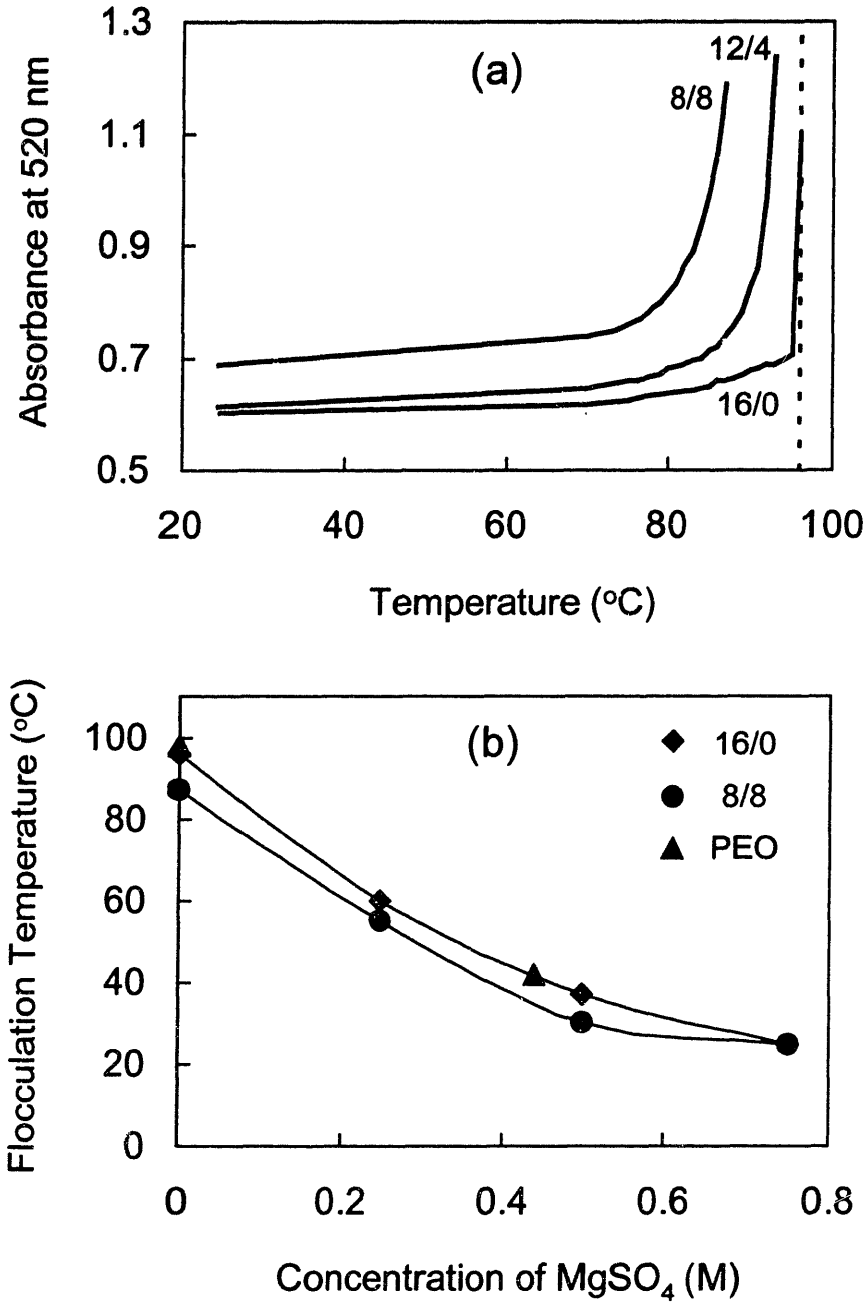


**Figure 2-10.** (a) Turbidity of dilute magnetic fluids indicates the critical flocculation temperature of the particles. The 16/0 particles flocculate at 96 °C, which is the theta temperature of PEO (indicated by the dashed line), while the 12/4 and 8/8 particles flocculate at lower temperatures. (b) Flocculation temperature (temperature at which the turbidity increases dramatically) as a function of ionic strength in $MgSO_4$ solutions. The addition of salt decreases the flocculation temperature, which is equivalent to the cloud point of high molecular weight PEO[16] for the 16/0 particles.

A similar trend for the particle stability is seen in Figure 2-10b, which illustrates the critical flocculation temperature of the 16/0 and 8/8 magnetic fluids as a function of $MgSO_4$ concentration. The addition of salt is known to dehydrate PEO and cause it to precipitate at elevated concentrations.[16] Figure 2-10b shows that at various salt concentrations, the temperature required for destabilization of the 16/0 particles is essentially identical to that observed for pure PEO,[16] suggesting it is PEO that is fully responsible for stabilization. In addition, the flocculation temperature of the 16/0 magnetic fluids is always approximately 5-10 °C higher than that of the 8/8 magnetic fluids. The $MgSO_4$ concentration must be increased above 0.6 M to flocculate the particles at room temperature. This salt concentration is higher than is likely to be observed in most separation processes. In addition, PEO is much more sensitive to divalent salts than monovalent salts. For example, the concentration of NaCl must be increased to approximately 3.0 M before PEO becomes insoluble.[16]

The magnetic fluids did not appear to be sensitive to pH, in that they remained stable over a wide range of acid and base concentrations. Directly after synthesis, the pH of the stable magnetic fluids was 6.5; while the fluids were synthesized at elevated pH, nearly all of the ammonium hydroxide was either consumed by the reaction or volatilized as ammonia during the 30 minute synthesis at 80 °C. After ultrafiltration to remove unbound polymer, the pH of the suspensions increased to 7.5. At this pH, we found that both the 16/0 and 8/8 particles had a negative zeta potential, as shown in Figure 2-11. The zeta potential is defined as the electrostatic potential at the shear plane, which in the case of our particles is the outside edge of the polymer shell. This potential is approximately –28 mV when the pH is 7.5. The source of the negative charge appears to be residual COOH groups in the PAA backbone (as opposed to charge on the $Fe_3O_4$ surface) as the zeta potential seems to follow the behavior of PAA. At neutral and basic pH, where carboxylic acid groups exist as $COO^-$ carboxylate groups, the particles have a negative charge. By adding acid to protonate the acid groups, the charge can be neutralized, with the particles having zero charge at low pH. The $pK_a$ of polyacrylic acid is approximately 4.5, which is close to the pH at which the particles have lost half of their charge. This analysis is consistent with our IR analysis, which showed that approximately 40% of the remaining COOH groups in the graft copolymer backbone

were not attached to the surface. Throughout the entire pH range of 2 to 12, the nanoparticles remained suspended in water indefinitely, suggesting that the graft copolymer does not detach under acidic or basic conditions. In addition, it shows that electrostatics do not play an important role in particle stabilization as protonation of the acid groups did not flocculate the particles. The unattached, negatively charged carboxylate groups that are present at neutral pH are probably buried deep in the shell, as the zeta potential of the particles is much lower than for particles coated with carboxylate functional groups (approximately –60 mV).

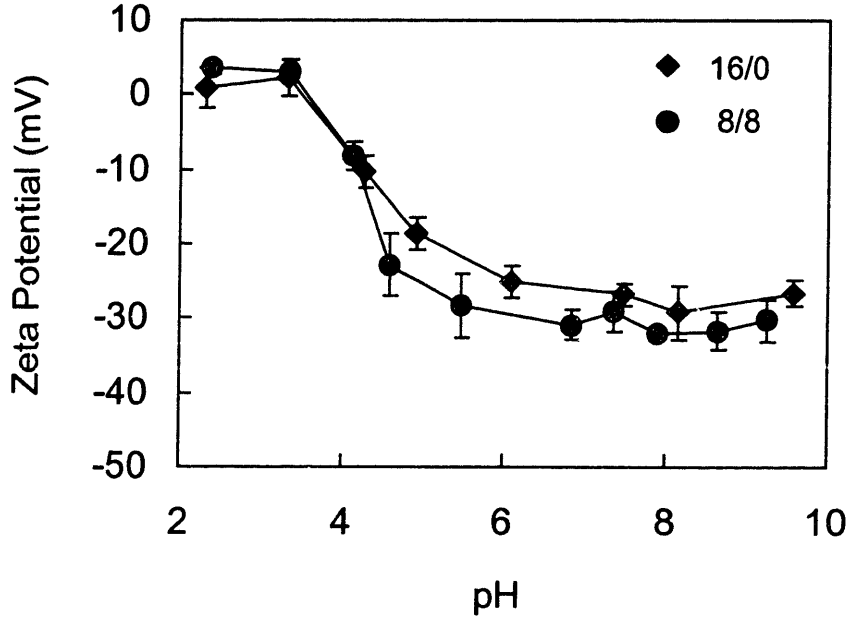


**Figure 2-11.** Zeta potential of dilute magnetic fluids. The washed magnetic nanoparticles have a pH of approximately 7.5 and a negative zeta potential. The charge is a result of unattached $COO^-$ groups in the polymer backbone, as the zeta potential is neutralized under acidic conditions that protonate these groups.

## 2.5 Control of Core Size and Magnetization

The core size and magnetization of the nanoparticles are key features that govern the magnetic collection of the particles, which is discussed in detail in Chapter 5. Using SQUID measurements, we examined the effect of changing the synthetic conditions on these properties. Specifically, we varied the 16/0 polymer concentration and the

precipitation temperature to determine if the particle size or magnetization could be controlled with these easily adjustable parameters. Table 2-1 shows that both increasing the polymer concentration and decreasing the temperature decreased significantly the median particle diameter from its base value of 7.4 nm. We hypothesize that an increase in the polymer:magnetite mass ratio from 1.25 increases the rate of polymer diffusion to the particle surface and leads to smaller particles. Decreasing the temperature from 80 °C would decrease both the rate of polymer diffusion and the kinetics of magnetite precipitation, but the effect on the precipitation rate must have been dominant since the particle size decreased. The precipitation temperature also affected the magnetic properties of the particles. Previous investigators have suggested that precipitation at or above 80 °C favors the formation of magnetite ($Fe_3O_4$) over less magnetic iron oxide forms, such as maghemite ($\gamma$-$Fe_2O_3$).[17,18] This hypothesis seems consistent with the SQUID data in Table 2-1, which show that the calculated saturation magnetization of the particles decreased from 63 emu/g to 53 emu/g when the temperature was lowered from 80 to 60 °C. As the standard deviation of the measured particle magnetization is ± 5 emu/g, this change represents a significant decrease. In contrast, increasing the polymer concentration did not have a significant effect on the particle magnetization. Increasing the temperature of the synthesis above 80 °C is not feasible, as the 8/8 particles are very near to the flocculation limit at this temperature; likewise, decreasing the polymer concentration led to a significant number of uncoated particles that settled rapidly. Our original synthetic conditions are therefore optimal given the accessible range of process variables. It is a limitation of our synthetic method that it is difficult to control the size or polydispersity of the particles, as HGMS collection should be easier with larger particles (see discussion in Chapter 5).[19] Better control of particle size may be possible by maintaining the reagent concentrations at a constant level during the synthesis and removing the precipitated nanoparticles from the reaction zone, although this requires specialized equipment.

**Table 2-1.** Effect of synthetic conditions on core size and magnetization

| Polymer | Temperature (°C) | Polymer:Magnetite Mass Ratio | $D_p$ [a] (nm) | $\sigma$ | $M_p$ [b] (emu/g) |
|---|---|---|---|---|---|
| 16/0 | 80 | 1.25 | 7.4 | 0.35 | 63 |
| 16/0 | 80 | 2.00 | 6.7 | 0.36 | 67 |
| 16/0 | 60 | 1.25 | 6.3 | 0.29 | 53 |

a) The standard deviation of the measured median particle diameter ($D_p$) is ± 0.1 nm.
b) The standard deviation of the measured particle magnetization ($M_p$) is ± 5 emu/g.

## 2.6 Summary

We have synthesized and characterized a novel class of water-based magnetic fluids that are specifically tailored for the removal of organic compounds from water. These materials consist of a magnetic $Fe_3O_4$ core surrounded by a polymer shell composed of an outer hydrophilic region for colloidal stability in water and an inner hydrophobic region for solubilization of organics. The magnetic fluids are produced by chemical coprecipitation of iron salts in aqueous solution in the presence of a soluble PEO/PPO-PAA graft copolymer. The PEO and PPO side chains are responsible for the hydrophilic and hydrophobic regions in the polymer shell, respectively. The ratio of the side chains in the graft copolymer can be controlled as we synthesize the polymer by reacting amino-terminated PEO and PPO side chains with a PAA backbone in an amidation reaction.

The magnetic fluids were characterized with a number of techniques that revealed the size of the core and shell, the magnetic properties, and the nature of the graft copolymer attachment. TEM and SQUID analysis showed that the magnetite core had a median diameter of 7.5 nm and was significantly polydisperse. The magnetization response of the suspensions was superparamagnetic with a saturation magnetization of the magnetite core that was close to the bulk value for magnetite. We were not able to substantially change either the core size or magnetization by varying the temperature or the polymer concentration during synthesis. IR spectroscopy showed that the backbone of the graft copolymer was not completely attached, in that approximately 40% of the

carboxylic acid groups were not covalently attached to the magnetite surface. The shell thickness was determined to be 9.4 nm with DLS, which also showed that a small fraction of the particles were present as larger aggregates.

We also examined the colloidal stability of the fluids to determine their stability limits. As expected, we found that the particles were sterically stabilized by PEO and the stability limits were the theta conditions of PEO for the 16/0 particles, while the 12/4 and 8/8 particles flocculated slightly before the theta conditions for PEO. Regardless, the magnetic fluids were stable over a wide range of temperature, ionic strength, and pH. The graft copolymer did not detach from the magnetite even at extremely acidic conditions where the free acid groups in the backbone were protonated. Zeta potential measurements showed that the particles have a moderate negative charge at neutral pH but that charge is not important in colloidal stability.

## 2.7 Bibliography


(1) Rosensweig, R. E. *Ferrohydrodynamics*; Dover Publications, Inc.: Mineola, NY, 1985.

(2) Darwin, D. C.; Gartner, E. M.; Chun, B.; Koyata, H.; Kuo, L. L. Cement and Cement Composition Having Improved Rheology. U.S. Patent 5,583,183, 1996.

(3) Curotto, E.; Aros, F. Quantitative Determination of Chitosan and the Percentage of Free Amino Groups. *Anal. Biochem.* **1993**, *211*, 240-241.

(4) Yoe, J. H.; Jones, L. Colorimetric Determination of Iron with Disodium-1,2-dihydroxybenzene-3,5-disulfonate. *Ind. Eng. Chem.* **1944**, *16*, 111-115.

(5) Mikhailik, O. M.; Povstugar, V. I.; Mikhailova, S. S.; Lyakhovich, A. M.; Fedorenko, O. M.; Kurbatova, G. T.; Shklovskaya, N. I.; Chuiko, A. A. Surface Structure of Finely Dispersed Iron Powders. I. Formation of Stabilizing Coating. *Colloids Surf.* **1991**, *52*, 315-324.

(6) Shen, L. F.; Stachowiak, A.; Fateen, S. E. K.; Laibinis, P. E.; Hatton, T. A. Structure of Alkanoic Acid Stabilized Magnetic Fluids. A Small-Angle Neutron and Light Scattering Analysis. *Langmuir* **2001**, *17*, 288-299.

(7) Chantrell, R. W.; Popplewell, J.; Charles, S. W. Measurements of Particle Size Distribution Parameters in Ferrofluids. *IEEE Trans. Magn.* **1978**, *14*, 975-977.

(8) Shen, L.; Laibinis, P. E.; Hatton, T. A. Aqueous Magnetic Fluids Stabilized by Surfactant Bilayers. *J. Magn. Magn. Mater.* **1999**, *194*, 37-44.

(9) Mendenhall, G. D.; Geng, Y.; Hwang, J. Optimization of Long-Term Stability of Magnetic Fluids from Magnetite and Synthetic Polyelectrolytes. *J. Colloid Interface Sci.* **1996**, *184*, 519-526.

(10) Lee, J.; Isobe, T.; Senna, M. Preparation of Ultrafine Fe3O4 Particles by Precipitation in the Presence of PVA at High pH. *J. Colloid Interface Sci.* **1996**, *177*, 490-494.

(11) Feltin, N.; Pileni, M. P. New Technique for Synthesizing Iron Ferrite Magnetic Nanosized Particles. *Langmuir* **1997**, *13*, 3927-3933.

(12) De Gennes, P. G. Conformations of Polymers Attached to an Interface. *Macromolecules* **1980**, *13*, 1069-1075.

(13) Lin, E. K.; Gast, A. P. Self Consistent Field Calculations of Interactions Between Chains Tethered to Spherical Interfaces. *Macromolecules* **1996**, *29*, 390-397.

(14) Farinha, J. P. S.; d'Oliveira, J. M. R.; Martinho, J. M. G.; Xu, R. L.; Winnik, M. A. Structure in Tethered Chains: Polymeric Micelles and Chains Anchored on Polystyrene Latex Spheres. *Langmuir* **1998**, *14*, 2291-2296.

(15) Napper, D. H. *Polymeric Stabilizaton of Colloidal Dispersions*; Academic Press Inc.: London, 1983.

(16) Bailey, F. E. J.; Callard, R. W. Some Properties of Poly(ethylene Oxide) in Aqueous Solution. *J. Appl. Polym. Sci.* **1959**, *1*, 56-62.

(17) Shen, L.; Laibinis, P. E.; Hatton, T. A. Bilayer Surfactant Stabilized Magnetic Fluids: Synthesis and Interactions at Interfaces. *Langmuir* **1999**, *15*, 447-453.

(18) Bica, D. Preparation of Magnetic Fluids for Various Applications. *Romanian Rep. Phys.* **1995**, *47*, 265-272.

(19) Gerber, R.; Birss, R. R. *High Gradient Magnetic Separation*; Research Studies Press: London, United Kingdom, 1983.

# Chapter 3

# Structural Analysis of the Polymer Shell

## 3.1 Introduction

Chapter 2 detailed the synthesis of water-based magnetic fluids with coatings that are tailored both to provide colloidal stability in the dispersion medium and to have an affinity for organic solutes. Provided that the particles have a strong affinity for organics, these materials could be used in tandem with high gradient magnetic separation as a novel method of separating small organic molecules from water. The magnetic nanoparticles in the fluid were synthesized and coated by precipitating magnetite ($Fe_3O_4$) in an aqueous solution containing a graft copolymer stabilizer. The polyacrylic acid (PAA) backbone of the graft copolymer binds to the magnetite particles shortly after nucleation, limiting the growth of the particles and simultaneously forming a polymer shell. The graft copolymer contains hydrophilic polyethylene oxide (PEO) and hydrophobic polypropylene oxide (PPO) side chains that we hypothesize will form an outer hydrophilic region that provides colloidal stability in water and an inner hydrophobic region for solubilization of organic species (illustrated in Figure 2-1). In Chapter 2, we detailed the synthetic procedure and characterized the nanoparticles in terms of their $Fe_3O_4$ core size, polymer shell thickness, and magnetic properties. While that chapter revealed general structural information, it did not provide any information on the internal structure of shell. Small angle neutron scattering (SANS) measurements and self-consistent mean-field lattice calculations are employed in this chapter to provide a way of examining the internal structure, including evidence of hydrophobic domain formation.

SANS is a powerful tool for determining the structure of colloidal systems such as polymers, micelles, and nanoparticle dispersions.[1] Like X-ray scattering, it can probe extremely small structures in the 1-50 nm size range, which is the appropriate scale for the nanoparticles in our magnetic fluid. In this technique, the size and composition of a structure, as well as interactions, are deduced from the neutron scattering pattern of a

sample. A key feature of SANS is that it allows different regions of a structure to be probed independently through selective deuteration of the sample. The large difference in neutron scattering from hydrogen and deuterium results in significant changes in the scattering pattern when deuterated materials are used in place of hydrogenated materials – a technique known as contrast matching. In this work, we prepare magnetic fluids in $H_2O$-rich and $D_2O$-rich solvents to isolate scattering from the $Fe_3O_4$ core and polymer shell, respectively. Scattering from the polymer shell can be used to deduce the water penetration into the shell, giving information about the presence of hydrophobic domains. Previous work on SANS analysis of magnetic fluids has demonstrated the feasibility of using this technique to probe the size, structure, and aggregation behavior of the particles.[2,3] Likewise, SANS has been shown to be an excellent tool in identifying hydrophobic domains in micellar systems composed of PEO-PPO-PEO triblock copolymers.[4-6]

Self-consistent mean-field lattice calculations provide another method for examining the internal structure of the polymer shell within the magnetic fluids. This method, originally developed by Scheutjens and Fleer[7] and later modified by Bjorling et al.,[8] has been applied extensively in modeling the solution behavior of mixtures of PEO and PPO,[9] the micellization of PEO-PPO-PEO triblock copolymers,[10-12] and the structure of PEO-PPO-PEO triblock copolymers adsorbed at surfaces,[13,14] and of terminally grafted PEO chains at interfaces.[8,15] The polymer shell around the magnetite nanoparticles represents a combination of several of these systems, suggesting that lattice calculations should be able to provide information about hydrophobic domain formation in the shell for comparison to the results of the SANS experiments.

## 3.2 Experimental

### 3.2.1 Materials

Polyacrylic acid (50 wt% in water, $M_w$ = 5000), iron(III) chloride hexahydrate (97%), iron(II) chloride tetrahydrate (99%), ammonium hydroxide (28 wt% in water), hydrochloric acid (37 wt% in water), and Tiron (4,5-dihydroxy-1,3-benzene-disulfonic acid, disodium salt monohydrate) were obtained from Sigma-Aldrich (Milwaukee, WI).

Jeffamine XTJ-234 ($CH_3$-O-PEO/PPO-$NH_2$, EO:PO = 6.1:1, $M_w$ = 3000) and Jeffamine XTJ-507 ($CH_3$-O-PEO/PPO-$NH_2$, EO:PO = 1:6.5, $M_w$ = 2000) were obtained as gifts from Huntsman Corporation (Houston, TX). In this work, we consider XTJ-234 to be equivalent to pure PEO and XTJ-507 to be equivalent to pure PPO, and refer to these polymers as PEO-$NH_2$ and PPO-$NH_2$, respectively. Deuterium oxide ($D_2O$) was supplied by Cambridge Isotope Laboratories (Andover, MA).

### 3.2.2 Preparation of Magnetic Fluids

The 16/0, 12/4, and 8/8 magnetic fluids for the SANS experiments were prepared as described in Sections 2.2.2 and 2.2.3. The nomenclature *x/y* refers to a magnetic fluid produced with a graft copolymer in which *x*% of the carboxylic acid groups in the PAA backbone were reacted with PEO chains and *y*% with PPO chains. To prepare the suspensions for the SANS experiments, the magnetic fluids were washed by diluting them to 0.5 wt% $Fe_3O_4$ with distilled water and then concentrating them to 2.5 wt% in a 100,000 molecular weight cutoff centrifugal filter (Millipore). The polymer-coated nanoparticles were retained in the filter while unattached polymer and ionic species were lost in the filtrate until there was no residual mass. This process of dilution and concentration in the filter was repeated four times to fully remove free polymer, which was confirmed by evaporating the filtrate. All three magnetic fluids were diluted to 0.5 wt% $Fe_3O_4$ after washing and then placed on a 0.5 T permanent magnet for one hour to remove any aggregates or uncoated particles. The exact magnetite concentration in the magnetic fluids was determined by iron titration.[16] The final suspensions for SANS were produced by evaporating five 4 mL portions of each magnetic fluid under a flow of nitrogen gas. Each magnetic fluid was then resuspended in 4 mL of five different $H_2O/D_2O$ mixtures of varying composition by mild sonication in a water bath for five minutes. Specifically, each magnetic fluid was resuspended in solvent mixtures of $H_2O$ and $D_2O$ that contained 100, 75, 50, 25, and 0 vol% $H_2O$. The 8/8 magnetic fluid was also prepared in a solvent mixture with 82 vol% $H_2O$.

### 3.2.3 Electron Microscopy Measurements

Transmission electron microscopy (TEM) experiments were performed on a JEOL 2010 (200 kV) instrument. Samples were prepared by evaporating dilute suspensions on a carbon-coated film. The median size and polydispersity of the magnetite particles was determined by measuring 150 particles.

### 3.2.4 SANS Measurements

Small angle neutron scattering experiments were conducted on the NG3 30 m SANS instrument at the National Institute of Standards and Technology (NIST) in Gaithersburg, MD. An unpolarized neutron beam with an average wavelength ($\lambda$) of 6 Å and a wavelength spread ($\Delta\lambda/\lambda$) of 0.11 was used in all scattering experiments. Samples were loaded in quartz cells with a path length of 1 mm. Scattering experiments were conducted on each sample at two sample-to-detector distances (1.33 and 7.00 m) with a lateral detector offset of 0.25 m, yielding a continuous $q$ range of $0.005 \leq q \leq 0.4$ Å$^{-1}$ for each sample. The scattering intensity on the detector was circularly averaged for each scattering angle because the scattering was observed to be isotropic. Scattering from the solvent and empty cell was subtracted by measuring the scattering from pure solvent in an identical cell. The scattering was placed on an absolute scale with the use of standards and software supplied by NIST.

## 3.3 Scattering Theory

### 3.3.1 General Scattering Equations

Small angle neutron scattering experiments on magnetic fluids are complicated by the fact that the neutrons interact with and are scattered by both atomic nuclei and the magnetic dipoles of the atoms. In the absence of an external magnetic field, the magnetic dipoles are randomly oriented in the suspension, and the nuclear and magnetic scattering contributions are additive, with the total coherent scattering intensity $I(q)$ given by[2,3]

$$I(q) = N_p\left(\left|F_N(q)\right|^2 + \tfrac{2}{3}\left|F_M(q)\right|^2\right)S(q) \qquad (3\text{-}1)$$

where $N_p$ is the number density of particles in the suspension, $F_N$ is the nuclear particle form factor, $F_M$ is the magnetic particle form factor, and $S(q)$ is the interparticle structure factor. The $F_N$ and $F_M$ terms are a result of coherent scattering from the particle nuclei and magnetic dipoles and are a function of particle size and shape, while $S(q)$ depends on the pair correlation function between particles (and therefore the interparticle interaction potential). The 2/3 factor that multiplies the magnetic form factor is a result of averaging over all orientations of the magnetic dipole in the absence of a magnetic field.[3] The scattering vector $q$ is related to the scattering angle $\theta$ by

$$q = \frac{4\pi}{\lambda}\sin\left(\frac{\theta}{2}\right) \tag{3-2}$$

Our magnetic fluids consist of magnetite particles coated with a polymer shell and suspended in an aqueous solvent. To derive the scattering for these particles, we must account for the significant polydispersity that was observed by TEM measurements (Section 2.3.3). For a polydisperse system, the total scattering intensity is given by integrating over all particles in the suspension:

$$I(q) = \overline{N}_p\left[\int_0^\infty \left(|F_N(q)|^2 + \tfrac{2}{3}|F_M(q)|^2\right)p(R_c)dR_c\right]S(q) \tag{3-3}$$

In Equation 3-3, the integral is taken over all magnetite core radii, $R_c$, with the scattering intensity multiplied by the normalized probability density $p(R_c)$. TEM measurements have shown that the magnetite core radius can be expressed by a lognormal distribution with the form

$$p(R_c) = \frac{1}{\sqrt{2\pi}\sigma_c R_c}\exp\left[\frac{-1}{2\sigma_c^2}\left(\ln\left(R_c/R_{c,med}\right)\right)^2\right] \tag{3-4}$$

where $R_{c,med}$ (the median core radius) and $\sigma_c$ (the core polydispersity) are parameters that define the distribution. Note that Equation 3-4 contains $R_c$ in the denominator of the normalization factor (as opposed to $R_c/R_{c,med}$) because the integration in Equation 3-3 is with respect to $R_c$. The average particle number density, $\overline{N}_p$, is also a function of the

lognormal probability distribution and $\phi_{mag}$, the total volume fraction of magnetite in the suspension:

$$\overline{N}_p = \frac{\phi_{mag}}{\frac{4}{3}\pi \int_0^\infty R_c^3 p(R_c) dR_c} \tag{3-5}$$

The structure factor $S(q)$ is considered to be an average structure factor that is not affected by polydispersity.[2]

### 3.3.2 Form Factor Models

The form factors (both nuclear and magnetic) are derived by summing over the scattering from all atoms in the particle; the resulting form factors are functions of particle size and shape, allowing $I(q)$ measurements to be used to infer the structure within a particle. The scattering of a material is defined by its scattering length density (SLD), which is a material property related to the stoichiometry, density, nuclear spin state, and magnetization of the material. The nuclear SLD ($\rho_N$) of the compounds in our magnetic fluids is summarized in Table 3-1. In our analysis, we consider the graft copolymer to be equivalent to a single component because the nuclear SLD of PEO ($0.57 \times 10^{-6}$ Å$^{-2}$) and PPO ($0.35 \times 10^{-6}$ Å$^{-2}$) are so similar as to make distinguishing between them by SANS extremely difficult,[4] while PAA ($2.4 \times 10^{-6}$ Å$^{-2}$) makes up less than 10 vol% of the graft copolymer. We therefore use a volume average SLD for the polymer based on the composition, resulting in a nuclear SLD of $0.76 \times 10^{-6}$ Å$^{-2}$ for the 16/0, 12/4, and 8/8 polymers. We also assume that solvents composed of mixtures of $H_2O$ and $D_2O$ have a nuclear SLD given by a weighted average of the $H_2O$ and $D_2O$ volume fractions.

The magnetic SLD ($\rho_M$) of a material is given by[17,18]

$$\rho_M = b_M M_s \tag{3-6}$$

**Table 3-1.** Scattering length densities for materials in the magnetic fluids

| Material | Nuclear SLD ($10^{-6}$ Å$^{-2}$) | Magnetic SLD ($10^{-6}$ Å$^{-2}$) |
|---|---|---|
| $Fe_3O_4$ | 6.96 [a] | 1.36 |
| Polymer | 0.76 [a] | - |
| $H_2O$ | -0.56 [a] | - |
| $D_2O$ | 6.36 [a] | - |

a) Nuclear SLD value from ref. [Shen, 2001 #187].

where $b_M$ is the magnetic scattering length per Bohr magneton (= $2.318 \times 10^{14}$ $T^{-1}m^{-2}$) and $M_s$ is the saturation magnetization of the bulk material (in T). As the polymer shell and the $H_2O$ and $D_2O$ solvents have a negligible magnetization, $\rho_M$ is zero for these components, as shown in Table 3-1. Using a value of 0.60 T (87 emu/g) for the saturation magnetization, we calculated a magnetic SLD for magnetite of $1.36 \times 10^{-6}$ Å$^{-2}$, which is consistent with other studies.[18]

The form factor for a particle is derived by summing the scattering amplitudes of all atoms in the particle, weighted by the phase shift corresponding to the particle position, $\exp(iq \cdot r)$.[17] It is given by the volume integral

$$F(q) = \int_V (\rho(r) - \rho_s)\exp(i \cdot qr)d^3r \qquad (3\text{-}7)$$

where $\rho(r)$ is the scattering length density of the atoms at relative position $r$ and $\rho_s$ is the scattering length density in the solvent (outside the particle). Equation 3-7 yields the nuclear form factor $F_N$ if the integral is taken with the nuclear SLD profile $\rho_N$(r), while it yields the magnetic form factor $F_M$ with the magnetic SLD profile $\rho_M$(r). For a particle with spherical symmetry, Equation 3-7 can be converted to spherical coordinates and made real:[19]

$$F(q) = 4\pi\int_0^\infty (\rho(r) - \rho_s)\frac{\sin(qr)}{qr}r^2 dr \qquad (3\text{-}8)$$

The nuclear and magnetic form factors can then be derived for any spherically symmetric particle with an assumed $\rho_N(r)$ or $\rho_M(r)$ profile.

In this study, we consider two different models for the particle structure, as shown in Figure 3-1. In both cases, the core of radius $R_c$ consists of pure magnetite surrounded by a hydrated polymer shell of length $L_1$. In case (a), the solvent penetration is assumed to be homogenous, with a constant solvent volume fraction of $\phi_{s1}$ in the shell. In this case, the nuclear SLD of the polymer shell ($\rho_{N1}$) is given by a weighted average of the solvent and polymer volume fractions in the shell:

$$\rho_{N1} = \phi_{s1}\rho_{Ns} + (1-\phi_{s1})\rho_{Np} \tag{3-9}$$

where $\rho_{Ns}$ is the nuclear SLD of the solvent and $\rho_{Np}$ is the nuclear SLD of the polymer.

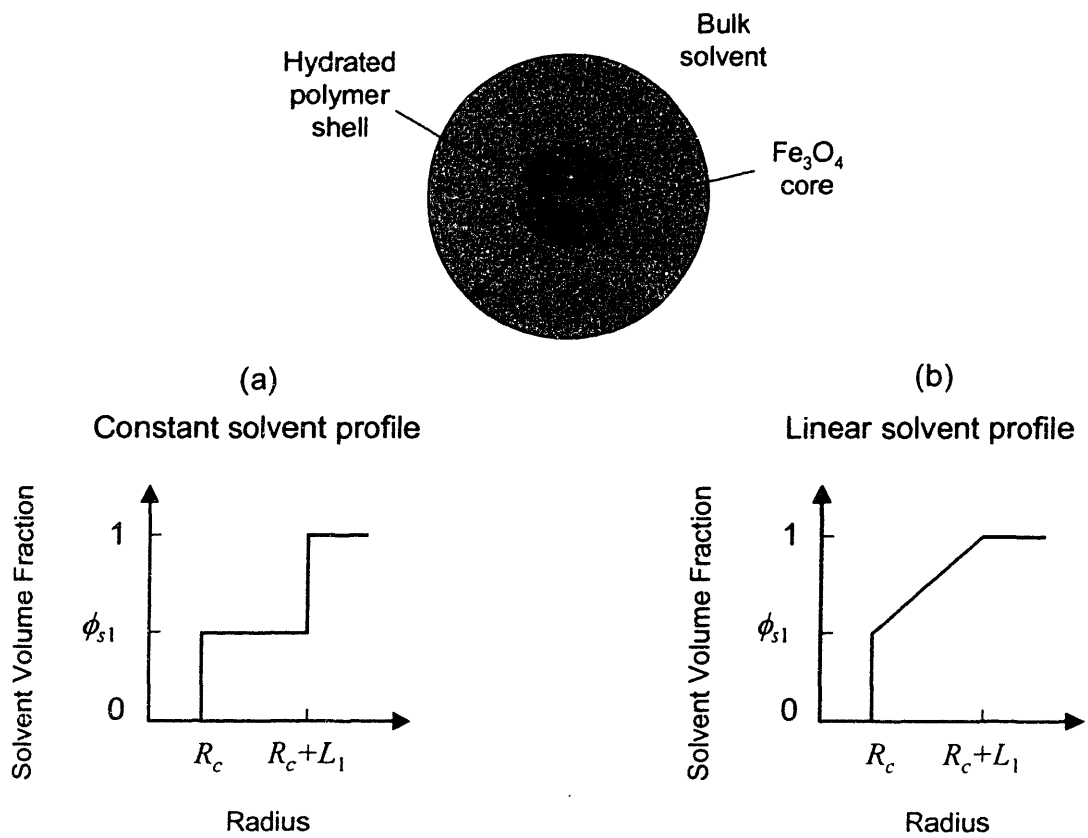


**Figure 3-1.** Solvent penetration models for the magnetic nanoparticle form factor. (a) Constant solvent volume fraction in the polymer shell. (b) Linear solvent volume fraction profile.

Using Equation 3-8 with the constant solvent profile yields the nuclear form factor:

$$F_N(q) = \frac{4\pi}{q}\left[R_c^2(\rho_{Nc} - \rho_{N1})j_1(qR_c) + (R_c + L_1)^2(\rho_{N1} - \rho_{Ns})j_1(q(R_c + L_1))\right] \quad (3\text{-}10)$$

where $\rho_{Nc}$ is the nuclear SLD of the magnetite core and $j_1(x) = (\sin x - x\cos x)/x^2$ is a first-order spherical Bessel function. This is the well-known form factor for core-shell particles.[2,4]

In case (b) in Figure 3-1, a linear solvent profile is assumed, with the solvent volume fraction varying from 1 at the exterior of the shell to $\phi_{s1}$ at the magnetite surface. In this case, the $\rho_N$(r) profile is calculated from the solvent volume fraction profile with a volume fraction-weighted average of the polymer and solvent nuclear SLD at each point. With this profile, the nuclear form factor is calculated with Equation 3-8 as

$$F_N(q) = \frac{4\pi}{q}\left\{R_c^2\left(\rho_{Nc} - \frac{\rho_{N1}(R_c + L_1) - \rho_{Ns}R_c}{L_1}\right)j_1(qR_c)\right.$$

$$+\left(\frac{\rho_{Ns} - \rho_{N1}}{L_1}\right)\left(\frac{2(R_c + L_1)}{q^2}\sin(q(R_c + L_1)) - \frac{2R_c}{q^2}\sin(qR_c)\right)$$

$$+\left(\frac{\rho_{Ns} - \rho_{N1}}{L_1}\right)\left(-\frac{q^2(R_c + L_1)^2 - 2}{q^3}\cos(q(R_c + L_1)) + \frac{q^2R_c^2 - 2}{q^3}\cos(qR_c)\right)$$

$$\left.+(R_c + L_1)^2\left(\frac{\rho_{N1}(R_c + L_1) - \rho_{Ns}R_c}{L_1} - \rho_{Ns}\right)j_1(q(R_c + L_1))\right\} \quad (3\text{-}11)$$

where $\rho_{N1}$ is the nuclear SLD in the polymer shell at the magnetite surface.

The polydispersity of the particles also affects the polymer shell thickness due to curvature effects. For a constant polymer grafting density, the shell thickness increases with increasing core radius because of decreasing curvature.[20,21] In Section 2.3.5, we calculated the shell thickness of 16/0 particles using a discrete blob model.[20] In the size range of our nanoparticles, this model can be approximated as

$$L_1 = \frac{L_{1,med}}{R_{c,med}^{0.24}} R_c^{0.24} \tag{3-12}$$

where $L_{1,med}$ is the shell thickness of a particle with the median core radius. While this relationship was derived for 16/0 particles that contain only PEO side chains, we also apply it to the 12/4 and 8/8 particles. In our analysis, the nuclear form factor is therefore given by either Equation 3-10 or 3-11 (depending on the solvent penetration model) with $L_1$ given by Equation 3-12.

The magnetic form factor is simpler to calculate, as the polymer and solvent are both nonmagnetic. The form factor for spherical particles is used, with the one caveat that we account for a nonmagnetic shell of thickness $\delta$ = 8.3 Å at the exterior of the magnetite core.[2] This nonmagnetic layer is usually ascribed to the disruption of the electronic structure of the atoms at the surface.[22] The magnetic form factor is given by

$$F_M(q) = \frac{4\pi}{q}(R_c - \delta)^2 \rho_{Mc} j_1(q(R_c - \delta)) \tag{3-13}$$

where $\rho_{Mc}$ is the magnetic SLD of the magnetite core. As a result of the low magnetic SLD of magnetite compared to the nuclear SLD, the magnetic scattering is 1-2 orders of magnitude lower than the nuclear scattering in all solvents used in this study; we include it here for completeness.

### 3.3.3 Structure Factor Model

The structure factor S($q$), which accounts for interparticle interactions, may be important for our nanoparticles as dynamic light scattering (DLS) studies have shown that they have a tendency to aggregate (Section 2.3.5). The magnetic fluids used in this study were placed on a magnet to remove any large aggregates before SANS measurements, although trace amount of aggregates were still detected afterwards. This may be a result of attractive interactions between particles. To account for attractive interactions, we used the Ornstein-Zernike structure factor, which has the form[23]

$$S(q) = 1 + \frac{S_o}{1 + (q\zeta)^2} \tag{3-14}$$

where $S_o$ is related to the osmotic compressibility of the suspension (increases with increasing attractive force) and $\zeta$ is the correlation length of the interaction. This structure factor has been applied successfully to systems of PEO-containing microemulsions that tend to aggregate[24] and should be appropriate for our PEO and PPO coated particles.

### 3.3.4 SANS Fitting Approach

All magnetic fluids used in this study were prepared in five $H_2O/D_2O$ mixtures with compositions ranging from pure $H_2O$ to pure $D_2O$. Previous studies have shown that the level of deuteration in the aqueous solvent does not significantly affect the structure of Pluronic micelles, composed of PEO and PPO polymers like our graft copolymer.[4] The mixtures of $H_2O$ and $D_2O$ are used to vary the solvent SLD without changing the hydration of the polymer shell or the structure of the particles. This method of contrast variation allowed isolation of different parts of the nanoparticles by matching the solvent SLD to either the graft copolymer (isolating scattering from the magnetite core) or the magnetite core (isolating scattering from the solvated shell). The data fitting approach used a single contrast-matched solvent to extract the core parameters and a global fit over a range of solvent conditions to determine the shell and interparticle parameters. By using a global fit, we simultaneously fit several parameters while keeping each parameter constrained at a constant value throughout the entire solvent SLD range.

A chi-squared fit was used in all data fitting procedures, as the NIST software provided estimates of the standard deviation of the measured intensity at each point ($\sigma_i$). A chi-squared fit is a weighted least-squares fit in which each square-error is divided by the variance. The parameter optimization therefore involves minimization of $\chi^2$, defined as

$$\chi^2 = \sum_{i=1}^{N} \frac{\left(I_{i,meas} - I_{i,pred}\right)^2}{\sigma_i^2} \tag{3-15}$$

where $I_{i,data}$ is the measured scattering intensity at $q_i$ and $I_{i,pred}$ is the predicted intensity given by Equation 3-3. In global fits, the sum was taken over all data series. Generally, $\chi^2/N < 1$ is required for a good fit in which the model is within the measurement error for all points,[25] although this is not always possible for global fits of different solvent SLD.[26] Parameter estimation (via minimization of $\chi^2$) was performed with a custom MATLAB code using the "lsqnonlin" nonlinear least-squares optimization function. Data fitting was limited to points with $q \leq 0.1$ Å$^{-1}$ as the scattering above this range was primarily incoherent background.

## 3.4 SANS Results

### 3.4.1 Determination of Core Parameters

Previous experiments using transmission electron microscopy (TEM) and magnetization measurements demonstrated that the magnetite core is approximately spherical and polydisperse (Chapter 2). No significant differences were observed in the core size as the PEO:PPO side chain ratio was varied, suggesting the hydrophobicity of the polymer did not affect the magnetite formation process. We obtained a similar result for the magnetic fluids used in our SANS experiments, as TEM images showed that the particles had a median core diameter of 7.3 nm ($R_{c,med}$ = 36 Å) and a polydispersity, $\sigma_c$, of 0.30, with no significant differences between the 16/0, 12/4, and 8/8 magnetic fluids. Our SANS results also support this hypothesis. Figure 3-2 shows scattering data for the three types of magnetic fluids in a solvent composed of 75% $H_2O$ and 25% $D_2O$. For this mixture, $\rho_{Ns} = 1.17 \times 10^{-6}$ Å$^{-2}$, which is close to the SLD of the graft copolymers ($0.76 \times 10^{-6}$ Å$^{-2}$). The polymer is approximately contrasted in this solvent ($\rho_{Ns} \approx \rho_{Np}$) and scattering becomes purely dependent on the magnetite core, as shown by Equation 3-10. Figure 3-2 shows that at $q > 0.03$ Å$^{-1}$, the scattering of the 16/0, 12/4, and 8/8 particles coincide, suggesting that the magnetite cores are essentially identical. The scattering at lower $q$, where larger scale structures dominate, increases somewhat from 16/0 to 8/8,

which may be due to differences in interparticle interactions. Interactions, characterized by the structure factor $S(q)$, will be discussed further in the next section.

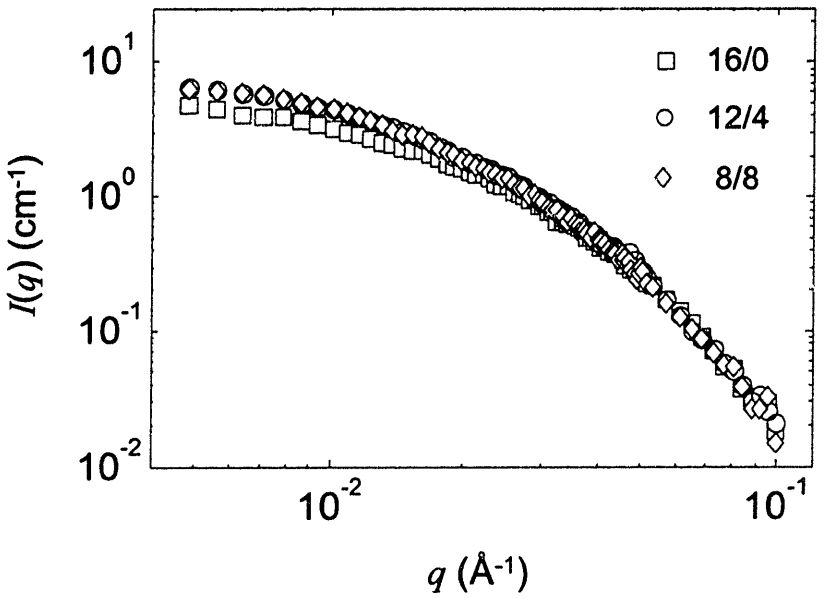


**Figure 3-2.** Neutron scattering data for magnetic fluids in 75% $H_2O$ / 25% $D_2O$. The scattering from 16/0, 12/4, and 8/8 particles is similar at $q \geq 0.03$ Å$^{-1}$, suggesting the $Fe_3O_4$ core size is similar for all particles.

To deduce the size of the $Fe_3O_4$ core, we measured the scattering from an 8/8 magnetic fluid in a solvent composed of 82% $H_2O$ and 18% $D_2O$ that has a nuclear SLD of $0.69 \times 10^{-6}$ Å$^{-2}$. In this solvent, the polymer shell is therefore contrast-matched, as the ratio $(\rho_{Nc} - \rho_{Np})/(\rho_{Np} - \rho_{Ns}) = 80$, meaning scattering from the core will contribute ~80 times more to the nuclear form factor than scattering from the shell. Substituting $\rho_{Np} = \rho_{Ns} = \rho_{Nl}$ into either Equation 3-10 or 3-11 yields the nuclear form factor for a homogeneous sphere:

$$F_N(q) = \frac{4\pi}{q} R_c^2 (\rho_{Nc} - \rho_{Ns}) j_1(qR_c) \tag{3-16}$$

This equation, in combination with the magnetic form factor (which is not affected by the level of solvent deuteration), defines the scattering intensity in this contrast-matched solvent.

Figure 3-3 shows the scattering from 8/8 particles in the 82% $H_2O$ solvent selected to contrast-match the polymer shell. The scattering data show a pattern consistent with polydisperse spheres, in that oscillations in the data are smeared by the broad distribution of core sizes.[2] Due to the effect of particle interactions, we limited our fit of the scattering to the region $0.03 < q < 0.1$ Å$^{-1}$. Because scattering depends only on the core, fitted parameters were $R_{c,med}$, $\sigma_c$, and $\phi_{mag}$, where $R_{c,med}$ and $\sigma_c$ define the lognormal core size distribution and $\phi_{mag}$ is the total volume fraction of magnetite in the magnetic fluid. Figure 3-3 shows that the best fit is excellent (in the fitted region), with $\chi^2/N = 0.88$. Error bars are not shown in the figure but are smaller than the symbols over the entire data range. The scattering is underpredicted at low $q$ (outside the fitted range) due to interparticle interactions that will be discussed in more detail in the next section. The optimal values of the fitted parameters were $R_{c,med} = 24.1$ Å, $\sigma_c = 0.490$, and $\phi_{mag} = 9.29 \times 10^{-4}$. $\phi_{mag}$ is effectively a scale factor for the scattering and was acceptably close to the magnetite volume fraction in the magnetic fluid as measured by iron titration ($1.09 \times 10^{-3}$). The predicted core size, however, is significantly different than that determined

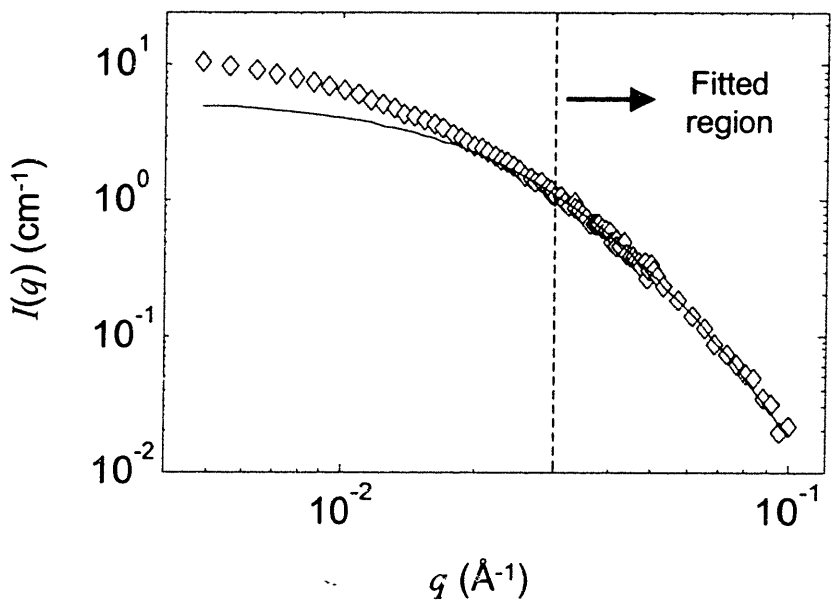


**Figure 3-3.** Neutron scattering data for the 8/8 magnetic fluid in 82% $H_2O$ / 18% $D_2O$. This solvent is selected to match the scattering length density of the graft copolymer. The solid line represents the best fit to the data in the range $0.03 < q < 0.1$ Å$^{-1}$ by varying $R_{c,med}$, $\sigma_c$, and $\phi_{mag}$.

by electron microscopy. The median core radius from SANS is 33% lower than the value of 36 Å determined from TEM images of the same sample. The core polydispersity, on the other hand, is 63% higher than the value of 0.30 from TEM.

The source of this core size discrepancy is uncertain. The median radius from TEM is relatively accurate, as it was a direct measurement of the size and previous results in Chapter 2 showed that the radius from TEM was consistent with estimates from magnetization measurements. Previous measurements of the core polydispersity ranged from 0.30 from TEM to 0.35 from magnetization measurements – still equivalent to a 40% overprediction by SANS. The size discrepancy is not an artifact of limiting the data fitting to higher $q$, as fitting the core size over the entire data range led to an even smaller core size and a higher polydispersity that were clearly erroneous. A more likely explanation is that the differences are due to irregularities in the shape of the magnetic particles. A close examination of a TEM image of the nanoparticles (Figure 2-6a) shows that while some particles are spherical, others are more ellipsoidal in nature. In addition, some particles have angular surfaces, particularly in the high resolution TEM image in Figure 2-7. In visual measurements of the diameter of ellipsoidal particles from TEM images, an average of the two axes was used, which could explain the differences according to Shen et. al.;[2] they observed this phenomenon to a lesser extent in their SANS study of magnetic particles, in that they underpredicted $R_{c,med}$ by 11% and overpredicted $\sigma_c$ by 15% with SANS, which they attributed to the ellipsoidal shape of the particles. Repeating the fit of the data in Figure 3-3 with a form factor for polydisperse ellipsoids (with radii $a$, $a$, and $b$) resulted in the median primary radius $a_{med}$ increasing to 33.2 Å with an axial ratio $b/a$ of 0.50, but excessive polydispersity was still observed ($\sigma_c$ = 0.480) and the quality of the fit did not improve. The core size discrepancy is probably a result of a combination of effects (irregular shape and angular surfaces) and illustrates the difficulty in applying SANS to somewhat irregular polydisperse objects.

### 3.4.2 Global Fit of Shell Parameters

The hydration profile of the polymer shell around the nanoparticles and the parameters that define the interparticle interactions were determined by a global fit of the

SANS data for each type of particle in five aqueous solvents with a varying level of deuteration. The size of the $Fe_3O_4$ core and the magnetite volume fraction determined in Section 3.4.1 were held constant for all particles. Thus, the globally-fitted parameters were the shell thickness of a median particle ($L_{1,med}$), the solvent volume fraction in the shell ($\phi_{s1}$), and two parameters that characterized interparticle interactions ($S_o$ and $\zeta$). Two global fits were performed for each type of particle: one with the constant solvent profile shown in Figure 3-1a and one with the linear solvent profile in Figure 3-1b. In the former case, $\phi_{s1}$ is the solvent volume fraction throughout the polymer shell, while in the latter case it is the solvent volume fraction at the $Fe_3O_4$ interface. Simultaneously fitting four parameters to five data series ensures a higher level of confidence in the parameters. Even though the core parameters determined by contrast matching the polymer shell ($R_{c,med}$ = 24.1 Å, $\sigma_c$ = 0.490, and $\phi_{mag} = 9.29 \times 10^{-4}$) were somewhat different than those observed by electron microscopy, our estimates show that $L_{1,med}$, $\phi_{s1}$, $S_o$, and $\zeta$ are relatively independent of the core shape and size. For example, if we modeled the particles as core-shell ellipsoids rather than spheres, our globally-fitted values of $L_{1,med}$ and $\phi_{s1}$ changed by less than 2%.

In Figure 3-4a, the scattering intensity of the 16/0 particles in the five solvents ranging from $H_2O$ to $D_2O$ is shown. Error bars on the scattering data are not shown in the figure but lie within the size of the data points. For clarity, the scattering curves in the various solvents are offset by factors of ten going from $H_2O$ to $D_2O$. The actual order of the scattering intensities as $q \rightarrow 0$ in the various solvents is 100% $H_2O$ > 0% $H_2O$ > 75% $H_2O$ > 25% $H_2O$ > 50% $H_2O$. This itself is evidence of the scattering from the polymer shell, as bare magnetite particles would show decreasing scattering with increasing solvent deuteration. The shape of the scattering data also shows evidence of the polymer shell. The $H_2O$-rich solvents, where the scattering is primarily from the $Fe_3O_4$ core, show a monotonic decay consistent with polydisperse spheres. The scattering in the $D_2O$-rich solvents, which is primarily due to the polymer shell, shows some evidence of a shoulder, although very distinguishable features are smeared by the high polydispersity.

The best global fit of the 16/0 scattering data assuming a constant solvent volume fraction is also shown in Figure 3-4a. The optimal values of the four fitted parameters from this fit are given in Table 3-2. For this fit of the 16/0 particles, $\chi^2/N = 10.6$, which implies that the predicted scattering was outside the measurement uncertainty for some points. Regardless, the fit is generally acceptable and seems to capture the important features of the data. The fit is weakest at high $q$ in the $D_2O$-rich solvents, which is probably caused by our use of a core-shell model for the particle structure, resulting in a predicted $q^{-4}$ scattering dependence at high $q$. Blob structure in the polymer shell (internal structure not considered in our development) has been reported to cause the scattering to decay at approximately $q^{-2}$ at $q$ greater than 0.06-0.10 $Å^{-1}$.[27-29], which is the region in which our predicted scattering begins to diverge in the $D_2O$-rich samples. As we limited our fit to $q < 0.1$ $Å^{-1}$, neglecting blob scattering should not lead to significant errors.

The scattering data for the 16/0, 12/4, and 8/8 particles are compared in parts a-c of Figure 3-4. In these figures, the fit to the scattering assuming a constant solvent volume fraction in the polymer shell is also shown; the optimal values of the fitted parameters for this fit and the total $\chi^2$ error are summarized in Table 3-2 for the three magnetic fluids. The constrained core parameters are also shown in italics, along with values determined by other experimental methods. The fit is generally good for 16/0 and 12/4 particles, with a $\chi^2/N$ value of 10.6 and 6.40, respectively. The global fit of the 8/8 data is somewhat worse, with a $\chi^2/N$ value of 43.2. A comparison of the scattering curves in Figure 3-4 shows that while the fit to the scattering from the 16/0 and 12/4 particles is clearly superior to that from the 8/8 particles, the fit to the 8/8 particles seems at least to capture the most important scattering features. The main source of error from the 8/8 particles appears to be from the scattering in $D_2O$-rich solvents at intermediate $q$, where the shoulder due to shell scattering is not captured perfectly. Regardless, our model does predict the general trends in the scattering, such as the increase in scattering intensity in pure $D_2O$ as $q \rightarrow 0$ from 16/0 to 8/8.

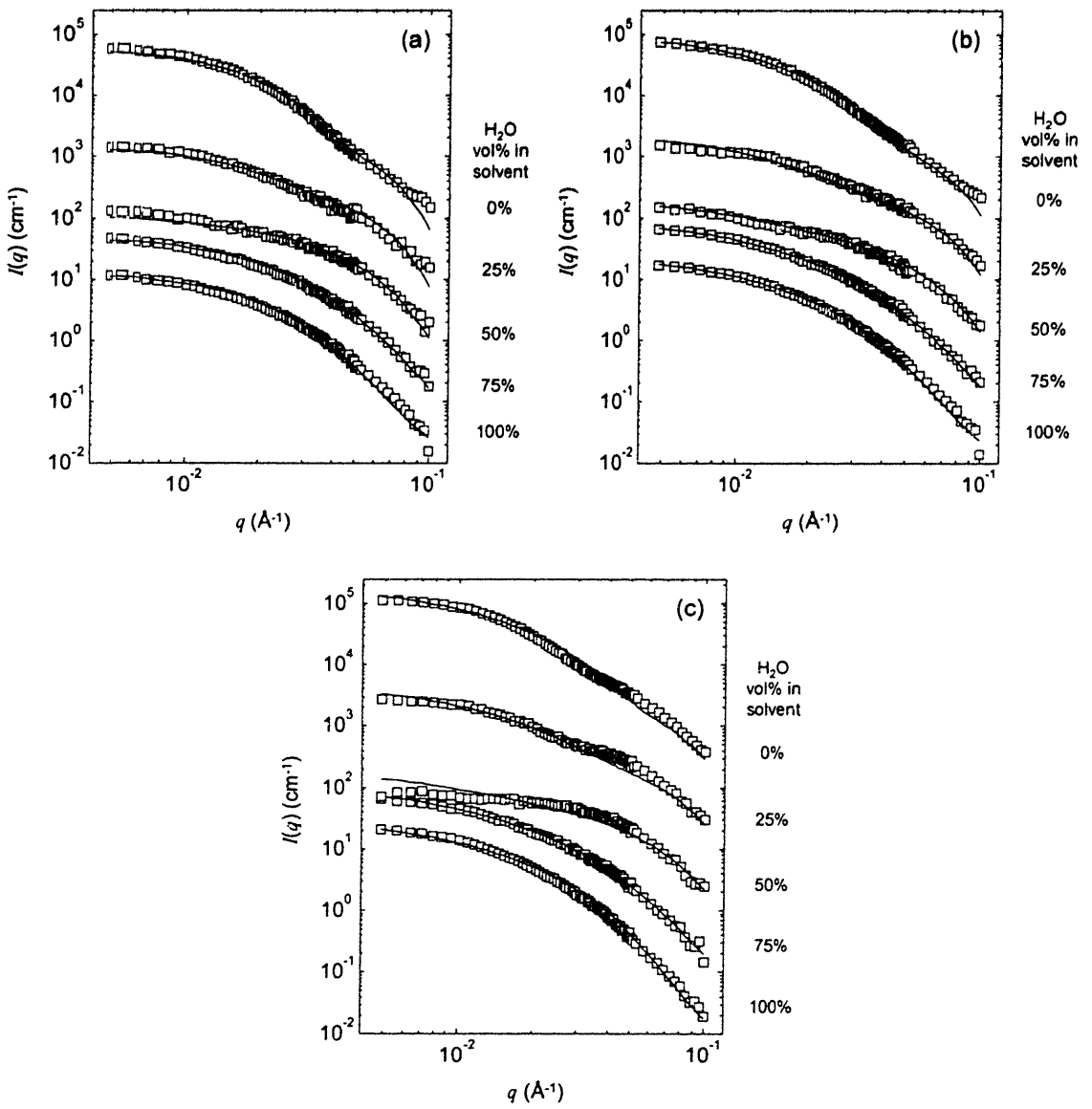


**Figure 3-4.** Global fit of neutron scattering from the magnetic fluids with the constant solvent model (Figure 3-1a). Data are shown for the (a) 16/0, (b) 12/4, and (c) 8/8 magnetic fluids in five aqueous solvents with a varying level of deuteration. The curves are offset for clarity by factors of: 100% $H_2O$ (×1), 75% $H_2O$ (×10), 50% $H_2O$ (×100), 25% $H_2O$ (×$10^3$), 0% $H_2O$ (×$10^4$). The solid lines represent a global fit to the five data series over the whole $q$ range by varying $L_{1,med}$, $\phi_{s1}$, $S_o$, and $\zeta$. The predicted scattering was calculated with the form factor in Equation 3-10.

**Table 3-2.** Results of global fit assuming a **constant** solvent volume fraction in shell

| | Values Inferred from SANS Data | | | Value Measured by Other Techniques |
|---|---|---|---|---|
| | 16/0 | 12/4 | 8/8 | |
| $\chi^2/N$ | 10.6 | 6.40 | 43.2 | |
| $R_{c,med}$ (Å) | *24.1* | *24.1* | *24.1* | 36 [a] |
| $\sigma_c$ | *0.490* | *0.490* | *0.490* | 0.30 [a] – 0.35 [b] |
| $\phi_{mag}$ | $9.29 \times 10^{-4}$ | $9.29 \times 10^{-4}$ | $9.29 \times 10^{-4}$ | $1.09 \times 10^{-3}$ [c] |
| $L_{1,med}$ (Å) | 45.3 | 39.8 | 33.3 | 94 [d] |
| $\phi_{s1}$ | 0.768 | 0.720 | 0.537 | - |
| $S_o$ | 0.237 | 1.08 | 1.35 | - |
| $\zeta$(Å) | 130 | 124 | 133 | - |
| $m_p/m_m$ | 0.477 | 0.452 | 0.543 | 0.80 [e] |

a) Measured by TEM.
b) Measured by magnetization analysis.
c) Measured by iron titration.
d) Measured by dynamic light scattering.
e) Measured by thermogravimetric analysis.

In Table 3-2, a clear trend is seen in the fitted parameters $L_{1,med}$ and $\phi_{s1}$ that characterize the solvation of the polymer shell, in that the shell appears to contract and become less solvated from 16/0 to 8/8 particles. This result is logical, as the 16/0 graft copolymer contains only hydrophilic PEO side chains, while the 12/4 and 8/8 particles have increasing numbers of hydrophobic PPO side chains substituted for PEO. The addition of PPO side chains has an effect on hydration that is greater than simple replacement of PEO chains, in that PPO side chains also reduce the ability of water to hydrate the PEO chains, decreasing the $H_2O$/EO molar ratio from 9.3 for the 16/0 particles to 5.6 for the 8/8 particles. These values compare with Pluronic micelles, which typically have an $H_2O$/EO ratio of 3-9 depending on composition and temperature.[6] Even the most hydrophobic 8/8 particles still contain 54 vol% water in the polymer shell according to our model, which is reasonable, as these particles remained stable in water up to 80 °C (Section 2.4). If the solvent volume fraction approached zero, the particles

would flocculate. The shell thickness from SANS was significantly smaller than was observed with dynamic light scattering (94 Å). In addition, the decrease in shell thickness when PPO side chains were added that we observed with SANS was not seen with dynamic light scattering (Section 2.3.5); however, SANS is a much more sensitive tool to observe subtle changes in the shell structure.

A significant trend in the parameters that characterize interparticle interactions is also evident in Table 3-2. The value of $\zeta$, which characterizes the length scale of particle interactions, was approximately constant for the 12/4 and 8/8 particles at values of 124 and 133 Å, respectively. The 16/0 fit, however, showed an extremely weak dependence on the structure factor and many pairs of $S_o$ and $\zeta$ values were able to fit the data equally well. To maintain a constant basis of comparison, we fixed the value of $\zeta$ for the 16/0 particles at 130 Å – a value consistent with the best-fit value for the other particles. The exact significance of this correlation length is uncertain but the relatively low value compared to the particle size suggests it probably arises from small particle aggregates. The value of $S_o$, related to the osmotic compressibility, increases from 16/0 to 8/8 particles, meaning that adding hydrophobic PPO side chains caused increased interparticle attraction. The magnitude of this attraction is relatively small, which is consistent with our observation that the particles do not flocculate. Figure 3-5 shows the structure factor $S(q)$ that arises from the fitted $S_o$ and $\zeta$ values in Table 3-2. $S(q) \approx 1$ for the 16/0 particles throughout the entire $q$ range. Attractive interactions for the 16/0 particles are expected to be extremely low as PEO is well solvated and should provide a good steric barrier. A substantial increase in $S(q)$ was observed upon adding PPO side chains, although the actual $S(q)$ remains low compared to that in many other systems. For example, fatty acid-coated aqueous magnetic fluids that showed significant aggregation had a value of $S(q) \approx 600$ at low $q$.[2] Our decision to fit the core parameters in the range $0.03 < q < 0.1$ Å$^{-1}$ is validated by Figure 3-5, which shows that $S(q)$ had diminished to less than 1.08 for all particles by $q = 0.03$ Å$^{-1}$.

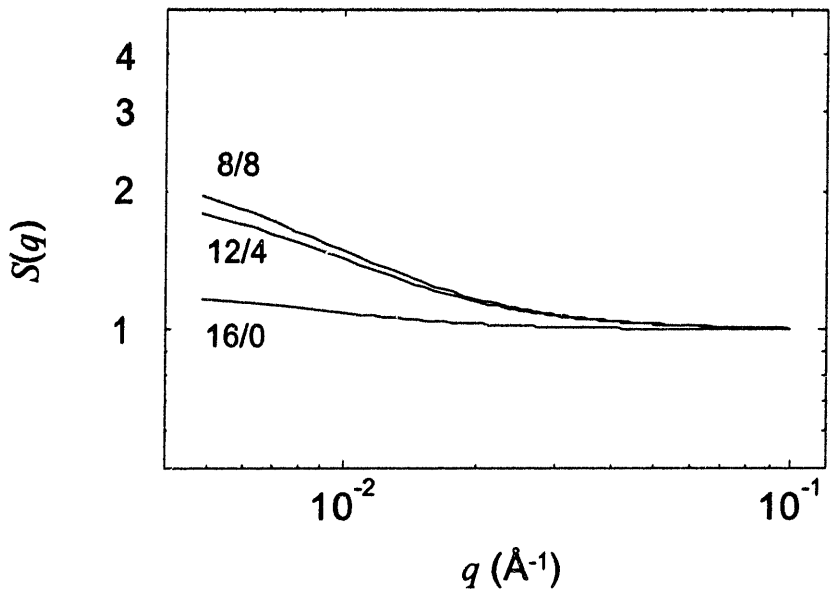


**Figure 3-5.** Comparison of predicted structure factor for the magnetic fluids. The structure factor increases with increasing PPO content because of attractive interactions.

The amount of polymer bound to the particles predicted by SANS (shown as the polymer:magnetite mass ratio $m_p/m_m$ in Table 3-2) is lower than what was observed by other methods. This value is a dependent parameter because the analysis fixed the core size and fit both the size and water content of the shell. The values from SANS (accounting for polydispersity) ranged from 0.45-0.54, while thermogravimetric analysis of the particles gave a value of approximately 0.8 for all particles (Section 2.3.2). The most likely explanation for this discrepancy is that the model for the particles (Figure 3-1) assumed spherical symmetry, in that it forced the polymer to be equally distributed around the strongly scattering $Fe_3O_4$ core. It is possible that the polymer is not equally distributed; for example, if several of the graft copolymer molecules are attached by only a few carboxylic acid groups near the end of the backbone, the polymer shell may be asymmetric with thicker and thinner regions. IR spectroscopy has indicated that a significant portion of the PAA backbone may not be attached to the $Fe_3O_4$ surface. We should therefore view the shell thickness as an average value.

The best fit to the same neutron scattering data with the linear solvent penetration model (Figure 3-1b) is shown in Figure 3-6 for the 16/0, 12/4, and 8/8 magnetic fluids,

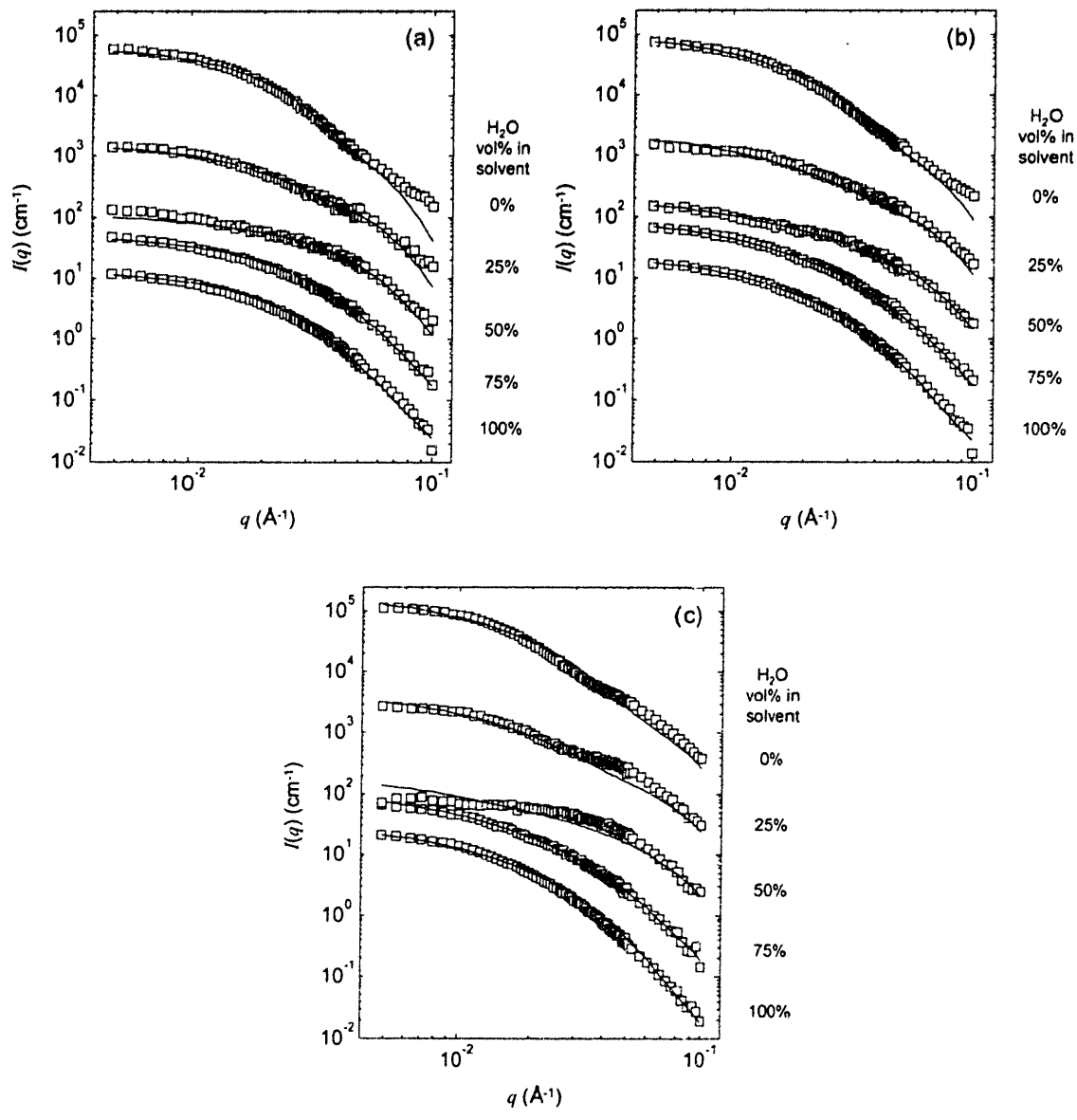


**Figure 3-6.** Global fit of neutron scattering from the magnetic fluids with the linear solvent penetration model (Figure 3-1b). Data are shown for the (a) 16/0, (b) 12/4, and (c) 8/8 magnetic fluids in five aqueous solvents with a varying level of deuteration. The curves are offset by factors of ten for clarity and the solid lines represent a global fit to the five data series over the whole $q$ range by varying $L_{1,med}$, $\phi_{s1}$, $S_o$, and $\zeta$. The predicted scattering was calculated with the form factor in Equation 3-11.

while the values of the best-fit parameters for this model are given in Table 3-3. A comparison of the fitted parameters from the constant solvent (Table 3-2) and linear solvent cases shows that changing the solvent penetration model did not have a strong effect on the quality of fit, although the linear solvent penetration was slightly worse in all cases. This result is somewhat unusual as the linear solvent penetration is expected to be a more physically realistic model for the solvent structure. In both cases, however, the trend of decreasing shell thickness and decreasing solvation was observed going from 16/0 to 8/8 particles. $\phi_{s1}$ is always higher for the constant solvent case because it represents the average solvent volume fraction between the magnetite surface and the outer edge of the shell (where the volume fraction must equal unity). For the same reason, $L_{1,med}$ is always higher for the linear solvent penetration model. Very similar results were seen for the structure factor parameters in both models.

**Table 3-3.** Results of global fit assuming a **linear** solvent volume fraction in shell

| | **Values Inferred from SANS Data** | | | **Value Measured by Other Techniques** |
|---|---|---|---|---|
| | **16/0** | **12/4** | **8/8** | |
| $\chi^2/N$ | 11.6 | 10.4 | 57.8 | |
| $R_{c,med}$ (Å) | *24.1* | *24.1* | *24.1* | 36 [a] |
| $\sigma_c$ | *0.490* | *0.490* | *0.490* | 0.30 [a] – 0.35 [b] |
| $\phi_{mag}$ | $9.29 \times 10^{-4}$ | $9.29 \times 10^{-4}$ | $9.29 \times 10^{-4}$ | $1.09 \times 10^{-3}$ [c] |
| $L_{1,med}$ (Å) | 61.5 | 50.8 | 41.0 | 94 [d] |
| $\phi_{s1}$ | 0.632 | 0.521 | 0.185 | - |
| $S_o$ | 0.210 | 1.13 | 1.47 | - |
| $\zeta$(Å) | 130 | 129 | 140 | - |
| $m_p/m_m$ | 0.482 | 0.442 | 0.523 | 0.80 [e] |

a) Measured by TEM.
b) Measured by magnetization analysis.
c) Measured by iron titration.
d) Measured by dynamic light scattering.
e) Measured by thermogravimetric analysis.

With both the constant and linear solvent penetration models, the predicted median shell thickness was lower than the value of 94 Å (9.4 nm) measured by dynamic light scattering (Section 2.3.5), as compared to 61.5 Å determined by SANS for the 16/0 particles (assuming a linear solvent penetration). There are two possible explanations for this difference: the underpredicted mass of bound polymer and our use of an underpredicted core radius in the global fitting. Calculations based on scaling theory[20] and discussed in Section 2.3.5 showed that 16/0 particles with $m_p/m_m = 0.8$ and $R_c = 36$ Å should have a shell thickness of 87 Å assuming that all PEO chains are end-grafted to the magnetite spheres. This shell thickness is very similar to what we observed with dynamic light scattering (94 Å). However, with the mass of bound polymer and core radius determined by SANS ($m_p/m_m$ = 0.48 and $R_c$ = 24 Å), the predicted value of the shell thickness falls to 69 Å – much closer to the value of 61.5 Å from our global fit. This result suggests that our SANS analysis is internally consistent in its extraction of the particle dimensions. The discrepancies between the dimensions from SANS and from other methods are most likely a result of our application of a simple model for the particle shape to particles that seem to contain significant shape irregularities. Regardless, neutron scattering does give us experimental insight into the solvation structure within the polymer shell that cannot be easily measured with other techniques.

## 3.5 Self-Consistent Lattice Calculations

### 3.5.1 Overview of Theory

Self-consistent lattice calculations, performed by Per Linse (University of Lund, Sweden), were used to predict the solvation structure of our nanoparticles by estimating the volume fraction profiles of PEO, PPO, and water in the polymer shell. Lattice theory has been used extensively to model systems composed of PEO and PPO in water.[8-14,30] This technique provided a method for predicting the behavior of PEO and PPO chains in the shell, which we could not observe with neutron scattering because of the similarities in nuclear scattering length densities of these materials. In addition, the predicted water penetration profile from lattice calculations could be compared to that from neutron scattering experiments, providing a method of validating our SANS analysis. A detailed

discussion of the application of this theory to multicomponent polymer mixtures at spherical interfaces can be found in the literature;[8,13] here the critical concepts are reviewed.

In self-consistent lattice calculations of PEO and PPO in water, the key to capturing the complex phase behavior of these polymers is the assumption that both PEO and PPO monomer units exist in two states: a polar state that is well solvated by water and a nonpolar state that is poorly solvated.[31] These states are related to trans and gauche conformations of the bonds in the monomer units. With this assumption, binary[31] and ternary[9] phase diagrams of PEO, PPO, and water mixtures have been reproduced without the use of temperature and concentration dependent parameters. Modeling the polymer shell around our nanoparticles with this theory requires a three-component system comprised of five states: water, polar-EO, nonpolar-EO, polar-PO, and nonpolar-PO. The model space for these calculations consists of a hexagonal lattice with spherical geometry, composed of layers that increase in volume with increasing distance from the particle surface. Solvent or monomer segments (in one of the two states) must occupy every lattice site in the system. The lattice size is given by the size of an EO or PO monomer unit (4.0 Å). The spherical core (representing $Fe_3O_4$) is considered to be impenetrable to both polymer and solvent. Within each layer, an approximation of random mixing is made (a mean-field approximation), meaning all lattice sites within a layer are equivalent and the problem is essentially one-dimensional.

The goal of the lattice calculations is to compute the PEO, PPO, and water volume fraction profiles around the spherical core. These profiles are derived from the canonical partition function, $Q$, where

$$Q = \Omega \exp(-\beta A_{\text{int}}) \exp(-\beta U) \tag{3-17}$$

In this equation, $\beta = 1/kT$, $A_{int}$ is the total internal free energy of the system, $\Omega$ is the configurational degeneration, and $U$ is the configurational energy. The latter two parameters depend on the particular spatial configuration of the molecules in the lattice. The total internal free energy, $A_{int}$, of the system is given by

$$\beta A_{\text{int}} = \sum_i \sum_A n_{Ai} \sum_B P_{ABi} \left[ \beta U_{AB} + \ln(P_{ABi} / g_{AB}) \right] \qquad (3\text{-}18)$$

where the sums are taken over $i$ (the layers), $A$ (the three components), and $B$ (all states of component $A$). In Equation 3-18, $n_{Ai}$ is the number of sites in layer $i$ occupied by component $A$, $P_{ABi}$ is the fraction of component $A$ in layer $i$ that is in state $B$, $U_{AB}$ is the internal energy of component $A$ in state $B$, and $g_{AB}$ is the degeneration factor of state $B$ of component $A$ (i.e. the number of $B$-state conformations of component $A$).

The configurational energy, $U$, is found by adding all nearest neighbor interactions (including surface interactions) and is given by

$$\beta U = \frac{1}{2} \sum_{i=0}^{M} L_i \sum_A \sum_{A'} \sum_B \sum_{B'} \phi_{Ai} P_{ABi} \chi_{BB'} \left\langle P_{A'B'i} \phi_{A'i} \right\rangle \qquad (3\ 19)$$

where the sums are taken over layer $i$ and component $A$ in state $B$ with another component $A$' in state $B$'. In Equation 3-19, $\phi_{Ai}$ is the volume fraction of sites in layer $i$ that are occupied by component $A$ (the final goal of these lattice calculations), $M$ is the number of layers (60 in these simulations), $L_i$ is the number of lattice sites in layer $i$, and $\chi_{BB'}$ is the interaction energy between component $A$ in state $B$ and component $A$' in state $B$'. The brackets <...> represent an average over layers $i$ - 1, $i$, and $i$ + 1, including the surface layer ($i$ = 0). The $\chi_{BB'}$ parameter in Equation 3-19 is essentially a Flory-Huggins interaction parameter; however, unlike a standard Flory-Huggins parameter, it does not have to written as a function of temperature and concentration to accurately reproduce the phase behavior of polymers.[13] When considering the interaction with the surface, the parameter $\chi_{BS}$ is used instead to represent the interaction energy of component $A$ in state $B$ with the surface.

The lattice simulations involve calculating the equilibrium state distribution, $\{P_{ABi}\}$, and the equilibrium segment density distribution, $\{n_{Ai}\}$, where $n_{Ai} = \phi_{Ai} L_i$. These distributions are interdependent and cannot be calculated independently; however, the numerical procedure used in these calculations involves computing these quantities independently and then following an iterative procedure until the two equilibrium

distributions are self-consistent. The equilibrium state distribution is first calculated from the partition function (assuming a constant segment density distribution) as shown in Linse and Bjorling.[13] The equilibrium segment density distribution is then calculated from the partition function (holding the state distribution constant at its computed value).[13] This latter calculation is quite complex due to the added restrictions imposed by the connections between the monomer segments. Additionally, a constraint can be added for grafted chains that one end of each chain is forced to occupy the $i = 1$ layer. The equilibrium segment density distribution is then used to compute a new state distribution, with the process continuing iteratively until there is convergence of the distributions.

### 3.5.2 Parameters for Calculations

The lattice calculations are dependent on a large number of parameters that have been determined by extensive regression against PEO-water, PPO-water, and PEO-PPO-water phase diagrams over a range of temperatures.[9] A summary of the parameters used in evaluating Equations 3-18 and 3-19 is given in Table 3-4, which shows that the three-component, five-state system that comprises the polymer shell of our nanoparticles requires a total of 18 independent parameters. Four independent parameters are related to the internal free energy in Equation 3-18, namely the internal energy difference of the polar and nonpolar forms of the EO and PO monomer segments, as well as the polar:nonpolar degeneracy ratio of the segments. The EO unit has a much lower degeneracy ratio (1:8) than PO (1:60) because it has many more polar conformations that are compatible with the structure of water. The absolute internal energy of water, polar-EO, and polar-PO are defined as zero because they are chosen as reference states in pure form. Fourteen additional independent parameters are related to the configurational energy in Equation 3-19, of which ten are $\chi_{BB'}$ parameters that define the state-state interaction energies and five are $\chi_{BS}$ parameters that define the state-surface interaction energies (of which four are independent). These parameters have been shown to successfully predict the phase behavior of PEO-PPO block copolymers, including the critical micellization temperature and the micelle structure,[10,12,14] and so should be accurate for the polymer shells of our nanoparticles.

**Table 3-4.** Parameters used in lattice calculations

| Component (A) | State (B) | State No. | $U_{AB}$ (kJ/mol) | $g_{AB}$ |
|---|---|---|---|---|
| Water | - | 1 | 0 | 1 |
| EO | polar | 2 | 0 | 1 |
| EO | nonpolar | 3 | 5.086 | 8 |
| PO | polar | 4 | 0 | 1 |
| PO | nonpolar | 5 | 11.5 | 60 |

| $kT\chi_{BB'}$ or $kT\chi_{BS}$ (kJ/mol) | | | | | |
|---|---|---|---|---|---|
| **State No.** | 2 | 3 | 4 | 5 | S |
| 1 | 0.6508 | 5.568 | 1.7 | 8.5 | 4.0 |
| 2 | - | 1.266 | 1.8 | 3.0 | 2.0 |
| 3 | - | - | 0.5 | -2.0 | 2.0 |
| 4 | - | - | - | 1.4 | 0 |
| 5 | - | - | - | - | 0 |

In applying lattice theory to our magnetic nanoparticles, we made the simplifying assumption that the polymer shell is composed of PEO and PPO chains that are end-grafted to the magnetite core. We did not explicitly include PAA in the calculations because it is present in a relatively low amount and the geometry of the backbone would complicate the calculations. To account for the alkyl chain that forms the PAA backbone, the surface of the spherical core was considered to be hydrophobic. This assumption determined the five $\chi_{BS}$ parameters listed in Table 3-4 that define the interaction of the states with the surface. As these parameters are all relative to one another, $\chi_{BS}$ for PO segments (in both states) was fixed at zero meaning it had no interaction with the surface. The interaction between EO segments and water was slightly repulsive, as seen by the relative positive value of $\chi_{BS}$.

To calculate the grafting density of the polymer chains (an input to the lattice calculations), we used a bound-polymer:magnetite mass ratio of 0.8 and computed the

total surface area of polydisperse magnetite particles with $R_{c,med}$ = 37.5 Å and $\sigma_c$ = 0.32 (values from TEM, Section 2.3.3). With the known molecular weight and side chain ratios of our graft copolymers, we then calculated the grafting density of PEO and PPO side chains for each type of particle. The calculated grafting densities were: 16/0: 1.17 PEO chains/nm$^2$; 12/4: 0.943 PEO chains/nm$^2$ and 0.314 PPO chains/nm$^2$; 8/8: 0.682 PEO chains/nm$^2$ and 0.682 PPO chains/nm$^2$. We assumed that both the PEO and PPO chains were linear homopolymers of molecular weight 3000 and 2000 g/mol, respectively, which is equivalent to 68 repeat units for the PEO chains and 34 repeat units for the PPO chains. Lattice calculations were performed for each type of graft copolymer, assuming that all chains were grafted to a spherical core of radius 37.5 Å (the median magnetite core radius). The temperature was fixed at 300 K in the calculations.

### 3.5.3 Results of Lattice Calculations

Mean-field lattice calculations were performed by Per Linse (University of Lund, Sweden) for the three types of magnetic nanoparticles studied by small angle neutron scattering. The calculation results for the particles are shown in Figure 3-7, which shows the volume fraction profiles of water, EO segments (i.e. PEO), and PO segments (i.e. PPO) as a function of distance from the surface. The layer number has been transformed to distance by multiplying by the lattice size. In Figure 3-7a, the calculated PEO volume fraction profile for the 16/0 particles is approximately linear and decays to zero at approximately 70 Å from the surface. This extension of the PEO chains is consistent with having a relatively high grafting density that results in significant interactions between chains. The observed linear profile is affected slightly by our assumption of a hydrophobic surface, which repels water more than PEO. A repeat of the calculation assuming an athermal surface (no surface interactions) caused the PEO volume fraction to decrease slightly in the first two layers because it was no longer attracted to the surface relative to water (as it was for the hydrophobic surface). However, in the third and outer layers ($\geq$ 12 Å), the surface interaction parameters had no effect on the PEO profile.

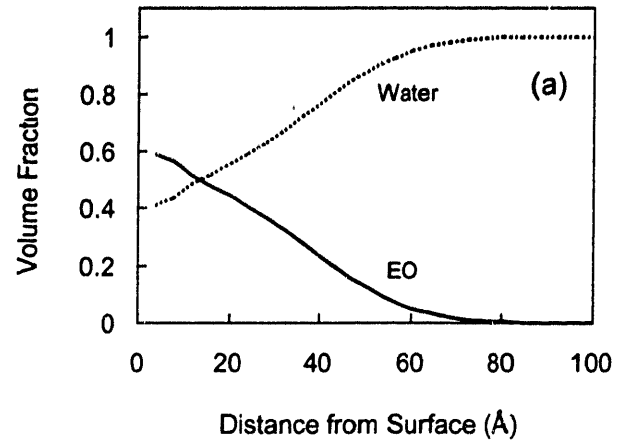


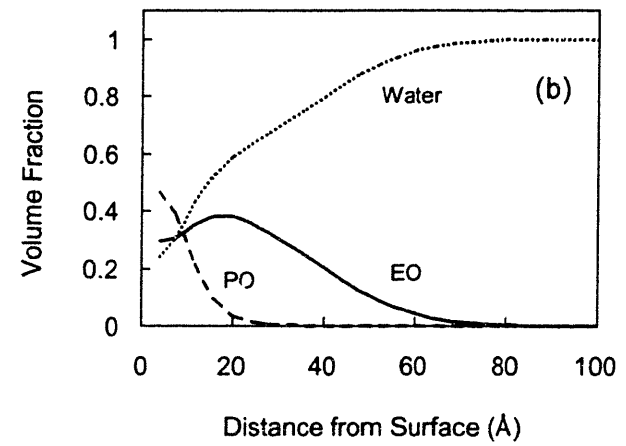


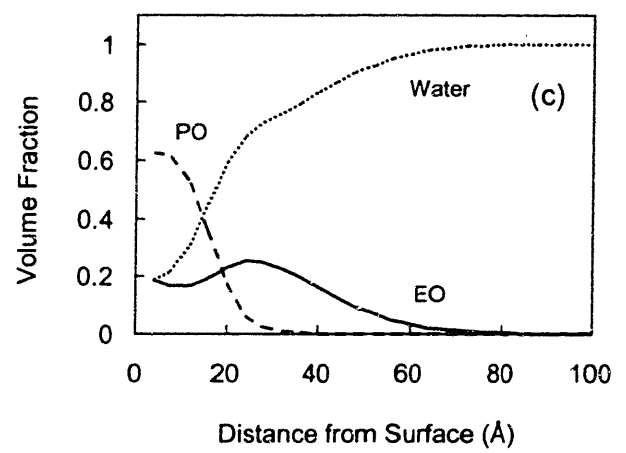


**Figure 3-7.** Results of lattice calculations for (a) 16/0, (b) 12/4, and (c) 8/8 magnetic fluids. The calculations were performed for end-grafted PEO and PPO chains with a grafting density of: 16/0: 1.17 PEO chains/nm$^2$; 12/4: 0.943 PEO chains/nm$^2$ and 0.314 PPO chains/nm$^2$; 8/8: 0.682 PEO chains/nm$^2$ and 0.682 PPO chains/nm$^2$ on a spherical core with $R_c$ = 37.5 Å.

The calculated PEO, PPO, and water volume fraction profiles for the 12/4 and 8/8 particles are illustrated in parts b and c of Figure 3-7. Comparison of the simulation results shows that water penetration into the polymer shell is hindered by replacement of PEO side chains with PPO side chains. The PPO side chains have exactly half the number of repeat units and are more hydrophobic and are therefore more concentrated than PEO in the first few layers of the 12/4 and 8/8 polymer shells. In Chapter 2, we postulated that adding both hydrophobic and hydrophilic side chains would form a polymer shell with two regions: an inner region for organic solubilization and an outer region for steric stabilization in water. Lattice calculations seem to support this model in that the 8/8 particles have a ~15 Å region around the particle core where the PPO volume fraction is greater than 0.40. In this region, water and hydrophilic EO segments are somewhat excluded. In particular, the PEO chains show a slight minimum at ~10 Å as they feel a repulsive interaction with the PPO chains; this minimum is observed regardless of our choice of surface interaction parameters. The PEO side chains are not fully able to segregate from this region, however, as they are tethered to the magnetite surface.

The structure of the polymer shell is qualitatively similar to that of a Pluronic micelle composed of PEO-PPO-PEO triblock copolymers, as shown in Figure 3-8. These polymer micelles have been shown experimentally and theoretically to consist of PPO-rich cores surrounded by a well solvated PEO corona. Neutron scattering studies have shown that PPO and PEO are highly segregated in the core and corona of these micelles,[5] but also that there is a significant amount of water in the PPO-rich core. The water volume fraction in the core depends on the particular copolymer and temperature but can range from 0.05 to 0.50.[4-6] Lattice calculations on these structures have shown similar results. Pluronic P104 ($EO_{30}$-$PO_{61}$-$EO_{30}$) showed a structure that is qualitatively similar to that of the 8/8 polymer shell shown in Figure 3-7c;[12] however, the EO volume fraction was only 0.05 in the first layer of the micelle, which is much lower than in the interior region of the nanoparticle shell (0.20). A similar result is seen for many other types of Pluronic micelles,[11,12] which is reasonable because the EO segments in micelles are not attached to a surface and can segregate more freely. The volume fraction of water in the

first layer of the polymer shell (0.20) is consistent with the values predicted within the first layer of Pluronic micelles (0.10-0.35).[11,12]

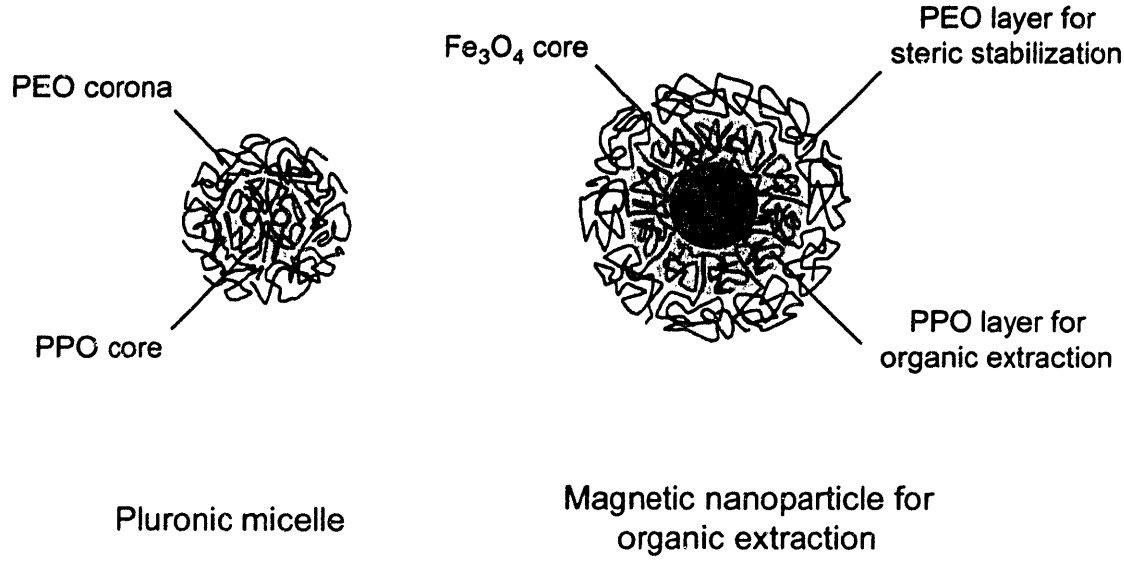


**Figure 3-8.** Structural comparison of Pluronic micelles with coated magnetite nanoparticles. The Pluronic micelles have a hydrophobic PPO core and a PEO corona.

### 3.5.4 Comparison with SANS Results

The lattice calculations can be compared with neutron scattering results by comparing the predicted water penetration profiles for particles with the median core radius. This comparison is made in Figure 3-9, which shows the best-fit results from SANS for both a linear solvent penetration profile (part b) and a constant solvent volume fraction in the shell (part c). Comparing the solvent penetration from lattice calculations (Figure 3-9a) with the SANS results assuming a linear solvent penetration model (Figure 3-9b) shows that the solvent penetration is essentially linear for the 16/0 nanoparticles. However, the water volume fraction at the magnetite surface from lattice calculations (0.40) is lower than the value from SANS (0.63). A similar result is seen for the 12/4 particles while the 8/8 particles have a nearly identical volume fraction of water at the magnetite surface. Figure 3-9a also shows that the water profile from lattice calculations is increasingly nonlinear as more PPO chains are added. This result may explain why the 8/8 SANS data were more difficult to fit than the 12/4 or 16/0 data.

Lattice calculations showed no significant difference in the predicted thickness of the polymer shell between particles, which is consistent with our observations from dynamic light scattering (Section 2.3.5). The total thickness of the shell is difficult to estimate from lattice calculations, as the polymer concentration decays very slowly between 60-80 Å. This observation may help to explain why SANS underpredicts the shell thickness. For example, SANS predicts a shell thickness of 62 Å for the 16/0 particles assuming linear solvent penetration. At this distance, our lattice calculations predict that the shell is ~96% water. The large hydrodynamic shell thickness from dynamic light scattering (94 Å) may be a consequence of the slow decay of polymer concentration, whereas the SANS model imposes a sharper cutoff at the edge of the shell.

More complex models for solvent penetration in the SANS data fitting were not helpful in further understanding the structure. While the 8/8 solvent profile in Figure 3-9a suggests that the shell could be modeled as two continuous linear regions, refitting the SANS data with this model did not improve the fit, as the optimal values of the parameters suggested an inner shell with the same linear profile in Figure 3-9b and an outer shell of zero thickness. While more complex functional forms such as an exponential decay function[6] or Fermi-Dirac distribution function[26] have been applied to model solvent penetration, these have no analytical form for the scattering and have typically been applied to micellar systems that were much more monodisperse. The linear solvent penetration model used in this study seems to adequately capture the structural changes in the particles that occur when adding PPO side chains, as the general trends in structure are consistent with the lattice calculations. It is noted that neither the SANS experiments nor the lattice calculations are capable of predicting inhomogeneity in the shell in an angular direction, as the SANS models were centrosymmetric and the lattice calculations assumed random mixing within a layer.

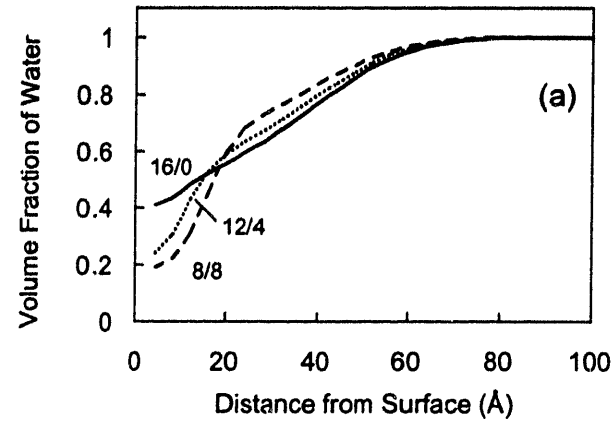


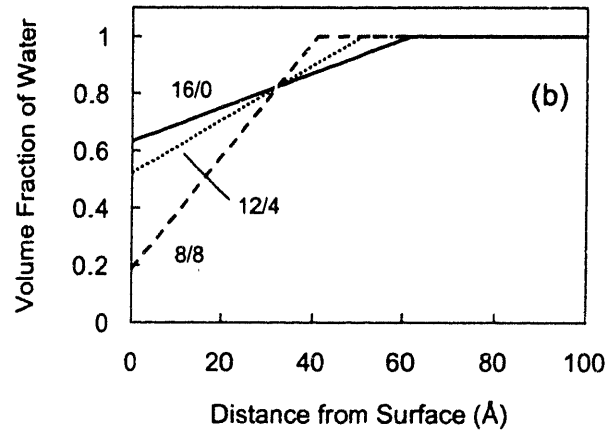


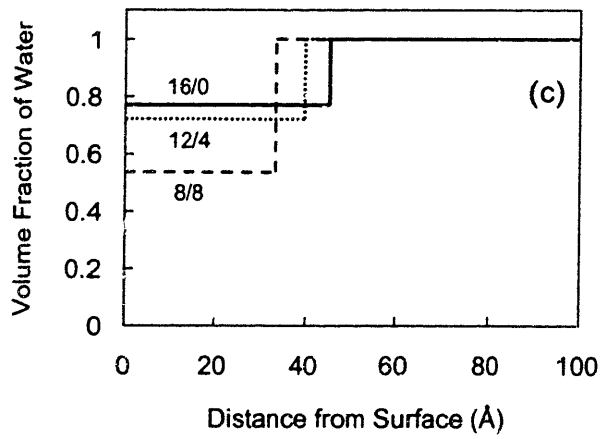


**Figure 3-9.** Comparison of water volume fraction profile in polymer shell from (a) lattice calculations, (b) neutron scattering data assuming a linear solvent profile, and (c) neutron scattering data assuming a constant solvent volume fraction in the shell.

## 3.6 Summary

In this work we have examined the hydration structure within the polymer shell of our magnetic nanoparticles experimentally with small angle neutron scattering and theoretically with mean-field lattice calculations. The hydration structure is important because we have designed the polymer shell around our magnetic nanoparticles to provide an inner hydrophobic region for the extraction of organic compounds and an outer hydrophilic region to provide steric stabilization in water. Both SANS and the lattice calculations provided evidence that this structure exists when PPO side chains are present in the stabilizing graft copolymer.

We conducted SANS experiments on our nanoparticles in a range of solvents with different ratios of $H_2O$ to $D_2O$ to study different aspects of the nanoparticle structure. When the particles were suspended in $H_2O$-rich solvents, the scattering was primarily from the magnetite core, while the scattering was primarily from the shell in $D_2O$-rich solvents. In a solvent selected to contrast-match the polymer, we found that the scattering was very similar for all of the particles, suggesting little difference in core size. From these data, we calculated the size of the $Fe_3O_4$ core, which we were able to compare with values from electron microscopy. We observed a significant difference in the core size, which we attributed to the irregular shape of the magnetic core. The shell hydration and interparticle interaction parameters were determined via a global fit of the scattering data for each type of particle in the five aqueous solvents with a varying level of deuteration, allowing us to vary the contrast without affecting the particle structure. We successfully fit the scattering data with a core-shell model for the particles with both a constant and a linear solvent profile in the shell. With both models, we observed a significant trend in the shell hydration, in that replacing PEO side chains with PPO side chains led to a contraction of the polymer shell and exclusion of water near the magnetite surface. In addition, adding PPO side chains led to a slight attraction between particles that we observed in the interparticle structure factor.

Self-consistent mean-field lattice calculations of end-grafted polymer chains, performed by Per Linse (University of Lund, Sweden), provided another method of

determining the structure in the polymer shell. This technique was able to predict both the water penetration profile and the distribution of PEO and PPO chains in the shell. This latter information could not be determined with neutron scattering without deuterating either the PEO or PPO chains due to their similar scattering length density. The lattice calculations showed that the shorter, more hydrophobic PPO chains were concentrated near the magnetite surface while PEO chains extended away from the surface. There was some evidence of PEO exclusion from the PPO-rich region, although less than is typically observed in simulations of structurally similar Pluronic micelles. This difference can be ascribed to the chemical attachment of the PEO chains to the surface of our magnetite nanoparticles. The hydration profiles from the lattice calculations were qualitatively similar to those determined by neutron scattering, in that the replacement of PEO side chains with PPO chains led to the formation of a water-excluded zone near the particle surface. The hydration levels are similar to those seen in the cores of Pluronic micelles, which are known to solubilize significant amounts of hydrophobic organics in water, suggesting our nanoparticles may have a similar high affinity for target organic solutes.

## 3.7 Bibliography

(1) Feigin, L. A.; Svergun, D. I. *Structural Analysis by Small-Angle X-Ray and Neutron Scattering*; Plenum Press: New York, 1987.

(2) Shen, L. F.; Stachowiak, A.; Fateen, S. E. K.; Laibinis, P. E.; Hatton, T. A. Structure of Alkanoic Acid Stabilized Magnetic Fluids. A small-Angle Neutron and Light Scattering Analysis. *Langmuir* **2001**, *17*, 288-299.

(3) Cebula, D. J.; Charles, S. W.; Popplewell, J. The Structure of Magnetic Particles Studied by Small-Angle Neutron-Scattering. *Colloid Polym. Sci.* **1981**, *259*, 395-397.

(4) Goldmints, I.; vonGottberg, F. K.; Smith, K. A.; Hatton, T. A. Small-Angle Neutron Scattering Study of PEO-PPO-PEO Micelle Structure in the Unimer-to-Micelle Transition Region. *Langmuir* **1997**, *13*, 3659-3664.

(5) Goldmints, I.; Yu, G. E.; Booth, C.; Smith, K. A.; Hatton, T. A. Structure of (Deuterated PEO)-(PPO)-(Deuterated PEO) Block Copolymer Micelles as Determined by Small-Angle Neutron Scattering. *Langmuir* **1999**, *15*, 1651-1656.

(6) Liu, Y. C.; Chen, S. H.; Huang, J. S. Small-Angle Neutron Scattering Analysis of the Structure and Interaction of Triblock Copolymer Micelles in Aqueous Solution. *Macromolecules* **1998**, *31*, 2236-2244.

(7) Scheutjens, J.; Fleer, G. J. Statistical-Theory of the Adsorption of Interacting Chain Molecules. 1. Partition-Function, Segment Density Distribution, and Adsorption-Isotherms. *J. Phys. Chem.* **1979**, *83*, 1619-1635.

(8) Bjorling, M.; Linse, P.; Karlstrom, G. Distribution of Segments for Terminally Attached Poly(Ethylene Oxide) Chains. *J. Phys. Chem.* **1990**, *94*, 471-481.

(9) Malmsten, M.; Linse, P.; Zhang, K. W. Phase-Behavior of Aqueous Poly(Ethylene Oxide) Poly(Propylene Oxide) Solutions. *Macromolecules* **1993**, *26*, 2905-2910.

(10) Linse, P. Phase-Behavior of Poly(Ethylene Oxide)-Poly(Propylene Oxide) Block-Copolymers in Aqueous-Solution. *J. Phys. Chem.* **1993**, *97*, 13896-13902.

(11) Linse, P. Micellization of Poly(Ethylene Oxide)-Poly(Propylene Oxide) Block-Copolymers in Aqueous-Solution. *Macromolecules* **1993**, *26*, 4437-4449.

(12) Hurter, P. N.; Scheutjens, J.; Hatton, T. A. Molecular Modeling of Micelle Formation and Solubilization in Block-Copolymer Micelles. 2. Lattice Theory for Monomers with Internal Degrees of Freedom. *Macromolecules* **1993**, *26*, 5030-5040.

(13) Linse, P.; Bjorling, M. Lattice Theory for Multicomponent Mixtures of Copolymers with Internal Degrees of Freedom in Heterogeneous Systems. *Macromolecules* **1991**, *24*, 6700-6711.

(14) Linse, P.; Hatton, T. A. Mean-Field Lattice Calculations of Ethylene Oxide and Propylene Oxide Containing Homopolymers and Triblock Copolymers at the Air/Water Interface. *Langmuir* **1997**, *13*, 4066-4078.

(15) Baskir, J. N.; Hatton, T. A.; Suter, U. W. Thermodynamics of the Separation of Biomaterials in 2-Phase Aqueous Polymer Systems - Effect of the Phase-Forming Polymers. *Macromolecules* **1987**, *20*, 1300-1311.

(16) Yoe, J. H.; Jones, L. Colorimetric Determination of Iron with Disodium-1,2-dihydroxybenzene-3,5-disulfonate. *Ind. Eng. Chem.* **1944**, *16*, 111-115.

(17) Hayter, J. B. Determination of Structures in Ferrofluids by Small-Angle Neutron-Scattering. *J. Chem. Soc., Faraday Trans.* **1991**, *87*, 403-410.

(18) Lembke, U.; Hoell, A.; Kranold, R.; Muller, R.; Schuppel, W.; Goerigk, G.; Gilles, R.; Wiedenmann, A. Formation of Magnetic Nanocrystals in a Glass Ceramic Studied by Small-Angle Scattering. *J. Appl. Phys.* **1999**, *85*, 2279-2286.

(19) Eastoe, J.; Hetherington, K. J.; Sharpe, D.; Dong, J. F.; Heenan, R. K.; Steytler, D. Mixing of Alkanes with Surfactant Monolayers in Microemulsions. *Langmuir* **1996**, *12*, 3876-3880.

(20) Farinha, J. P. S.; d'Oliveira, J. M. R.; Martinho, J. M. G.; Xu, R. L.; Winnik, M. A. Structure in Tethered Chains: Polymeric Micelles and Chains Anchored on Polystyrene Latex Spheres. *Langmuir* **1998**, *14*, 2291-2296.

(21) Lin, E. K.; Gast, A. P. Self Consistent Field Calculations of Interactions between Chains Tethered to Spherical Interfaces. *Macromolecules* **1996**, *29*, 390-397.

(22) Rosensweig, R. E. *Ferrohydrodynamics*; Dover Publications. Inc.: Mineola, NY, 1985.

(23) Kotlarchyk, M.; Chen, S. H.; Huang, J. S. Critical-Behavior of a Microemulsion Studied by Small-Angle Neutron-Scattering. *Phys. Rev. A* **1983**, *28*, 508-511.

(24) Schubel, D.; Bedford, O. D.; Ilgenfritz, G.; Eastoe, J.; Heenan, R. K. Oligo- and Polyethylene Glycols in Water-in-Oil Microemulsions. A SANS study. *PCCP* **1999**, *1*, 2521-2525.

(25) Press, W. H.; Teukolsky, S. A.; Flannery, B. P.; Vetterling, W. T. *Numerical Recipes: The Art of Scientific Computing*; Cambridge University Press: Cambridge, 1989.

(26) Won, Y. Y.; Davis, H. T.; Bates, F. S.; Agamalian, M.; Wignall, G. D. Segment Distribution of the Micellar Brushes of Poly(Ethylene Oxide) via Small-Angle Neutron Scattering. *J. Phys. Chem. B* **2000**, *104*, 7134-7143.

(27) Pedersen, J. S.; Svaneborg, C. Scattering from Block Copolymer Micelles. *Curr. Opin. Colloid Interface Sci.* **2002**, *7*, 158-166.

(28) Poppe, A.; Willner, L.; Allgaier, J.; Stellbrink, J.; Richter, D. Structural Investigation of Micelles Formed by an Amphiphilic PEP-PEO Block Copolymer in Water. *Macromolecules* **1997**, *30*, 7462-7471.

(29) Forster, S.; Burger, C. Scattering Functions of Polymeric Core-Shell Structures and Excluded Volume Chains. *Macromolecules* **1998**, *31*, 879-891.

(30) Hurter, P. N.; Scheutjens, J.; Hatton, T. A. Molecular Modeling of Micelle Formation and Solubilization in Block-Copolymer Micelles. 1. A Self-Consistent Mean-Field Lattice Theory. *Macromolecules* **1993**, *26*, 5592-5601.

(31) Karlstrom, G. A New Model for Upper and Lower Critical Solution Temperatures in Poly(Ethylene Oxide) Solutions. *J. Phys. Chem.* **1985**, *89*, 4962-4964.

# Chapter 4

# Organic Solubilization

## 4.1 Introduction

The tailored magnetic fluids for organic extraction have been shown to consist of particles that are nanoscale in size, suitably magnetic, and colloidally stable over a range of conditions (Chapter 2). In addition, the structure within the bifunctional polymer shell has been probed with neutron scattering and compared to lattice calculation results (Chapter 3), which suggested that the polymer shell contains a hydrophobic domain for organic solubilization. In this chapter, we examine the affinity of the particles for several types of common organic compounds, such as substituted benzenes, polyaromatic hydrocarbons (PAH's), and alkanes. These species represent common synthetic organic compounds that could be present in either plant wastewater or drinking water, and must be removed before the water could be discharged or consumed. As these organics are soluble in water at low concentration, standard coagulation and sedimentation techniques are not effective for their removal. Magnetic fluids represent a new class of extractants that should possess significant advantages over traditional methods of organic extraction due to their extremely large surface area that is achieved without the use of porous materials, such as activated carbon, that have inherent mass transfer limitations.[1]

We measured the organic affinity of our particles by saturating the magnetic fluids with an organic species and measuring the total organic solubility in the magnetic fluid phase. This approach is similar to techniques that have been used to measure organic solubilities in PEO-PPO-PEO triblock copolymer (Pluronic) micelles that contain a similar structure (Figure 3-8).[2-5] By saturating the system, we avoid problems with organic adsorption on the walls of containers or transfer devices.[3] The measurement of organic uptake at levels below saturation can be achieved with fluorescent organic molecules, such as pyrene, where the phase partitioning can be tracked with the fluorescence emission of the organic.[6] Comparing the solubility of organics in our

nanoparticles with that in Pluronic micelles will give an indication of whether similar hydrophobic domains exist in the polymer shell.

## 4.2 Experimental

### 4.2.1 Materials

Polyacrylic acid (50 wt% in water, $M_w$ = 5000), iron(III) chloride hexahydrate (97%), iron(II) chloride tetrahydrate (99%), ammonium hydroxide (28 wt% in water), hydrochloric acid (37 wt% in water), Tiron (4,5-dihydroxy-1,3-benzene-disulfonic acid, disodium salt monohydrate), octane, naphthalene, *o*-dichlorobenzene, phenanthrene, and pyrene were obtained from Sigma-Aldrich (Milwaukee, WI). HPLC grade hexane and toluene were obtained from Burdick and Jackson (Muskegon, MI). Jeffamine XTJ-234 ($CH_3$-O-PEO/PPO-$NH_2$, EO:PO = 6.1:1, $M_w$ = 3000) and Jeffamine XTJ-507 ($CH_3$-O-PEO/PPO-$NH_2$, EO:PO = 1:6.5, $M_w$ = 2000) were obtained as gifts from Huntsman Corporation (Houston, TX). In this work, we consider XTJ-234 to be equivalent to pure PEO and XTJ-507 to be equivalent to pure PPO, and we refer to these polymers as PEO-$NH_2$ and PPO-$NH_2$, respectively.

### 4.2.2 Preparation of Magnetic Fluids

The 16/0, 12/4, and 8/8 magnetic fluids for the SANS experiments were prepared as described in Sections 2.2.2 and 2.2.3. The nomenclature *x*/*y* refers to a magnetic fluid produced with a graft copolymer in which *x*% of the carboxylic acid groups in the polyacrylic acid (PAA) backbone were reacted with polyethylene oxide (PEO) chains and *y*% with polypropylene oxide (PPO) chains. To prepare the suspensions for the organic solubilization experiments, the magnetic fluids were washed magnetically in a bench-scale high gradient magnetic separation column. (Model L-1CN Frantz Canister Separator, S.G. Frantz Co., Inc., Trenton, NJ). The HGMS system consisted of a cylindrical glass column with an internal radius of 0.285 cm and a length of 22.6 cm (a volume of 5.77 $cm^3$) that was packed with 6.2 g of type 430 fine-grade stainless steel wool (40-66 μm diameter) also supplied by S.G. Frantz Co., Inc. The packing occupied 0.79 $cm^3$, resulting in a packing fraction of 14%, which is the maximum packing fraction

that could be obtained by hand. For filtration, the column was placed in the 1 cm gap between the two metal plates of the filter. During magnetic filtration, a 1.3 T magnetic field was generated between the two plates with an attached electromagnet. The direction of the magnetic field was transverse to the direction of flow through the column. Magnetic washing of the particles was performed by passing 4.5 mL of magnetic fluid with 1.25 wt% $Fe_3O_4$ through the column with the electromagnet on. The liquid was pumped at 1.6 mL/min with a peristaltic pump. With the magnet on, the majority of particles were trapped in the filter, while the filtrates contained some particles along with free polymer and ions from the synthesis. The magnet was then turned off and 4.5 mL of water was passed through the column to collect and resuspend the washed particles. This process of passing and collecting was then repeated three additional times to fully remove free polymer and ions. Before each pass of the particles, the column was backflushed with clean water and acetone, and dried with a heat gun to remove any liquid left in the column. The magnetite concentration in the washed magnetic fluid was measured with chemical iron titration.[7]

### 4.2.3 Solubility Measurements at Saturation

Aqueous magnetic fluids of varying particle concentration were saturated with a target organic by mixing them with the pure organic species until equilibrium was reached. The mixing procedure depended slightly on the nature of the solute, but in general, 10 mL of the organic (if liquid) or 0.75 g (if solid) were mixed with 7 mL of aqueous magnetic fluid and continually agitated for 48 h. Afterwards, the magnetic fluid was drawn off for analysis. If the organic was solid, the aqueous magnetic fluid was filtered with a 0.22 μm organic-saturated syringe filter (Millipore) to obtain the magnetic fluid for analysis. The organic content in the saturated magnetic fluid was measured by back-extraction into hexane. Three 1 mL portions of the magnetic fluid were added to test tubes, followed by 10 mL of hexane. The mixture was agitated for 24 h to allow the organic to partition into the hexane phase, which was analyzed with a Hewlett-Packard 5890A gas chromatograph to determine the concentration of the target organic and allow calculation of the original saturation concentration in the magnetic fluid. To measure the

solubility of hexane in the magnetic fluid, octane was used as the back-extraction solvent for analysis.

### 4.2.4 Fluorescence Experiments

To measure the solubility of pyrene in the magnetic fluids, the washed magnetic fluids were diluted to 0.005 wt% $Fe_3O_4$ with water. 25 μL of a $1.0 \times 10^{-4}$ M pyrene in methanol solution was then added to 5 mL of each magnetic fluid. After letting the samples equilibrate in the dark for 12 h, the solutions were transferred to a quartz cell with a 1 cm pathlength. The fluorescence emission spectrum was then measured by exciting the solutions with monochromatic light at 335 nm in a Photon Technology International QM-2000 7SE fluorescence spectrometer. The excitation source in this instrument was a mercury lamp.

## 4.3 Solubilization Results

### 4.3.1 Saturation Experiments

We conducted a series of extraction experiments to investigate the ability of the particles to absorb various organic compounds. In these experiments, aqueous suspensions of the magnetic particles were contacted with an organic until both the bulk water and the polymer layer around the particle were saturated with the organic. By varying the concentration of the particles in the suspension, we were able to calculate the solubility of the organic in the polymer layer and the polymer-water partition coefficient, giving an estimate of the ability of the particles to remove that species from a contaminated water source.

Aromatic species have a high affinity for PPO,[2-5,8] and provide a good indicator of the extraction potential of the particles. In Figure 4-1a, the total solubility of toluene in the magnetic fluid phase is presented for the 16/0, 12/4, and 8/8 particles as a function of the $Fe_3O_4$ particle concentration. Figure 4-1a shows that the concentration of toluene in the aqueous magnetic fluid phase increased significantly for the PPO-containing 12/4 and 8/8 particles. In contrast, the addition of 16/0 particles that contained only PEO in their

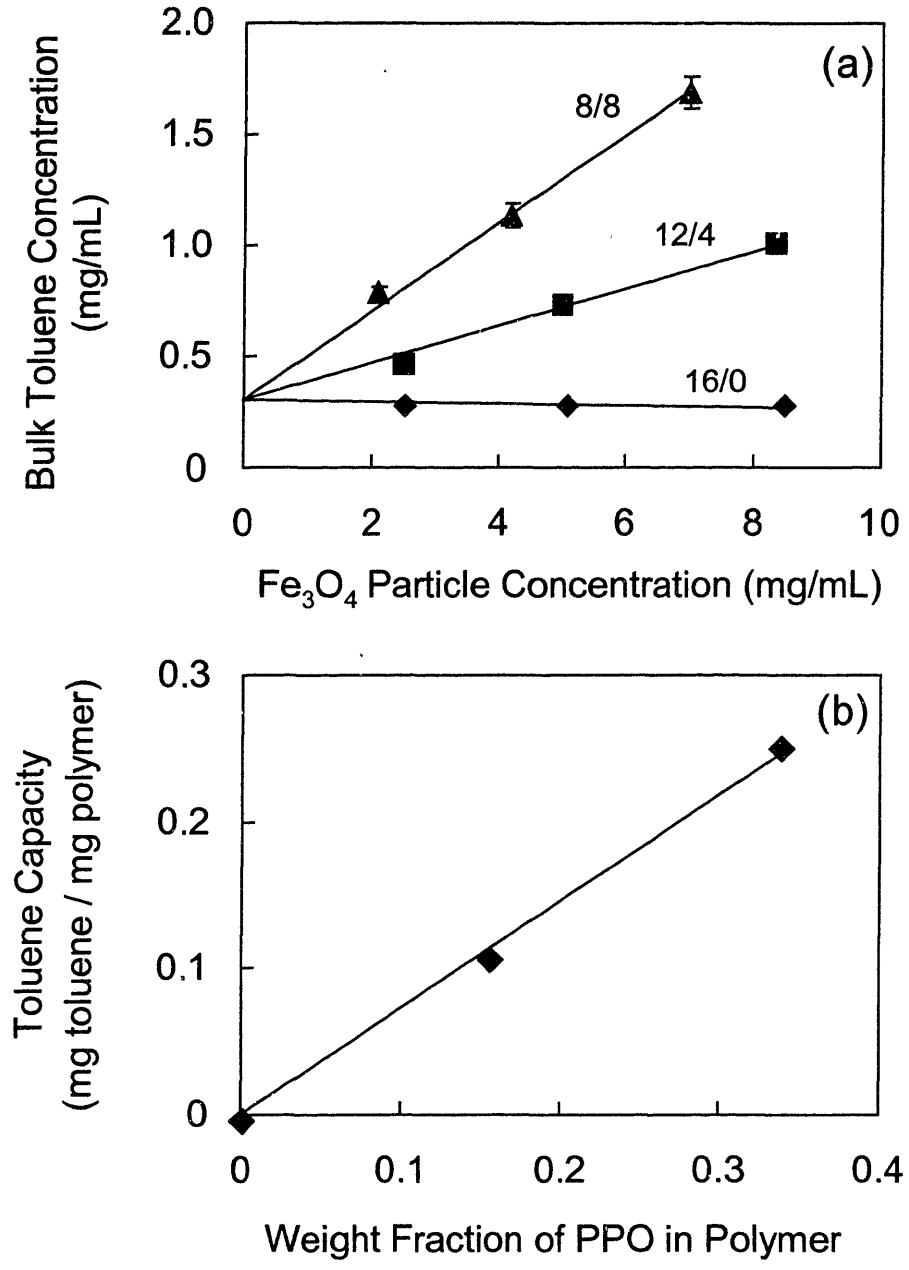


**Figure 4-1.** Toluene solubility in various aqueous magnetic fluids. (a) The toluene solubility increases with particle concentration for magnetic fluids that contain PPO side chains. (b) The solubility in the polymer shell is linear with the weight fraction of PPO in the polymer, suggesting that PPO is responsible for organic solubilization.

stabilizing layer caused no further uptake of toluene. This result suggests that only PPO is responsible for the increased solubility, and that the 12/4 and 8/8 particles may contain hydrophobic regions responsible for increased solubilization.

In Figure 4-1a, the intercept represents the saturation concentration of toluene in the bulk water. The common intercept for toluene was 0.30 mg/mL (300 ppm), which is lower than the published saturation concentration of 0.52 mg/mL.[9] This reproducible difference was possibly due to the loss of some toluene during our back-extraction into hexane and could not be eliminated by increasing the contacting time of the extractions. As the losses are relatively constant, they should not greatly affect the slopes of the lines in Figure 4-1a, which represent the toluene solubility in the particles per mass of magnetite. Using the bound-polymer:magnetite mass ratio of 0.8, as determined in Section 2.3.2, we calculated the toluene solubility in the polymer layer from the slope for each of the three magnetic fluids and compared them against the PPO content of the polymer shell (Figure 4-1b). The solubility in the polymer shell varied linearly with PPO content, giving further evidence that PPO was responsible for solubilization of the toluene. These results are promising because of the high loadings of toluene obtained at relatively low particle volume fractions. In particular, the 8/8 polymer shell contained loadings as high as 0.25 g toluene/g polymer, or 0.74 g toluene/g PPO.

We performed additional extractions of other organics using the 8/8 particles because it was our most hydrophobic system. Table 4-1 summarizes the results of these experiments and shows the high affinity of the 8/8 particles for a variety of organics. In this table, we calculated the molar solubility in the polymer layer using a density of 1 g/cm$^3$ for PEO and PPO. The table also gives the literature value of the saturation concentration of each solute in water,[9] showing the strong affinity of the organics for the polymer shell as compared to water. We calculated PPO-water partition coefficients ($K_{pw}$') by dividing the measured saturation concentration in the polymer shell by the aqueous solubility, and normalizing for the weight fraction of PPO in the polymer (0.34 for the 8/8 particles). The $K_{pw}$' values in Table 4-1 apply only at saturation and may vary somewhat with the concentration of the organic species in water, which is often much

lower than its saturation concentration. However, the $K_{pw}$' values at saturation are a good indicator of the magnitude of the partition coefficients at other concentrations.

**Table 4-1.** Organic solubility in 8/8 magnetic fluids and in water

| Compound | Solubility in 8/8 Polymer Shell (mol/L) | Solubility in Water [a] (mol/L) | $K_{pw}$' [b] | $K_{ow}$ [a] |
|---|---|---|---|---|
| Toluene | 2.72 | $5.59 \times 10^{-3}$ | 1430 | 490 |
| *o*-Dichlorobenzene | 1.75 | $9.77 \times 10^{-4}$ | 5280 | 2400 |
| Naphthalene | 0.141 | $2.45 \times 10^{-4}$ | 1700 | 2290 |
| Phenanthrene | 0.0677 | $6.31 \times 10^{-6}$ | 31600 | 37200 |
| Hexane | 0.398 | $1.48 \times 10^{-4}$ | 7930 | 12900 |

a) Data from ref. [9].
b) $K_{pw}$' is defined as the ratio of the saturation concentration in the PPO shell to the saturation concentration in the aqueous dispersion medium. The volume fraction of PPO in the polymer is 0.34.

## 4.3.2 Linear Free Energy Relationship

A comparison of the $K_{pw}$' values of the different solutes in Table 4-1 is challenging due to significant differences between the various solutes. These organics include substituted benzenes, PAH's, and linear alkanes, and any comparisons must take into account the differences in molecular size and polarity of these species. One measure of these effects is provided by the octanol-water partition coefficient ($K_{ow}$) scale; values of these coefficients for the solutes investigated here are tabulated in Table 4-1 for direct comparison with our results.[9] Clearly, the PPO-water partition coefficients correlate with this scale, which could therefore provide a basis for extrapolation and prediction of partition coefficients for other solutes of interest. This correlational approach does not provide a direct evaluation of thermodynamic parameters, however. A more direct thermodynamic analysis, based on a linear free energy relationship discussed in Schwarzenbach et al.,[9] could provide direct calculation of the activity coefficients of the organics in the PPO domains, which give an indication of the driving force for partitioning into the nanoparticles. This parameter also allows comparisons of different

classes of solutes and comparison to solubilization results obtained using structurally similar Pluronic micelles.

To derive a linear free energy relationship for organic partitioning in our nanoparticles, we considered the PPO domains around the particles to be a pure phase of PPO monomer units. Although in Chapter 3 we showed that the inner region of the polymer shell is not pure PPO, the volume fraction of PPO in the interior of the 8/8 shell is as high as 0.60. In addition, considering the solubilization to occur in a pure PPO domain makes it easier to compare our extraction results with other PPO-containing systems that have different overall compositions. This PPO phase was treated in terms of monomer units, as activity coefficients are usually defined by mole fraction weighting, which is not appropriate for polymers. At equilibrium, the mole fractions of the saturated organic in PPO monomer ($x_{ppo}^{sat}$) and water ($x_w^{sat}$) are related by

$$\gamma_{ppo}^{sat} x_{ppo}^{sat} = \gamma_w^{sat} x_w^{sat} \tag{4-1}$$

where $\gamma_{ppo}^{sat}$ and $\gamma_w^{sat}$ are the activity coefficients of the organic in the PPO and water phases, respectively, at saturation. Conversion of the mole fractions to molar concentrations at saturation ($C_i^{sat}$) yields:

$$K'_{pw} = \frac{C_{ppo}^{sat}}{C_w^{sat}} = \frac{\gamma_w^{sat} V_w}{\gamma_{ppo}^{sat} V_{ppo}} \tag{4-2}$$

where $V_w$ and $V_{ppo}$ are the molar volumes of water and a PPO monomer unit, respectively. According to Schwarzenbach et al.,[9]

$$\gamma_w^{sat} V_w = \frac{1}{C_w^{sat}(1, L)} \tag{4-3}$$

where $C_w^{sat}(1, L)$ is defined as the molar saturation concentration of the *liquid* organic compound in water at 1 atm. Equation 4-3 is a result of the reference state of the organic

compound, which we took to be the pure organic in liquid form at 1 atm.[9] Substitution of this relation into Equation 4-2 yields the linear free energy relationship:

$$\log K'_{pw} = -\log C_w^{sat}(1,L) - \log \gamma_{ppo}^{sat} - \log V_{ppo} \qquad (4\text{-}4)$$

For organics such as toluene that are liquid at atmospheric pressure and room temperature, $C_w^{sat}(1,L)$ is equal to the standard aqueous solubility listed in Table 4-1. For organics that are solids at ambient conditions (such as naphthalene), $C_w^{sat}(1,L)$ is equal to the subcooled liquid solubility, which can be calculated from the standard aqueous solubility, $C_w^{sat}$, and the vapor pressures of the pure solid, $p_s$, and subcooled liquid, $p_l$, forms as[9]

$$C_w^{sat}(1,L) = C_w^{sat}\frac{p_l}{p_s} \qquad (4\text{-}5)$$

With the linear free energy relationship in Equation 4-4, the activity coefficient of an organic solute in PPO can be obtained from $K_{pw}$' and $C_w^{sat}(1,L)$ data. In addition, a class of organics with the same activity coefficient in the PPO phase should fall on a line with slope of –1 on a linear free energy plot.

The linear free energy relationship for our nanoparticles is shown in Figure 4-2 as a logarithmic plot of $K_{pw}$' against $C_w^{sat}(1,L)$. Our data are presented for the five organic solutes in the 8/8 polymer shell, as well as data for various organic solutes in Pluronic micelles. We make the comparison with Pluronic micelles as their structure is similar to that of the nanoparticles, as shown in Figure 3-8. Figure 4-2 shows that organics follow the same solubility trends in the 8/8 polymer shell as in the micelles, as solubility data in both systems fall approximately on the same line for a given class of organics. Conceptually, this result means that a given class of solutes has roughly the same PPO activity coefficient (at saturation) in both systems. The slopes of the best-fit lines for a given class of solutes are close to –0.8, which is common for linear free energy relationships.[9] Lines of constant PPO activity coefficient (with a slope of –1) are included in Figure 4-2 for comparison. Substituted benzenes (i.e., toluene and

*o*-dichlorobenzene) exhibited the lowest PPO activity coefficients and therefore have the most favorable interaction with PPO. This result is expected since substituted benzenes are relatively small molecules and have a similar polarity to PPO, as illustrated by the similar Hildebrand solubility parameters for PPO (9.3 $cal^{1/2}/cm^{3/2}$) and toluene (8.9 $cal^{1/2}/cm^{3/2}$).[10] PAH's and linear alkanes have higher activity coefficients than substituted benzenes, as evidenced by their lower intercepts in Figure 4-2. The linear alkanes have the least favorable interaction with PPO, as the alkanes are much more nonpolar with Hildebrand solubility parameters of ~7.5 $cal^{1/2}/cm^{3/2}$.

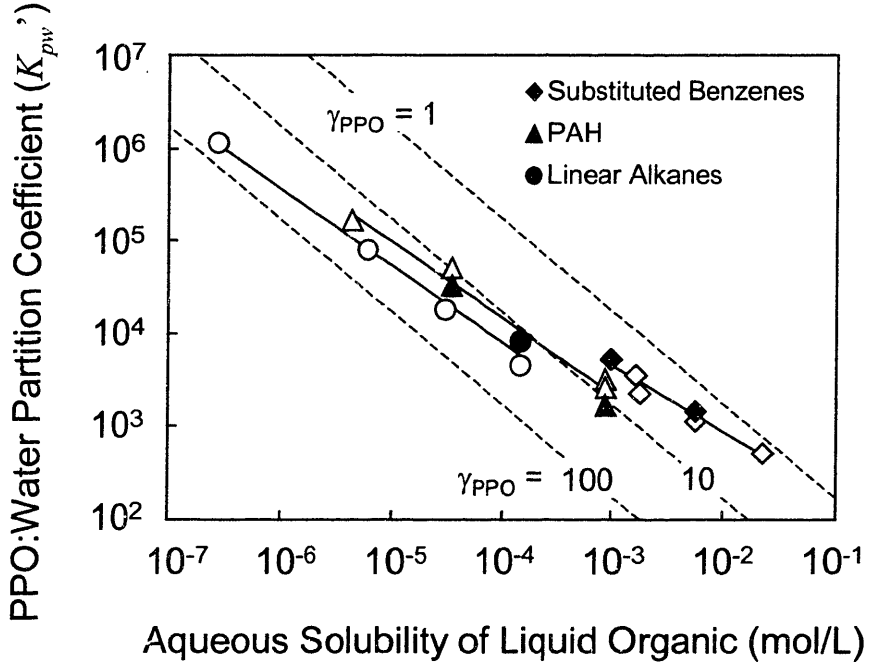


**Figure 4-2.** Linear free energy relationship of PPO-water partition coefficients. The PPO-water partition coefficient ($K_{pw}$') of various organics is plotted against their solubility as liquids in water. $K_{pw}$' data are presented for organics in the 8/8 particles (filled symbols) and a range of Pluronic micelles (open symbols).[2-4] Data for a given class of organics fall on approximately the same line, suggesting that the nanoparticles contain a PPO domain that is similar to the core of a Pluronic micelle.

The similar activity coefficients for the organics in the 8/8 particles and the Pluronic micelles suggest that our nanoparticles contain PPO domains that are similar to

the hydrophobic cores of Pluronic micelles. The small differences in organic solubility between the two systems may be due to differences in the size or shape of the hydrophobic domains, as experimental results have shown that $K_{pw}$' of PAH's in micelles can depend on the PPO core size.[3,4,11] The data suggest formation of PPO domains rather than isolated segments of PPO around our nanoparticle cores. For example, our $K_{pw}$' value for naphthalene is slightly lower for the 8/8 particles than for Pluronic micelles (Figure 4-2), but is an order of magnitude larger than the $K_{pw}$' value of 158 obtained for Pluronic copolymers that do not form micelles and therefore contain no distinct PPO domains.[4]

### 4.3.3 Fluorescence Measurements of Solubility

The solubilization of fluorescent organic molecules can be measured at very low levels due to the strong fluorescence emission from these molecules. With this technique, we can measure the partition coefficient of organics in a magnetic fluid at concentrations that are closer to what would be expected in a contaminated water supply, rather than the saturation levels that we have measured previously. Previous studies on pyrene, a PAH that is excited by UV radiation and fluoresces in the visible spectrum, have indicated that it is well solubilized by PPO-containing Pluronic micelles.[3,6] Pyrene is often used as a fluorescent probe for hydrophobic domains as it is known to change its fluorescence emission spectrum when it is solubilized in domains of different polarities. Specifically, the $I_1/I_3$ ratio (the intensity ratio of the first and third peaks in the emission spectrum) decreases as the polarity of the environment becomes more hydrophobic.[12] The total fluorescence also generally increases as pyrene is transferred to a more hydrophobic domain such as the core of a micelle.[13]

In our fluorescence experiments, the extreme turbidity of our magnetic fluids limited the concentration of the particles to 0.005 wt% $Fe_3O_4$. Figure 4-3a illustrates the emission spectra of pyrene when it was added to the three magnetic fluids at this particle concentration. In these measurements, the final concentration of pyrene in the magnetic fluid was $5.0 \times 10^{-7}$ M. The fluorescence spectra in Figure 4-3a show two anomalies. First, the $I_1/I_3$ ratio changes by less than 5% between the three magnetic fluids and is very

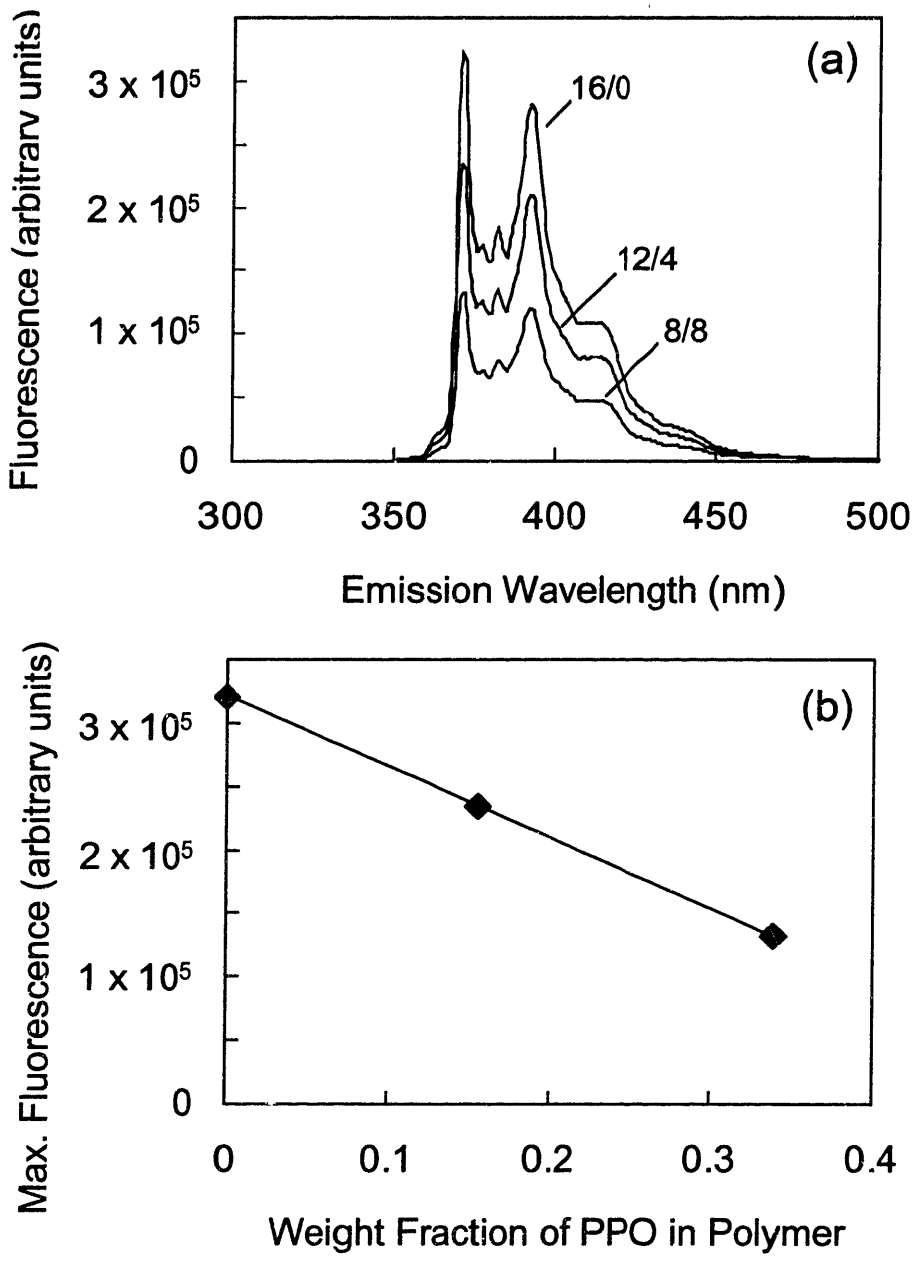


**Figure 4-3.** Fluorescence of pyrene ($5.0 \times 10^{-7}$ M) in various aqueous magnetic fluids (0.005 wt% $Fe_3O_4$). (a) The fluorescence emission decreases as the polymer shell contains more PPO side chains. The $I_1/I_3$ ratio is relatively constant and similar to that in pure water, suggesting that only unsolubilized pyrene fluoresces visibly. (b) The decrease in fluorescence is directly proportional to the PPO content of the polymer shell.

close to the value in a pure aqueous solution ($I_1/I_3$ = 1.87).[12] Second, the total fluorescence decreases as particles with hydrophobic domains are present. Because the $I_1/I_3$ ratio is essentially that of pyrene in water, we hypothesize that we observed only fluorescence from pyrene in the aqueous dispersion medium. Fluorescence from pyrene that partitions into the polymer shell is not observed, possibly because it is solubilized close to the magnetite particle, which may block incoming light from reaching the pyrene molecule or block the fluorescence from reaching the detector. This hypothesis is supported by Figure 4-3b, which shows that the maximum fluorescence (at 371 nm) decreased linearly with the weight fraction of PPO in the stabilizing polymer, suggesting that the uptake of pyrene in the polymer shell was proportional to the PPO content of the shell – a result similar to what we observed for toluene (Figure 4-1b).

The fluorescence intensity of pyrene in the magnetic fluids can be converted to a partition coefficient if we assume that there is no uptake of pyrene into the polymer shell of the 16/0 particles, which is supported by our toluene measurements in Section 4.3.1. With this assumption, as well as the known particle concentration and bound-polymer:magnetite mass ratio (0.8, as determined in Section 2.3.2), we determined that $K_{pw}$' for pyrene in our particles (both 12/4 and 8/8) was $1.18 \times 10^5$ from the slope of the line in Figure 4-3b. In Figure 4-4, this value is compared to other PAH molecules in both 8/8 particles at saturation (closed symbols) and Pluronic micelles at saturation (open symbols) in a linear free energy plot. The dilute pyrene partition coefficient follows the same trend as the naphthalene and phenanthrene partition coefficients that were determined by saturating the particles. In addition, the dilute pyrene partition coefficient in the particles is similar to the $K_{pw}$' value for pyrene in P103 Pluronic micelles that was determined at saturation ($1.62 \times 10^5$).[3] This result suggests that the partitioning data at saturation in Table 4-1 is applicable to more dilute concentrations that might be expected in contaminated water.

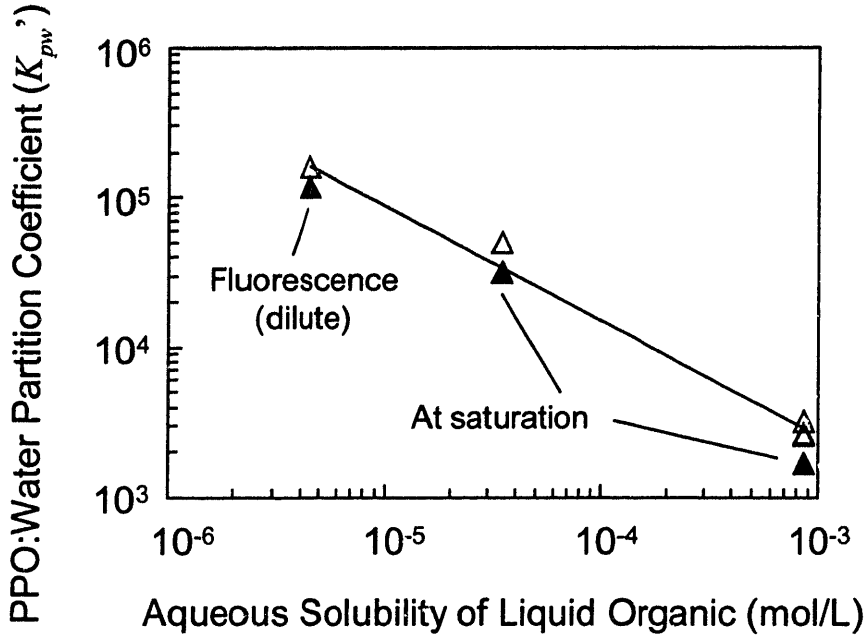


**Figure 4-4.** Linear free energy relationship of PPO-water partition coefficients for PAH solutes. $K_{pw}$' data are presented for organics in the 8/8 magnetic fluids (filled symbols) determined either at saturation or by fluorescence at non-saturated conditions, and a range of Pluronic micelles at saturation (open symbols).[3,4] The data fall on approximately the same line, suggesting that partition coefficients at saturation are approximately the same as in more dilute systems.

## 4.4 Summary

Our extraction experiments showed that the magnetic fluids developed in this work seem promising as potential extractants for organic compounds in water. Using toluene as a model solute, the saturation concentration of the organic was directly proportional to the concentration of particles in the magnetic fluid as well as the volume fraction of PPO in the polymer shell. This result suggested that PPO is responsible for solubilization. This study was extended to other model organics such as PAH's, substituted benzenes, and linear alkanes by measuring the saturation uptake of organics into the 8/8 magnetic particles. Using a free energy relationship, we found that the PPO-

water partition coefficients of the organic species could be correlated to the activity coefficient of the organic in PPO. This parameter gave a measure of the driving force for partitioning into the polymer shell, which was highest for aromatic species and lower for linear alkanes. In addition, the particles showed solubility trends that were nearly identical to PEO-PPO-PEO triblock copolymer (Pluronic) micelles, which contain a PPO-rich core for organic extraction. Using pyrene, a fluorescent organic solute, we extended our study to more dilute magnetic fluids and solutes, and found that the PPO-water partition coefficients were similar to those determined at saturation.

The similarity between our nanoparticles and Pluronic micelles was also noted in Chapter 3, where lattice calculations indicated that the structure in the polymer shell is qualitatively similar to that of a micelle, although with less segregation of PEO and PPO. In our organic solubilization study, we again found that the similarities between the nanoparticle shells and Pluronic micelles were more than compositional, as they seemed to share many of the same extraction characteristics. We can therefore conclude that there is some form of PPO domain formation in the interior region of the polymer shell, although as in Pluronic micelles, phase separation is probably not total and there may be a significant amount of water intermixed with the PPO. Regardless, hydrophobic organics seem to partition strongly into this domain from water, as PPO-water partition coefficients for the organics were on the order of $10^3$-$10^5$ for both the particles and the Pluronic micelles. We note that the nanoparticles offer several advantages over micellar systems, as they retain their PPO domain structure when diluted and have the potential to be recovered by magnetic filtration.

## 4.5 Bibliography

(1) Smith, J. E. J.; Hegg, B. A.; Renner, R. C.; Bender, J. H. *Upgrading Existing or Designing New Drinking Water Treatment Facilities*; Noyes Data Corporation: Park Ridge, NJ, 1991; Vol. 198.

(2) Nagarajan, R.; Barry, M.; Ruckenstein, R. Unusual Selectivity in Solubilization by Block Copolymer Micelles. *Langmuir* **1986**, *2*, 210-215.

(3) Hurter, P. N.; Hatton, T. A. Solubilization of Polycyclic Aromatic Hydrocarbons by Poly(Ethylene Oxide-Propylene Oxide) Block Copolymer Micelles: Effects of Polymer Structure. *Langmuir* **1992**, *8*, 1291-1299.

(4) Paterson, I. F.; Chowdhry, B. Z.; Leharne, S. A. Investigations of Naphthalene Solubilization in Aqueous Solutions of Ethylene Oxide-b-Propylene Oxide-b-Ethylene Oxide Copolymer. *Langmuir* **1999**, *15*, 6187-6194.

(5) Edwards, D. A.; Luthy, R. G.; Liu, Z. Solubilization of Polycyclic Aromatic Hydrocarbons in Micellar Nonionic Surfactant Solutions. *Environ. Sci. Technol.* **1991**, *25*, 127-133.

(6) Kozlov, M. Y.; Melik-Nubarov, N. S.; Batrakova, E. V.; Kabanov, A. V. Relationship Between Pluronic Block Copolymer Structure, Critical Micellization Concentration and Partitioning Coefficients of Low Molecular Mass Solutes. *Macromolecules* **2000**, *33*, 3305-3313.

(7) Yoe, J. H.; Jones, L. Colorimetric Determination of Iron with Disodium-1,2-dihydroxybenzene-3,5-disulfonate. *Ind. Eng. Chem.* **1944**, *16*, 111-115.

(8) Calvert, T. L.; Phillips, R. J.; Dungan, S. R. Extraction of Naphthalene by Block Copolymer Surfactants Immobilized in Polymeric Hydrogels. *AIChE J.* **1994**, *40*, 1449-1458.

(9) Schwarzenbach, R. P.; Gschwend, P. M.; Imboden, D. M. *Environmental Organic Chemistry*; John Wiley and Sons, Inc.: New York, 1993.

(10) Grulke, E. A. Solubility Parameter Values. In *Polymer Handbook*, 4th ed.; Brandrup, J., Immergut, E. H., Grulke, E. A., Eds.; John Wiley and Sons, Inc.: New York, 1999.

(11) Hurter, P. N.; Anger, L. A.; Vojvodich, L. J.; Kelley, C. A.; Cohen, R. E.; Hatton, T. A. Amphiphilic Polymer Solutions as Novel Extractants for Environmental Separations. In *Solvent Extraction in the Process Industries*; Logsdail, D. H., Slater, M. J., Eds.; Elsevier Applied Science: York, U.K., 1993; Vol. 3, pp. 1663-1670.

(12) Dong, D. C.; Winnik, M. A. The Py Scale of Solvent Polarities. *Can. J. Chem.-Rev. Can. Chim.* **1984**, *62*, 2560-2565.

(13) Kabanov, A. V.; Nazarova, I. R.; Astafieva, I. V.; Batrakova, E. V.; Alakhov, V. Y.; Yaroslavov, A. A.; Kabanov, V. A. Micelle Formation and Solubilization of Fluorescent-Probes in Poly(Oxyethylene-B-Oxypropylene-B-Oxyethylene) Solutions. *Macromolecules* **1995**, *28*, 2303-2314.

# Chapter 5

# Magnetic Separation of Nanoparticles

## 5.1 Introduction

High gradient magnetic separation (HGMS) is a process used to separate magnetic materials from a nonmagnetic liquid medium. This process is well suited for the recovery of small magnetic particles that require the application of large magnetic forces for capture. The magnetic fluids that we have developed for organic separation consist of ~8 nm diameter magnetite ($Fe_3O_4$) particles surrounded by a ~9 nm polymer shell that has a high affinity for sparingly soluble organic compounds in water. The nanometer-scale size of the nanoparticles and their high organic affinity suggest that the particles could have several advantages over traditional methods of organic removal from water. However, the use of these particles in a practical separation process requires that the nanoparticles be magnetically removed from the aqueous dispersion medium with a high efficiency. In this chapter, we examine the feasibility of applying HGMS to our aqueous magnetic fluids.

An HGMS system generally consists of a column packed with a bed of magnetically susceptible wires (~50 μm diameter) placed inside an electromagnet. The application of a magnetic field across the column results in large magnetic field gradients around the wire that cause magnetic particles to be trapped on the surface of the wires. The magnetically susceptible wires therefore act as collection elements that form extremely high local magnetic field gradients that are much larger than what could be achieved on the scale of the separator with electromagnets of the same strength.[1] The collection of particles depends strongly upon the creation of large magnetic field gradients because the magnetic force that drives the motion of a magnetic particle is directly proportional to local magnetic field gradient, as well as the volume and magnetization of the particle.[1] HGMS is a good candidate for separation of magnetic nanoparticles from a magnetic fluid because of the strong magnetic field gradients that are needed to overcome the small particle size.

Typically, HGMS has been used to separate micron-scale or larger particles or aggregates. When magnetic nanoparticles have been used as separation agents, the nanoparticles have usually been present as micron-scale aggregates[2] or encapsulated into larger polymer beads.[3] The larger volume of these particles makes magnetic collection by HGMS (or other means) relatively straightforward. Using HGMS to separate individually dispersed nanoparticles is known to be more difficult due to nanoparticle diffusion away from the collection wires.[4-8] For $Fe_3O_4$ nanoparticles, diffusion is predicted to become important when the diameter is less than 40 nm,[4] which is the case for the $Fe_3O_4$ cores of our nanoparticles, as discussed in Chapter 2.

The focus of this chapter is on characterizing the ability of HGMS to remove our nanoparticles from water, including experiments in a bench-scale HGMS column and modeling of the buildup of nanoparticles on the collection wires. A number of models exist in the literature for simulating the behavior of magnetic nanoparticles around a single magnetized collection wire[4-6] or sphere[7-9]; we developed our HGMS model using the methodology of Fletcher[5] but with specific modifications for our nanoparticles and HGMS system. We also compare the capture of our nanoparticles for organic separation with another type of magnetic nanoparticle produced in our laboratory, namely phospholipid-coated nanoparticles that have been shown to have a high affinity for hydrophilic proteins in water.[10] Comparing experimental magnetic filtration data and model predictions for the two systems illustrates the importance of particle size and aggregation on the feasibility of using HGMS for separation. We conclude our discussion with a preliminary study of inducing particle aggregation in our magnetic fluids through the incorporation of polymeric crosslinking agents during synthesis.

## 5.2 Experimental

### 5.2.1 Materials

Polyacrylic acid (50 wt% in water, $M_w$ = 5000), polyacrylic acid (35 wt% in water, $M_w$ = 100,000), polyacrylic acid (35 wt% in water, $M_w$ = 250,000), iron(III) chloride hexahydrate (97%), iron(II) chloride tetrahydrate (99%), ammonium hydroxide (28 wt% in water), hydrochloric acid (37 wt% in water), decanoic acid, Tiron (4,5-

dihydroxy-1,3-benzene-disulfonic acid, disodium salt monohydrate), and TES buffer (N-tris [hydroxymethyl] methyl-2-aminoethane-sulfonic acid) were obtained from Sigma-Aldrich (Milwaukee, WI). Jeffamine XTJ-234 ($CH_3$-O-PEO/PPO-$NH_2$, EO:PO = 6.1:1, $M_w$ = 3000) and Jeffamine XTJ-507 ($CH_3$-O-PEO/PPO-$NH_2$, EO:PO = 1:6.5, $M_w$ = 2000) were obtained as gifts from Huntsman Corporation (Houston, TX). In this work, we consider XTJ-234 to be equivalent to pure PEO and XTJ-507 to be equivalent to pure PPO, and we refer to these polymers as PEO-$NH_2$ and PPO-$NH_2$, respectively. DMPG (1,2-myristoyl-sn-glycero-3-phosphocholine) was provided by Genzyme Pharmaceuticals (Cambridge, MA). All chemicals were used as received.

### 5.2.2 Preparation of Magnetic Fluids

The 16/0, 12/4, and 8/8 magnetic fluids for the HGMS experiments were prepared as described in Sections 2.2.2 and 2.2.3. The nomenclature *x/y* refers to a magnetic fluid produced with a graft copolymer in which *x*% of the carboxylic acid groups in the PAA backbone were reacted with PEO chains and *y*% with PPO chains.

Aggregated 16/0 magnetic fluids were produced by performing the magnetic fluid synthesis in the presence of both the 16/0 graft copolymer and a high molecular weight linear PAA polymer. The reaction conditions were identical to those described in Section 2.2.3, except that high molecular weight PAA was also dissolved in the aqueous reaction mixture. The concentration and molecular weight of the PAA in the reaction mixture was varied to examine the effect on HGMS collection. Directly after the synthesis, the aggregated magnetic fluids were sonicated for two minutes with a Branson Sonifier 450 tip sonicator (160 W output power with a 50% on/off cycle).

Magnetic fluids with phospholipid-coated particles were synthesized by Seyda Bucak (MIT) to compare their filtration performance with our graft copolymer-coated magnetic fluids. A detailed discussion of these magnetic fluids, including the synthetic procedure, is given in the literature.[10] Briefly, these magnetic fluids were prepared by copreciptation of iron(II) and iron(III) chloride in the presence of decanoic acid to form decanoic acid bilayer-coated magnetite nanoparticles. The outer layer of decanoic acid

around the nanoparticles was then exchanged with DMPG phospholipid by dialysis to produce the phospholipid-coated nanoparticles.

### 5.2.3 High Gradient Magnetic Separation

HGMS experiments were performed with a Model L-1CN Frantz Canister Separator, supplied by S.G. Frantz Co., Inc. (Trenton, NJ). The HGMS system consisted of a cylindrical glass column with an internal radius of 0.285 cm and a length of 22.6 cm (a volume of 5.77 $cm^3$) that was randomly packed with 6.2 g of type 430 fine-grade stainless steel wool (40-66 μm diameter) also supplied by S.G. Frantz Co., Inc. The packing occupied 0.79 $cm^3$, resulting in a packing fraction of 14%, which is the maximum packing fraction that could be obtained by hand. For filtration, the column was placed in a 1 cm gap between two metal plates of the separator. A magnetic field between the two plates that could be varied in strength was generated with an attached electromagnet. The direction of the magnetic field was perpendicular to the direction of flow through the column. The maximum flux density generated between the two plates was 1.3 T, as measured with a handheld magnetometer. In all experiments, the maximum magnetic flux density was used, with ± 3% variations due to temperature variations in the electromagnet.

Batch filtration experiments were performed at room temperature by passing 4.5 mL of dilute magnetic fluid (0.25 wt% $Fe_3O_4$) through the column with the electromagnet on. With the magnet on, the majority of particles were trapped in the filter. The concentration of particles that escaped in the filtrate was measured by iron titration, which was performed by adding concentrated hydrochloric acid to dissolve the $Fe_3O_4$ particles and then titrating the resulting $Fe^{3+}$ ions with 4,5-dihydroxy-1,3-benzene-disulfonic acid, disodium salt monohydrate.[11] When the electromagnet was turned off, 4.5 mL of water was passed through the column to collect and resuspend the trapped particles. To remove any remaining particles, the column was backflushed with clean water and acetone and dried with a heat gun.

The second type of HGMS experiment is referred to as magnetic chromatography. In this experiment, water was pumped steadily through the HGMS column with the

magnet on. A 0.5 mL sample of dilute magnetic fluid was then injected with a syringe into tubing directly above the HGMS filter and the HGMS column effluent collected in 1 min batches (for high flow rates, the effluent was collected more frequently). The $Fe_3O_4$ particle concentration in these effluent samples was determined by measuring the turbidity at 365 nm with a Hewlett Packard 8453 UV-Visible spectrometer. In some experiments, the hydrodynamic size of the particles was measured with dynamic light scattering.

### 5.2.4 Particle Characterization

Transmission electron microscopy (TEM) experiments were performed on a JEOL 2010 (200 kV) instrument. Samples were prepared by evaporating dilute suspensions on a carbon-coated film. The median size and polydispersity of the magnetite particles was determined by measuring 150 particles.

Dynamic light scattering (DLS) experiments were performed with a Brookhaven BI-200SM light scattering system at a measurement angle of 90°. The autocorrelation function was fit with an exponential fitting software program to extract the diffusion coefficient, and the Stokes-Einstein equation was used to convert the diffusion coefficient to the hydrodynamic diameter. Intensity-average size distributions provided by the light scattering software were converted to volume-average and number-average size distributions for further analysis. Quoted particle sizes are the average of five measurements. All samples were filtered with a 0.22 μm syringe filter (0.80 μm for the aggregate study) to remove dust.

## 5.3 HGMS Modeling

### 5.3.1 Overview of Model and System

High gradient magnetic separation of micron-size particles has been modeled extensively by considering the important forces on the magnetic particles as they flow through the separator.[1,12,13] Particle capture has been shown to be governed by competition between the magnetic attraction of the particles to the magnetized wires and

the viscous drag on the particles from the flowing fluid. However, when the diameter of the magnetic particles is below approximately 40 nm (for magnetite particles), diffusion of the particles away from the wires becomes important.[4] Particle diffusion is commonly viewed as an additional force that is exerted on the nanoparticles.[5]

The HGMS collection process is illustrated schematically in Figure 5-1. We consider a magnetically susceptible wire of radius $a$ coated with a static nanoparticle buildup of radius $b$. The wire and particle buildup are surrounded by water, with a magnetic nanoparticle located at a distance $r$ and angle $\theta$ from the wire. The illustrated orientation of the wire in Figure 5-1 is reasonable to consider, as the wires in the column are generally oriented in a direction perpendicular to the direction of fluid flow. Our assumption that the wires are also perpendicular to the applied magnetic field can be justified by noting that only wires oriented in this direction will induce magnetic field gradients; wires oriented parallel to the applied field will not induce field gradients in the liquid[14] and are considered to be dead space in the column. The motion of the particle

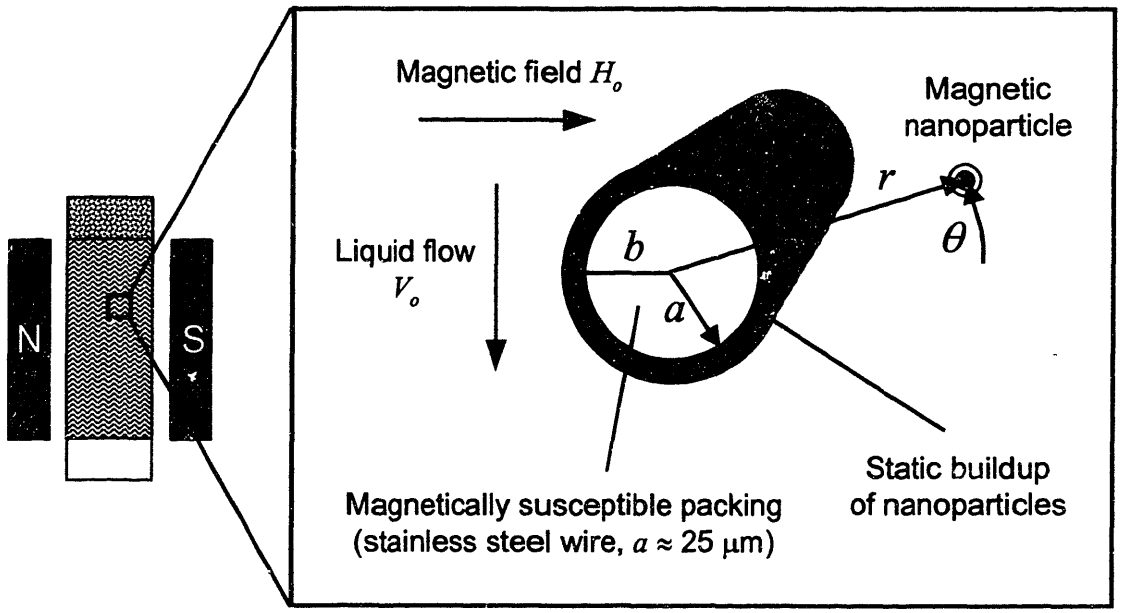


**Figure 5-1.** The HGMS model system is based on an isolated magnetically susceptible wire magnetized perpendicular to its axis, in a flow field oriented perpendicular to both the wire axis and the magnetic field. The wire is coated with a dense static buildup of nanoparticles. A coated magnetic nanoparticle is shown at a distance $r$ and polar angle $\theta$ from the wire center.

in Figure 5-1 is governed by the magnetic, fluid drag, and diffusive forces exerted on it. Rather than deriving the trajectory of the nanoparticle, in this work we use these forces to calculate the region around the wire where the nanoparticles can form a stable buildup.[5] The size and shape of the buildup region gives an indication of the effect of various parameters on HGMS.

The model we develop here for HGMS is based on the development by Fletcher[5] with four key differences. First, as shown in Figure 5-1, the fluid flow is taken to be perpendicular to the direction of the applied magnetic field, in contrast to Fletcher's assumption that the flow and field directions are parallel. Second, Fletcher's theory was derived for the collection of paramagnetic nanoparticles (where the particle magnetization is a linear function of the applied field), whereas our magnetite nanoparticles are superparamagnetic.[15] In addition, our particles are coated with a nonmagnetic polymer or phospholipid layer, as opposed to the bare magnetic particles considered by Fletcher. Therefore, while the magnetic force acts only on the magnetic core, as in Fletcher's model, we must account for the fact that the fluid drag force acts on the entire particle including the shell. Finally, our model uses a low Reynolds number solution for liquid flow around the cylindrical wire,[1,13] which is more applicable than the high Reynolds number solution with a boundary layer used in Fletcher's model, as the Reynolds number (based on the wire diameter) is usually less than unity for HGMS of nanoparticles.

## 5.3.2 Derivation of Forces

### 5.3.2.1 Drag Force

The first force we consider is the fluid drag force acting on a particle in the flow field around the wire. While there is no simple analytical solution for low Reynolds number flow around a cylinder, in the region near the surface, the velocity components of the fluid flow around the wire coated with a dense buildup of particles can be approximated by[13]

$$V_r = -V_o G^- \sin\theta \qquad (5\text{-}1)$$

$$V_\theta = -V_o G^+ \cos\theta \tag{5-2}$$

where G is a geometric factor given by

$$G^\pm = \frac{\ln\left(r/b\right) \pm 0.5\left(1-\left(b/r\right)^2\right)}{2 - \ln \mathrm{Re}_b} \tag{5-3}$$

In this equation, $\mathrm{Re}_b$ is the Reynolds number based on $b$:

$$\mathrm{Re}_b = \frac{2b\rho V_o}{\eta} \tag{5-4}$$

where $\rho$ and $\eta$ are the fluid density and viscosity, respectively. Given this velocity profile of the fluid, the radial and azimuthal fluid drag force components on a nanoparticle in the fluid are given by

$$F_{vr} = -6\pi\eta R_{shell}\left(\frac{dr}{dt} + V_o G^- \sin\theta\right) \tag{5-5}$$

$$F_{v\theta} = -6\pi\eta R_{shell}\left(r\frac{d\theta}{dt} + V_o G^+ \cos\theta\right) \tag{5-6}$$

where $R_{shell}$ is the total nanoparticle radius including the coating. In these equations, the sums in the brackets represent the motion of the particle relative to the fluid.

#### 5.3.2.2 Diffusive Force

Particle diffusion can be described as a driving force that arises from a gradient in particle concentration. If $n$ is defined as the particle number concentration at $r$ and $\theta$, then the diffusive "force" acting on particles around the wire can be written as[5]

$$F_{dr} = -\frac{kT}{n}\frac{dn}{dr} \tag{5-7}$$

$$F_{d\theta} = -\frac{kT}{n}\frac{1}{r}\frac{dn}{d\theta} \tag{5-8}$$

We assume that nanoparticles in the dense static buildup around the wire are frozen in place and unable to diffuse, but particles outside this buildup are subject to diffusion.

#### 5.3.2.3 Magnetic Force

The magnetic force on the particle is determined by first solving for the magnetic field, $\mathbf{H}(r,\theta)$, that is induced in the liquid by the presence of a wire with the geometry shown in Figure 5-1:[1,5]

$$H_r = \left( \frac{M_{wire} a^2}{2r^2} + H_o \right) \cos\theta \tag{5-9}$$

$$H_\theta = \left( \frac{M_{wire} a^2}{2r^2} - H_o \right) \sin\theta \tag{5-10}$$

In these equations, $H_o$ is the externally applied magnetic field and $M_{wire}$ is the magnetization of the wire. The magnetic force on a particle is then calculated from the magnetic field using

$$\mathbf{F_m} = \mu_o V_p \mathbf{M_p} \cdot \nabla \mathbf{H} \tag{5-11}$$

The result of this product (for our wire geometry) has been derived previously for paramagnetic particles, in which the particle magnetization is a linear function of the local magnetic field, $\mathbf{M_p} = \chi \mathbf{H}$.[1,5] Here, our magnetite nanoparticles are intrinsically superparamagnetic,[10,15] meaning that the $Fe_3O_4$ core magnetization, $\mathbf{M_{core}}$, is described by a Langevin function of the magnetic field.[16] However, at magnetic fields greater than approximately 1 T, as are encountered in our HGMS column, the particle cores become magnetically saturated and the core magnetization effectively reaches a constant value. With these saturation conditions, the core magnetization is a vector of constant magnitude $M_{core}$ in the direction of the magnetic field:

$$\mathbf{M_{core}} = M_{core} \frac{\mathbf{H}}{|\mathbf{H}|} \tag{5-12}$$

If the magnitude of the magnetic field in the liquid, |**H**|, is approximately equal to the applied magnetic field, $H_o$, then the core magnetization can be approximated as

$$\mathbf{M}_{\text{core}} \approx \frac{M_{core}}{H_o}\mathbf{H} \tag{5-13}$$

With this approximation, we can use the solution for paramagnetic nanoparticles[1,5] by substituting $\chi = M_{core}/H_o$; this approach has been used previously to simplify problems for superparamagnetic particles.[6] The magnetic force components on a nanoparticle are therefore given by

$$F_{mr} = -\frac{4\pi\mu_o M_{wire} M_{core} a^2 R_{core}^3}{3r^3}\left(\frac{M_{wire} a^2}{2H_o r^2} + \cos 2\theta\right) \tag{5-14}$$

$$F_{m\theta} = -\frac{4\pi\mu_o M_{wire} M_{core} a^2 R_{core}^3}{3r^3}\sin 2\theta \tag{5-15}$$

where $R_{core}$ is the core radius of the magnetic nanoparticle.

## 5.3.3 Derivation of Limit of Nanoparticle Buildup

### 5.3.3.1 Force Balance

The response of a nanoparticle to the magnetized collection wire is determined by a force balance: $\mathbf{F_v} + \mathbf{F_d} + \mathbf{F_m} = 0$. We have neglected inertia (the acceleration term) because of the small particle size. Balancing the radial and azimuthal force components (Equations 5-5–5-8, 5-14, and 5-15), making the equations nondimensional by substituting $r_a = r/a$, and rearranging, we obtain the following equations for the nanoparticle trajectory in the fluid near the static buildup:

$$\frac{dr_a}{dt} = -\tau_v G^- \sin\theta - \tau_d \frac{1}{n}\frac{dn}{dr_a} - \tau_m\left(\frac{M_{wire}}{2H_o r_a^5} + \frac{\cos 2\theta}{r_a^3}\right) \tag{5-16}$$

$$r_a \frac{d\theta}{dt} = -\tau_v G^+ \cos\theta - \tau_d \frac{1}{r_a n}\frac{dn}{d\theta} - \tau_m \frac{\sin 2\theta}{r_a^3} \tag{5-17}$$

where $\tau_v$, $\tau_d$, and $\tau_m$ are constants associated with the fluid drag force, diffusion, and magnetic force, respectively:

$$\tau_v = \frac{V_o}{a} \tag{5-18}$$

$$\tau_d = \frac{kT}{6\pi\eta R_{shell} a^2} \tag{5-19}$$

$$\tau_m = \frac{2\mu_o M_{wire} M_{core} R_{core}^3}{9\eta R_{shell} a^2} \tag{5-20}$$

While these constants reflect the rates of particle transport by these processes, they cannot be compared directly to give a measure of the relative importance of these forces because $G^-$ and $G^+$ are not necessarily of order unity in Equations 5-16 and 5-17.

### 5.3.3.2 Definition of Limiting Conditions

Rather than solve the particle trajectory equations in Equations 5-16 and 5-17 numerically, we instead used these equations to determine the limiting radius of the static buildup of particles around the wires following the methodology of Fletcher.[5] The outer limit of static buildup of nanoparticles (defined as $b_L$) is the outermost point at which a particle is motionless at the interface between the static buildup and the liquid. This point is reached when $dr_a/dt = 0$ and $d\theta/dt = 0$ at $r = b \equiv b_L$, or in dimensionless variables, $r_a = b/a \equiv b_{La}$. However, in evaluating $G^-$ and $G^+$ (the geometric factors from the velocity profile), we use $r = b + R_{shell}$, as the nanoparticle center of mass can approach no closer than $R_{shell}$ to the static buildup interface. Evaluating these geometric factors for a particle sitting on the static buildup interface, $G_b$, yields

$$G_b^{\pm} = \frac{\ln\left(\frac{b+R_{shell}}{b}\right) \pm 0.5\left(1-\left(\frac{b}{b+R_{shell}}\right)^2\right)}{2-\ln \mathrm{Re}_b} \tag{5-21}$$

As $R_{shell} << b$ for nanoparticles, a Taylor series expansion for both terms in the numerator yields

$$G_b^- = 0 \qquad G_b^+ = \frac{2R_{shell}/b}{2 - \ln \mathrm{Re}_b} \tag{5-22}$$

The outermost limit of static nanoparticle buildup is therefore found by substituting the conditions $dr_a/dt = 0$, $d\theta/dt = 0$, $r_a = b/a \equiv b_{La}$, and $G^{\pm} = G_b^{\pm}$ in Equations 5-16 and 5-17.

#### 5.3.3.3 Diffusion Buildup Limit

Following the methodology of Fletcher[5], we derive the static buildup limit for two limiting cases: one in which particle capture is purely diffusion-limited and another in which capture is purely drag force-limited. To derive the diffusion limit of static buildup, we make the additional assumption that $V_o = 0$ (i.e. a stagnant fluid). Making these substitutions in the radial force balance (Equation 5-16) and integrating the term $dn/dr_a$ with the boundary condition that $n = n_o$ when $r_a = \infty$ yields the equation

$$n = n_o \exp\left(\frac{\tau_m}{2\tau_d}\left(\frac{M_{wire}}{4H_o r_a^4} + \frac{\cos 2\theta}{r_a^2}\right)\right) \tag{5-23}$$

which is the nanoparticle concentration profile in a stagnant liquid. Neglecting the higher order term and making the substitution that $n = n_s$ (the number density of the static buildup of densely packed particles) at $r_a = b_{La}$ we obtain the dimensionless limit of static buildup in a purely diffusion-limited case:

$$b_{La} = \left(\frac{\tau_m}{\tau_d}\frac{\cos 2\theta}{2\ln\left(n_s/n_o\right)}\right)^{1/2} \tag{5-24}$$

This result is identical to that obtained by Fletcher.[5] In this equation, $n_s$ can be estimated by assuming simple cubic packing in the dense static buildup of particles, where $n_s$ =

$1/(2R_{shell})^3$.[5] We could also have derived Equation 5-24 from the azimuthal force balance (Equation 5-17) with the same assumptions.

#### 5.3.3.4 Drag Force Buildup Limit

The limit of static buildup in a purely drag force-limited case is found by substituting the limiting conditions $dr_a/dt = 0$, $d\theta/dt = 0$, $r_a = b/a \equiv b_{La}$, and $G^{\pm} = G_b^{\pm}$ with the additional assumption that $dn/dr_a = dn/d\theta = 0$ (i.e. no diffusion). Making these substitutions in the radial force balance does not yield a limit since $G_b^- = 0$. In the azimuthal force balance, however, these substitutions yield an equation for the dimensionless limit of static buildup in a purely drag force-limited case:

$$\frac{b_{La}^2}{2 - \ln \mathrm{Re} - \ln b_{La}} = -\frac{\tau_m}{\tau_v}\frac{a}{R_{shell}}\sin\theta \tag{5-25}$$

This is a new result for low Reynolds number flow (with the geometry shown in Figure 5-1) that must be solved numerically for $b_{La}$. In this equation, we have factored $b_{La}$ from $\mathrm{Re}_b$, leaving the traditional Reynolds number Re based on $a$:

$$\mathrm{Re} = \frac{2a\rho V_o}{\eta} \tag{5-26}$$

#### 5.3.3.5 Dimensionless Force Ratios

The actual limit of static buildup of particles around the wire is defined as the region in which both diffusion and fluid drag on the particle are overcome by the magnetic force. This region is defined by the area inside both the diffusion and drag force buildup limits in Equations 5-24 and 5-25, respectively.[5] These equations also yield dimensionless quantities that show the relative importance of the forces acting on the nanoparticles in the HGMS column. The diffusion limit is dependent on the dimensionless variable $K_{md} \equiv \tau_m/\tau_d$, which is a ratio of the magnitude of the magnetic force to diffusive force:

$$K_{md} = \frac{\tau_m}{\tau_d} = \frac{4\pi\mu_o M_{wire} M_{core} R_{core}^3}{3kT} \tag{5-27}$$

The drag force limit is a function of $K_{mv} \equiv \tau_m a/\tau_v R_{shell}$, which is a measure of the magnitude of the magnetic force relative to the fluid drag force near the buildup interface:

$$K_{mv} = \frac{\tau_m}{\tau_v}\frac{a}{R_{shell}} = \frac{2\mu_o M_{wire} M_{core} R_{core}^3}{9\eta R_{shell}^2 V_o} \tag{5-28}$$

While $\tau_m/\tau_v$ (or $V_m/V_o$ using conventional nomenclature) is often used as a measure of the magnetic force to the drag force, our derivation indicates that this ratio should be multiplied by $a/R_{shell}$ to give a better estimate of the relative importance of these forces near the wire or static buildup. This additional factor (>>1 for nanoparticles) accounts for the fact that the fluid velocity near the edge of the buildup is much lower than it is far from the wire. It is this velocity that determines whether a particle is captured statically, rather than the velocity far from the wire. Our model for HGMS, which yields the limit of static buildup of nanoparticles around the magnetized collection wires, can be used to explain our bench scale experimental results.

## 5.4 Magnetic Filtration Experiments

### 5.4.1 Batch Filtration Results

The ability of high gradient magnetic separation to remove our nanoparticles from water was initially examined in batch filtration experiments in our bench-scale HGMS system. In these experiments, we investigated the effect of the particle concentration and suspension velocity on the collection efficiency by passing small volumes of magnetic fluid through the column. We also examined the effect of HGMS on the particle size distribution by repeatedly passing the same particles through the column – a process we refer to as magnetic washing of the particles because it was originally used to remove free polymer and ions from the magnetic fluids. In all HGMS experiments performed in this work, we used freshly prepared magnetic fluids, although it is expected that magnetic

nanoparticles that are loaded with organic compounds will show similar behavior in the HGMS column.

A series of magnetic washing experiments was performed in which a suspension of the particles was passed through the HGMS filter with the magnet on, and the particles trapped in the filter then recovered by turning off the magnet and passing fresh water through the filter; this cycle of filtration and collection processes was then repeated a number of times. Approximately one column volume of diluted magnetic fluid (0.25 or 0.50 wt% $Fe_3O_4$) was passed through the column at a flow velocity of 0.1 cm/s in these experiments. In all cases, the nanoparticles resuspended spontaneously when they were flushed from the column with pure water. The concentration of particles that escaped in the filtrate on each pass was measured to determine the efficiency of HGMS collection.

Figure 5-2 shows the fraction of particles lost on each pass of the suspension through the filter, which is defined as a ratio of the filtrate concentration of $Fe_3O_4$ particles to the inlet concentration. The inlet concentration of particles during each individual pass was adjusted for particles lost in prior passes. A significant number of particles were lost from the filter on the first pass, regardless of the type of particle. For example, when 0.25 wt% 16/0 particles were passed with the magnet on, 9.4% of the $Fe_3O_4$ particles (by mass) escaped the HGMS filter. When the trapped particles were collected with fresh water and passed through the filter again, the losses dropped to 4.7%. After three passes through the filter, the particle losses were relatively constant in subsequent filtrations, but did not approach zero. The 12/4 and 8/8 particles followed a similar trend, although they appeared to have been slightly easier to capture initially. After three passes, their performance was similar to that of the 16/0 particles in that they were captured with approximately 98% efficiency. The effect of the particle concentration on capture is shown in Figure 5-2 for the 8/8 particles. When the concentration of particles was doubled, the relative losses were nearly identical, indicating that the HGMS column did not become saturated with particles during filtration and that the losses could not be ascribed to a lack of available surface area on the packing for particle capture.

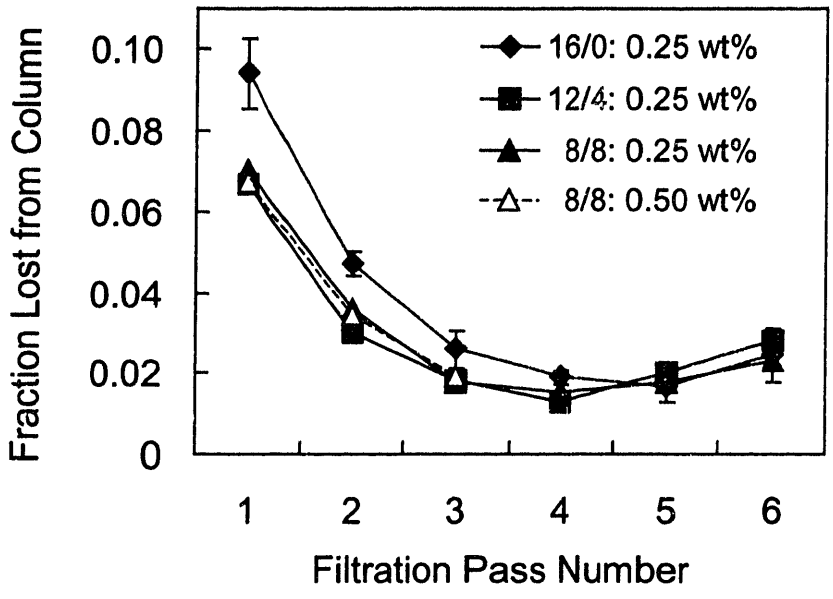


**Figure 5-2.** Batch filtration results from a repetitive cycle of magnetic washing. In each pass, a column volume of a particle suspension was passed through the HGMS filter at 0.1 cm/s with the magnet on and the concentration of particles that escaped in the filtrate was measured. The particles trapped in the filter were then collected with the magnet off and passed again to the filter. The initial concentration was recalculated for each pass accounting for previously lost particles.

The filtration performance improved after several passes because the smallest particles in the size distribution were lost preferentially during the first several passes, while the larger particles were more readily captured by the magnetic filter, as suggested by the equation for the magnetic force on a particle, which is proportional to the volume of its magnetic core (Equation 5-11). This is evident in Figure 5-3a, where the size distribution determined by TEM for the $Fe_3O_4$ core of the 16/0 particles lost in the first pass is compared to the initial core size distribution. The median core diameter of the particles lost in the first filtrate (4.6 nm) was significantly smaller than the initial median diameter (7.5 nm), indicating that the first filtrate was composed almost entirely of the smallest particles in the initial distribution.

We also used dynamic light scattering to determine the hydrodynamic diameter of the particles collected during the sequence of magnetic filtrations. Figure 5-3b shows the number-average hydrodynamic diameter of the 16/0 particles before, during, and after the first three passes of magnetic washing. The average hydrodynamic diameter of the

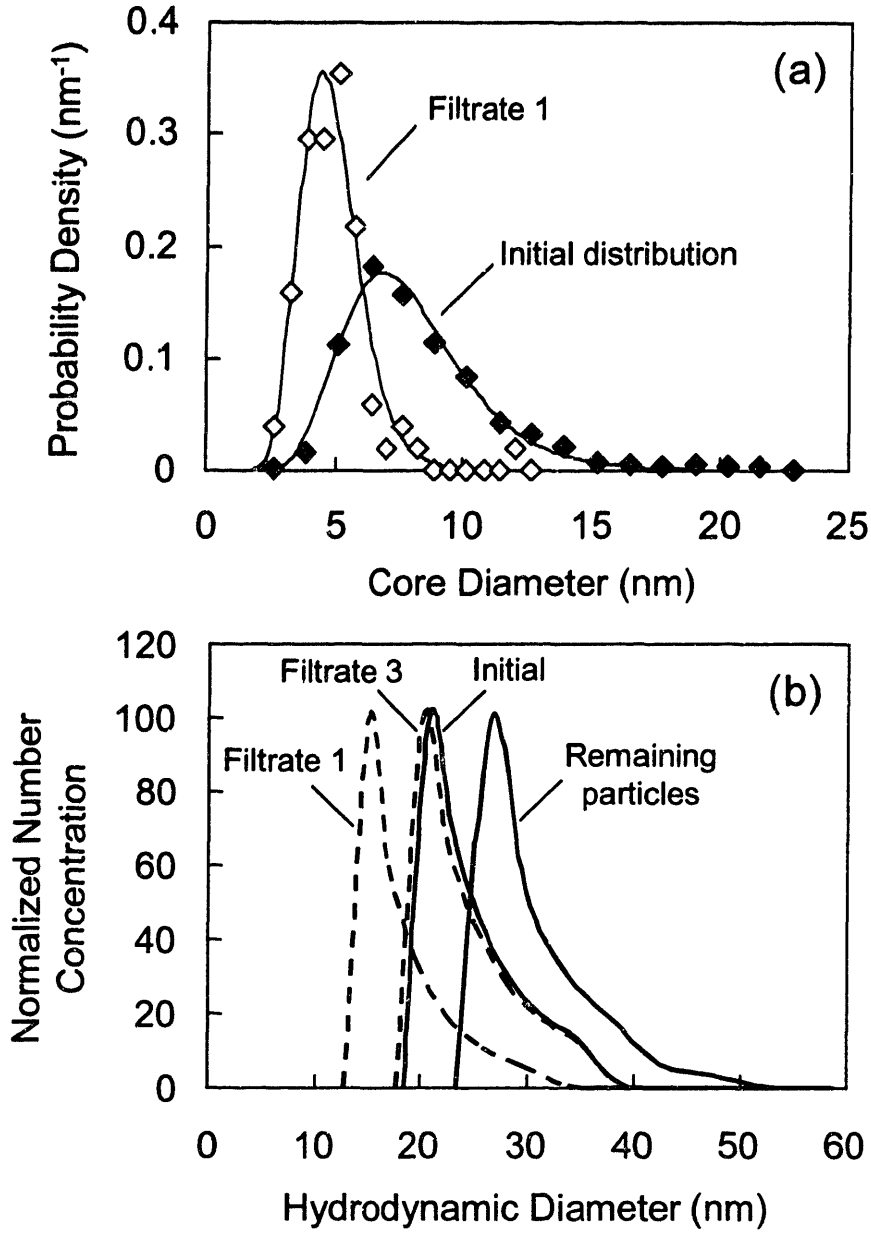


**Figure 5-3.** Effect of size on particle capture during magnetic washing. (a) The $Fe_3O_4$ core size distribution (from TEM) of particles in the first 16/0 filtrate is compared to the initial distribution. (b) The hydrodynamic diameter (from DLS) of particles in the first and third 16/0 filtrate is compared to the initial distribution.

particles lost in the first pass was significantly smaller than the initial average diameter, which is consistent with the TEM results. The lost particles increased in size as the washing proceeded such that by the third filtration pass, the particles lost in the filtrate were similar in size to the initial particles. This observation may explain why the particle losses reached an approximately constant level after three passes. In addition, the remaining particles showed a bias to higher diameters after the three washes.

These preliminary magnetic washing results showed that small volumes of the graft copolymer-stabilized magnetic fluids could be passed through the HGMS column with approximately 90% particle retention, which could be improved to approximately 98% retention after removing the smallest particles in the size distribution. However, a practical separation process would require that the HGMS column process much larger volumes of magnetic fluid with essentially no particle losses. To determine which force opposing capture (i.e. diffusion or fluid drag) was primarily responsible for our inability to capture all of the particles, we investigated the effect of the flow velocity on particle capture, as shown in Figure 5-4a. In these experiments, we performed one batch HGMS filtration of 4.5 mL of 16/0 magnetic fluid and measured the percentage of particles lost in the filtrate. At low flow velocities near 0.1 cm/s (the value used in our previous experiments), the effect of the flow velocity was small, as the velocity could be increased or decreased by nearly an order of magnitude with less than 10% change in filtration performance. In contrast, the concentration of particles that were lost in the filtrate increased dramatically above 1 cm/s.

These experimental results show that HGMS collection of these nanoparticles can be divided into two regimes: a high velocity regime in which fluid drag is the primary force competing against the magnetic force of attraction towards the wires, and a low velocity regime in which the magnetic force competes primarily with particle diffusion. This hypothesis is consistent with the dimensionless quantities $K_{md}$ and $K_{mv}$ that were derived in Equations 5-27 and 5-28 and express the ratio of the magnetic force on a particle to the diffusive and fluid drag forces, respectively. Of these, $K_{mv}$ is a function of $V_o$, as the drag force is directly proportional to the flow velocity in the HGMS column. We calculated these dimensionless force ratios for our particles using standard values of

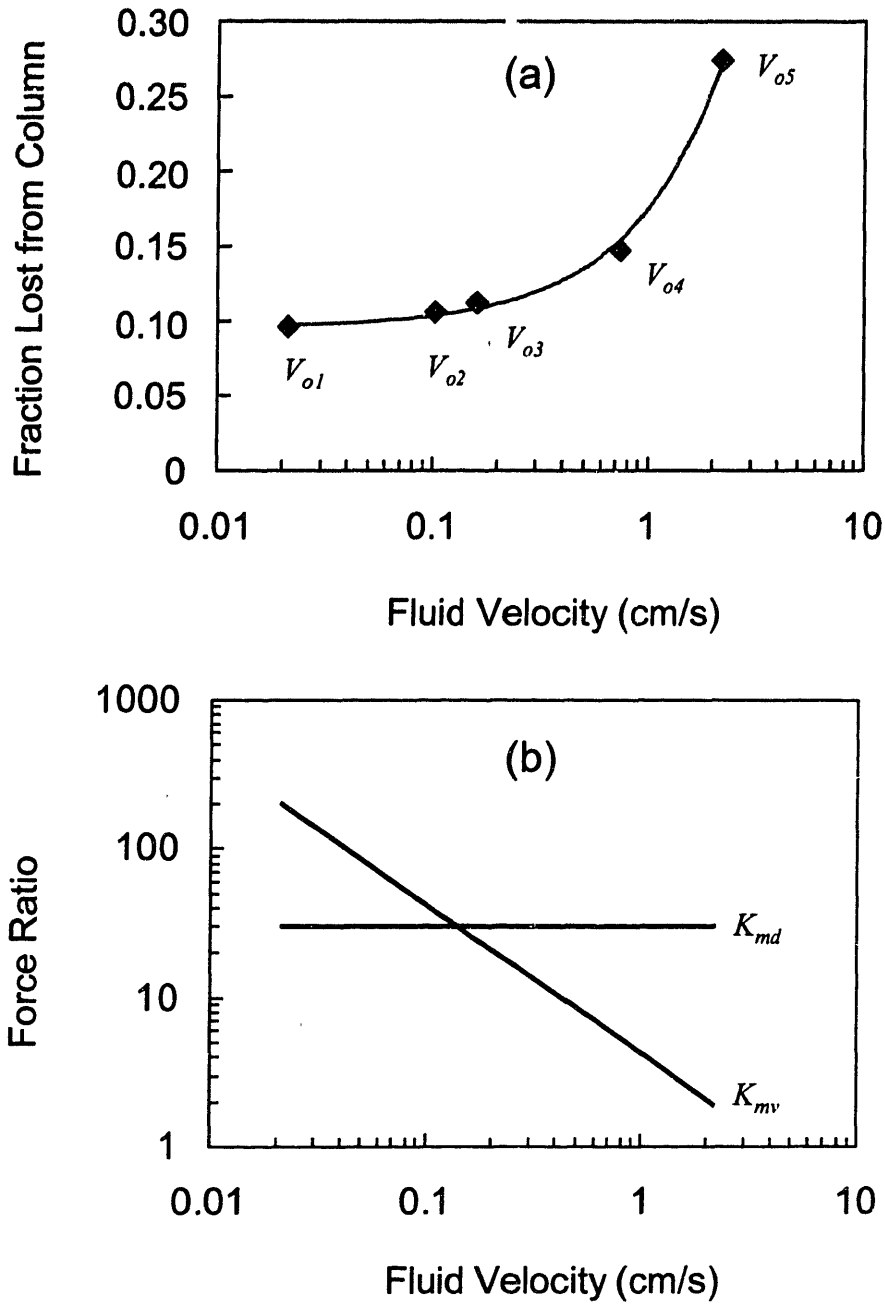


**Figure 5-4.** (a) Effect of fluid velocity on batch HGMS capture of 16/0 magnetic fluid. In this experiment, 4.5 mL of magnetic fluid was passed through the HGMS column (void volume = 5.0 mL) at various flow velocities ($V_o$). The concentration of particles lost in the filtrate was measured and normalized by the initial concentration. (b) Effect of flow velocity on the dimensionless numbers expressing the ratio of the magnetic force to the diffusive force ($K_{md}$) and fluid drag force ($K_{mv}$).

$\rho$ and $\eta$ for water, our average measured values of $R_{core}$ (3.75 nm) and $R_{shell}$ (13 nm) for the individual nanoparticle dimensions (Chapter 2), and the nominal radius of the wires for $a$ (25 μm). The measured saturation magnetization of the nanoparticles was used for $M_{core}$ (63 emu/g) because the applied magnetic field in the column (1.3 T) was sufficient to saturate the nanoparticles (Chapter 2). As this magnetic field was also sufficient to saturate the stainless steel wires, $M_{wire}$ was obtained from the literature value of its saturation magnetization (153 emu/g).[1] The variation of these quantities with flow velocity is shown in Figure 5-4b, which illustrates that at high flow velocities, $K_{mv}$ is small and the drag force is limiting. As the flow velocity is reduced, $K_{mv}$ becomes large and below ~0.1 cm/s, $K_{md}$ dominates particle retention. As $K_{md}$ does not depend on $V_o$, the flow velocity no longer has an effect on the HGMS collection efficiency. This result has also been predicted theoretically by Fletcher.[5]

### 5.4.2 Buildup Profile Calculations

Our model for HGMS of magnetic nanoparticles can be applied more rigorously to the conditions in Figure 5-4a by calculating the diffusion and drag force limit of static particle buildup (Figure 5-5a) for the five flow velocities using Equations 5-24 and 5-25. In this analysis, we used standard values of $\rho$, $\eta$, and $a$, and experimentally determined values of $R_{core}$, $R_{shell}$, $M_{core}$, and $M_{wire}$ for our nanoparticles, as discussed above. The number densities $n_s$ and $n_o$ were calculated using simple cubic packing and the initial magnetite concentration (0.25 wt%), respectively, yielding $n_s/n_o = 24.0$ for a nanoparticle with average dimensions. The diffusion buildup limit, shown in Figure 5-5a, is independent of the flow velocity as it was derived for a stagnant fluid. In contrast, the drag force buildup limit increases in size as the velocity is decreased, as the fluid drag force on the particle is overcome by the magnetic force at increasing distances. The experimentally observed influence of the flow velocity can be understood by comparing the two limits of static buildup, as the area of overlap of the two profiles represents the region where the polymer-coated nanoparticles can be statically trapped. For $V_{o1}$, $V_{o2}$, and $V_{o3}$ ($V_o \leq 0.2$ cm/s), the drag force limit is sufficiently large (meaning the fluid drag force is sufficiently small) that the diffusion dominates particle collection. At $V_{o4}$ and $V_{o5}$ ($V_o \geq 0.7$ cm/s), the fluid drag force becomes limiting because the region of static buildup

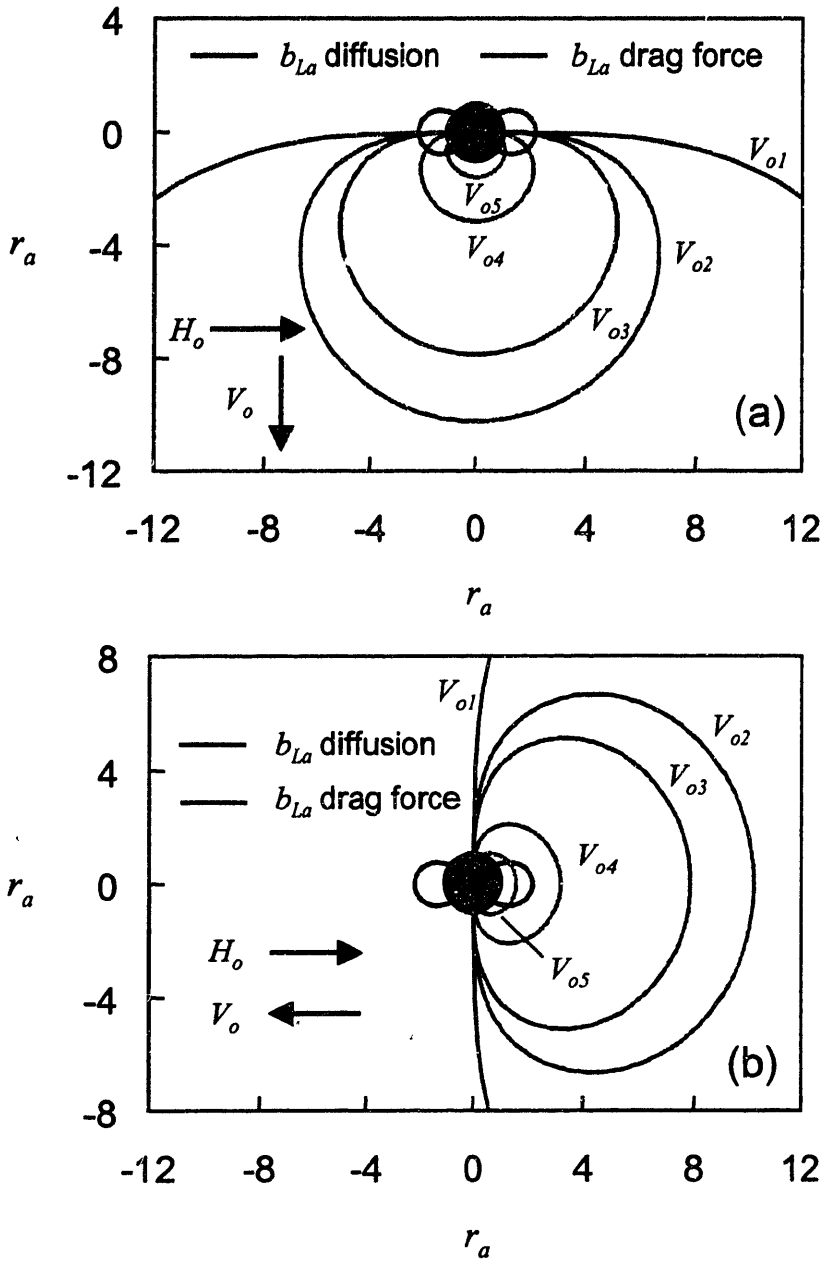


**Figure 5-5.** Predicted diffusion (black line) and fluid drag force (gray line) limits of static buildup for polymer-coated nanoparticles. The actual limit of static buildup at a given flow velocity is defined by the intersection of areas inside the diffusion- and drag force-limited curves. The circle represents the cylindrical wire and the dimensionless distance ($r_a$) is scaled by the wire radius. (a) Predictions when the magnetic field and fluid flow are perpendicular, as is the case for our apparatus and experiments. (b) Predictions when the magnetic field and fluid flow are parallel (and opposite).

decreases in size as the outer part of the diffusion limit is eroded. The theoretically predicted transition velocity between the two regimes ($V_{o3} \rightarrow V_{o4}$) is consistent with the experimental data in Figure 5-4a.

Our theory predicts that when the magnetic field is applied perpendicular to the direction of fluid flow (as in our HGMS column), static particle capture is only possible in two regions below the wire. Only in these two regions do the radial component of the magnetic force act towards the wire center and the azimuthal component of the magnetic force act in the upstream direction. Above the wire, the azimuthal component of the magnetic force acts in the same direction as the fluid flow and capture is not possible. Turbulent flow that might cause eddies below the wire is not a concern for the velocities used here, as the Reynolds number is less than or equal to 1 for all five flow velocities. Our theory can also be applied to the case in which the fluid flow is parallel to the applied magnetic field. The diffusion buildup limit (Equation 5-24) is unchanged, while the drag force buildup limit (Equation 5-25) is modified by changing $\sin\theta$ to $-\cos\theta$. As shown in Figure 5-5b, the predicted result of rotating the fluid flow direction by $-90^\circ$ is rotation of the drag force buildup limit by $90^\circ$. Although it may appear counterintuitive, capture occurs on the upstream half of the wire when the fluid flow is parallel to the applied field and the downstream half of the wire when the fluid flow is perpendicular to the applied field.[1] In addition, the transition velocity between the two HGMS regimes is higher in this configuration, as capture at $V_{o4}$ becomes limited entirely by the diffusion-limited lobe. However, once in the diffusion-limited regime, the fluid flow direction should have no effect on HGMS efficiency, as the total static buildup volume remains the same (i.e. the downstream halves of both lobes in Figure 5-5a and the upstream lobe in Figure 5-5b).

The most important difference between our model and that of Fletcher[5] is the different functional form of the drag force buildup limit. This difference arose because we used a velocity profile that is more appropriate for low Reynolds number flow. In Fletcher's derivation, the drag force buildup limit was derived for high Reynolds number flow (a nonphysical situation in this case) and then modified with a boundary layer solution around the solid buildup. If Fletcher's model is modified for the other changes

we introduced, such as the perpendicular flow and field, particle superparamagnetism, and presence of a nonmagnetic shell, we can directly compare the effect of the different fluid flow solutions. Figure 5-6 shows that Fletcher's boundary layer method predicts a drag force buildup volume that is approximately 20% larger than our prediction. Regardless, both models predict the correct transition velocity between the two regimes for our experimental data. One of the weaker assumptions of our model (and Fletcher's) is the assumption that the particle buildup is cylindrical in the fluid flow equations. Figure 5-6 shows that the buildup profiles are clearly not cylindrical and a significant drag force may be exerted on the nanoparticle buildup.

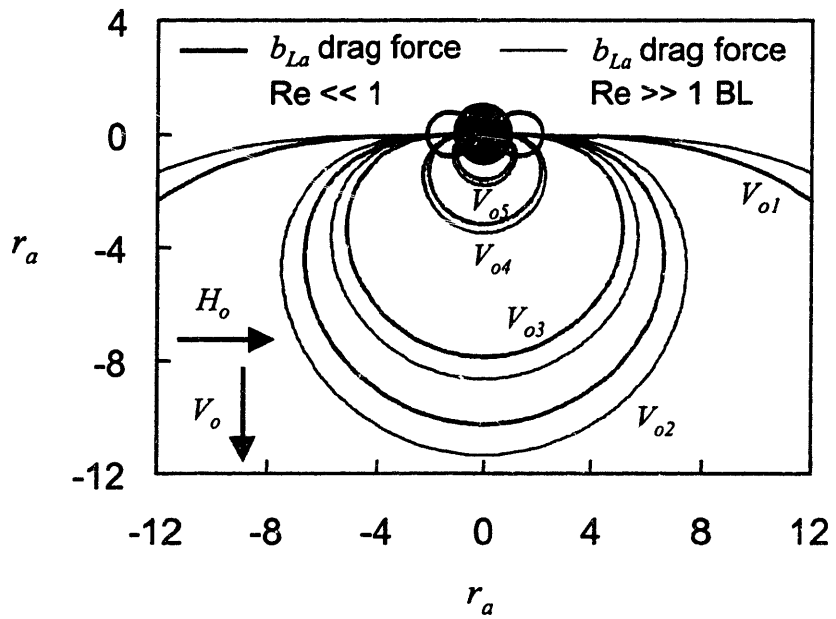


**Figure 5-6.** Comparison of model predictions with different velocity profile solutions. The thin lines represent the drag force buildup limit calculated using Fletcher's high Reynolds number flow solution modified with a boundary layer (BL).[5] The thick lines represent our predictions using the low Reynolds number flow solution that more accurately describes flow near the buildup interface. The diffusion buildup limit is not affected as it represents nanoparticle buildup in a stagnant fluid.

The model can also be used to predict the effect of particle size on HGMS capture. We determined the total static capture area as a function of the fluid velocity by integrating the common area inside both the diffusion and drag force limits (not including the wire) for particles with different magnetite core diameters. In these calculations, we

fixed the $n_s/n_o$ ratio at 24.0 and set the polymer shell thickness constant at 9.4 nm, allowing $R_{shell}$ to vary. The results are shown in Figure 5-7a, where the total static buildup volume has been normalized by the wire volume. This figure shows that the effect of the flow velocity is qualitatively similar for particles of different core diameters, in that the transition velocity occurs at approximately 0.2 cm/s, with particle collection being entirely diffusion-limited below this velocity and drag force-limited above this velocity. Figure 5-7b illustrates the shape of the static buildup of nanoparticles as $V_o$ approaches zero for various core diameters. In the limit of $V_o \rightarrow 0$, the static buildup is defined by the lower half of both diffusion-limited lobes. Figure 5-7 shows that the total static buildup volume increases dramatically with increasing core size. For example, in the diffusion-limited regime, the normalized static buildup volume increases from 0.51 for 7.5 nm diameter $Fe_3O_4$ cores to 5.7 for 15 nm cores. Figure 5-7b also shows that for small particles with a 4 nm core diameter, the dimensionless buildup limit is less than unity for all angles, which has no physical significance and is equivalent to no static buildup. By setting $b_{La} = 1$ at $\theta = 0$, we found that the minimum particle core diameter that can form any static buildup is 4.5 nm, which is similar to the result calculated by Takayasu et al.[6]

Dynamic light scattering results (Section 2.3.5) have shown that approximately 10% of the particles are present as aggregates with a diameter of 60-125 nm. To calculate the static buildup volumes of these aggregates around the wire, we assumed that they were composed of individual particles with a core diameter of 7.5 nm and total diameter of 26 nm. The dimensionless ratio of the magnetic force to the diffusive force for dense aggregates of individual particles that maintain the same volume fraction of magnetite as the individuals is given by

$$K_{md,agg} = NK_{md,ind} \tag{5-29}$$

where $N$ is the number of particles in the aggregate, each with $K_{md,ind}$. The dimensionless ratio of the magnetic force to the fluid drag force for dense aggregates of individual

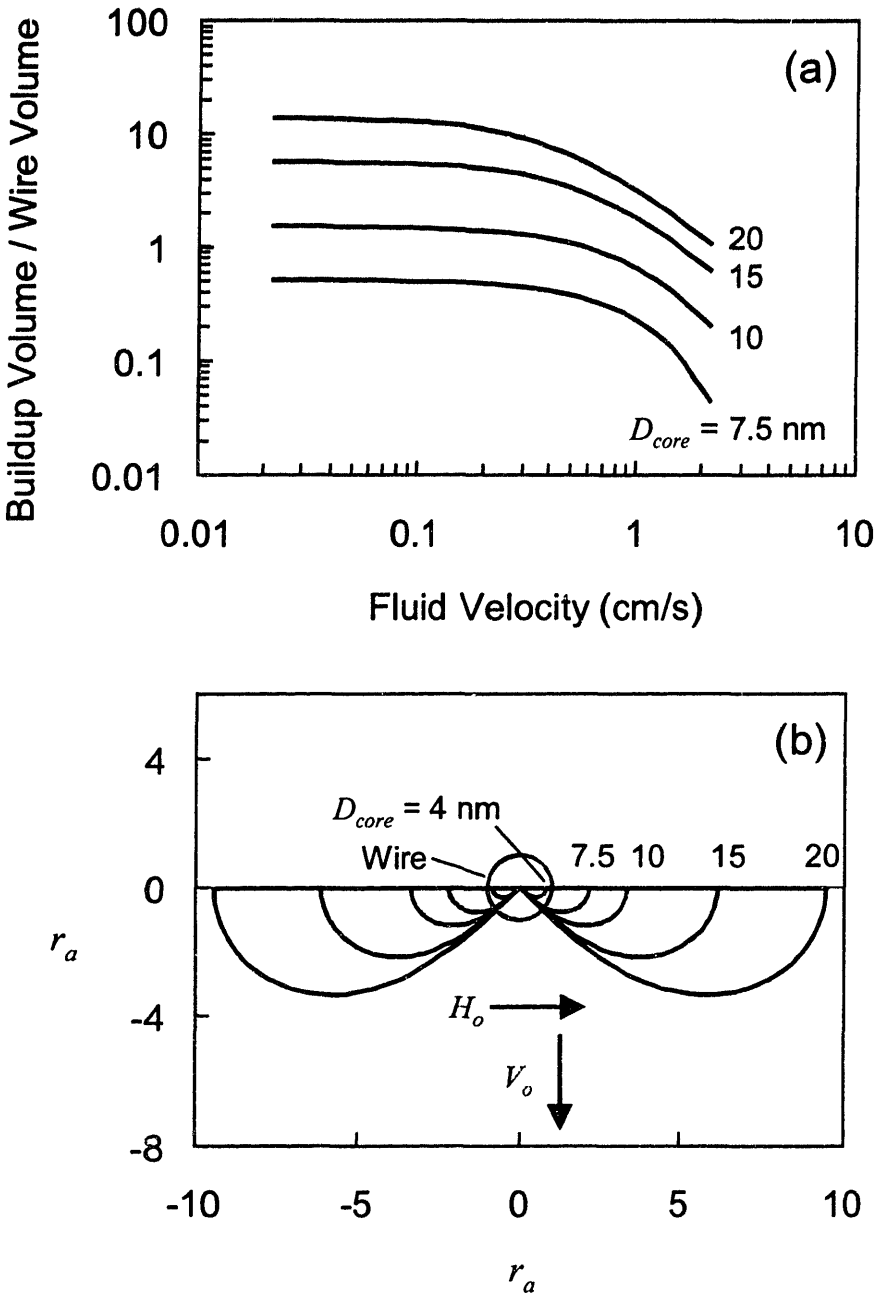


**Figure 5-7.** Effect of the nanoparticle core size on the static buildup volume. (a) The calculated volume of the static buildup limit (normalized by the wire volume) is plotted against the flow velocity ($V_o$). (b) The static buildup limit for different core sizes for the case when $V_o \rightarrow 0$ (but remains positive). In all calculations, $n_s/n_o$ and the polymer shell thickness were fixed at 24 and 9.4 nm, respectively, for the purposes of comparison.

particles can be expressed as

$$K_{mv,agg} = NK_{mv,ind}\frac{R_{shell}^2}{R_{agg}^2} \tag{5-30}$$

where $N$ is the number of individual particles with $K_{mv,ind}$ and $R_{shell}$ in aggregates of radius $R_{agg}$. The total static buildup volume for aggregates of different diameter was calculated as a function of the flow velocity and is shown in Figure 5-8. The static buildup volume is seen to increase with increasing aggregate diameter in a manner similar to individual particles. However, the transition velocity is approximately an order of magnitude lower than for individual particles, as the diffusion buildup limit depends on $K_{md,agg}$, which scales directly with the number of particles in the aggregates, while the drag force buildup limit depends on $K_{mv,agg}$, which increases at a much slower rate due to the $R_{shell}^2 / R_{agg}^2$ factor in Equation 5-30. The qualitative shapes of the aggregate buildups as

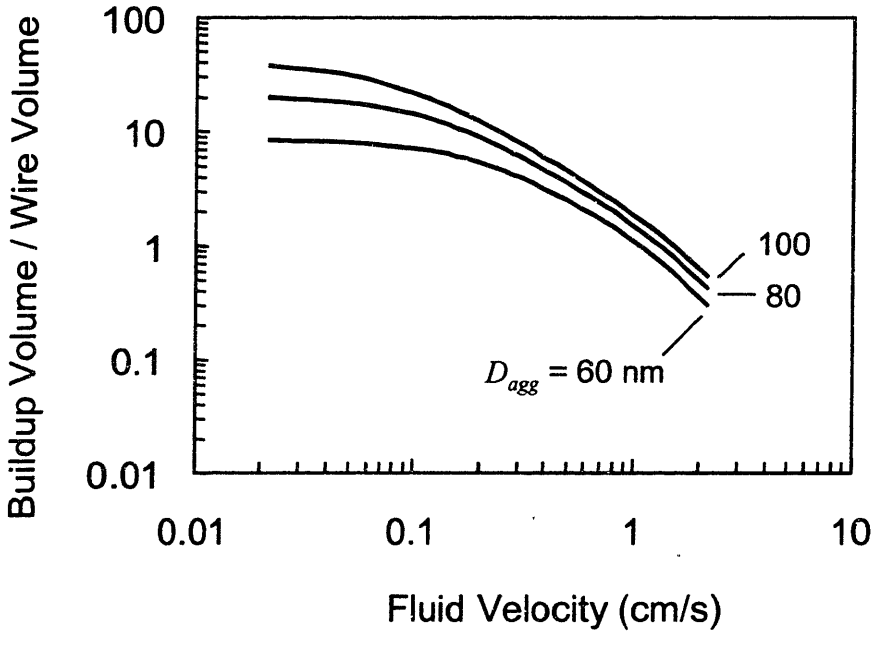


**Figure 5-8.** Effect of flow velocity on the static buildup volume of aggregates. The aggregates were assumed to be composed of average nanoparticles ($R_{core}$ = 3.75 nm and $R_{shell}$ = 13 nm) that maintained the same volume fraction of magnetite as the individuals. $n_s/n_o$ was fixed at 24.0 for the purposes of comparison.

$V_o \rightarrow 0$ are essentially the same as those for the individual nanoparticles shown in Figure 5-7b.

### 5.4.3 Magnetic Chromatography Results

To observe experimentally the effect of particle size on HGMS capture, we performed magnetic chromatography experiments in which a pulse of 0.5 wt% 16/0 magnetic fluid was injected into the column directly above the packing while water was passed continuously through the column. During the experiment, the column effluent was monitored for particle concentration and size. The flow velocity of the water (0.1 cm/s) was sufficiently low that diffusion was the primary mechanism opposing capture for all particles and aggregates. When this experiment was conducted with the magnet off, we observed a sharp breakthrough of particles in the column effluent with a mean residence time of 4.1 min and a small amount of variance due to axial dispersion or channeling. This breakthrough is shown in Figure 5-9 by the dashed line that represents particle concentration in the effluent as function of time.

The magnetic chromatography experiment was also performed with the magnet operated at its maximum field strength of 1.3 T; the results of this experiment are illustrated in Figure 5-9, which shows the particle concentration and hydrodynamic diameter from DLS of particles in the column effluent as a function of residence time. With the magnet on, the breakthrough of particles was only slightly delayed compared to when no field was applied, as the maximum effluent concentration occurred at only 1.6 residence times. The earliest particles to pass through the column had a number-average hydrodynamic diameter of only 10 nm, which is much smaller than the initial number-average diameter (26 nm). This result is consistent with our batch filtration data in Figure 5-3a, which showed that the smallest particles were the least attracted to the packing material. After the smallest particles were eluted, there followed a continuous decrease in particle concentration in the effluent over the next eight residence times, as average-sized particles that were significantly hindered by the magnetic field were washed from the column until the effluent was essentially free of particles. The magnet was then deactivated, at which point permanently trapped particles eluted from

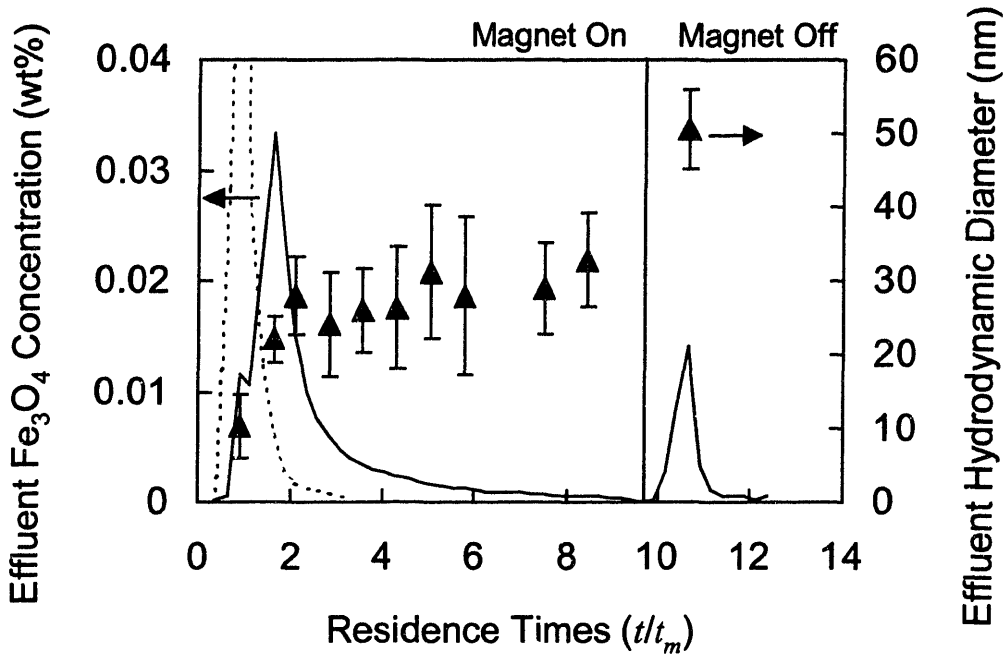


**Figure 5-9.** Magnetic chromatography of 16/0 magnetic fluid. In this experiment, 0.5 mL of 0.5 wt% 16/0 magnetic fluid was injected into the column directly above the packing material while water was passed continuously at 0.1 cm/s. The dashed line shows the concentration of particles in the effluent as a function of time (normalized by the mean residence time) when the magnet is off, while the solid line shows the concentration of particles in the effluent when the magnet is operated at its maximum field strength (1.3 T). The triangles represent the number-average hydrodynamic diameter of particles in the effluent during the run with the magnet on.

the column. Subsequent experiments showed that this peak was observed regardless of the time between injection and deactivation of the magnet. The number-average hydrodynamic diameter of the permanently trapped particles was 51 nm, which not only is much larger than the initial average, but also larger than any particles in the initial number-average distribution (Figure 2-9). These permanently trapped particles are probably the 60 to 125 nm aggregates present in the volume-average distribution from DLS. Further evidence that these permanently trapped particles are aggregates is that halving the concentration of the injected magnetic fluid halved the size of the permanently trapped peak, suggesting that these particles are not trapped in a limited number of sites on the packing material. The volume-average diameter of the permanently trapped particles was 94 nm, which is consistent with the size of the

aggregates. The smaller number-average diameter (51 nm) may be a result of some individual particles remaining with the aggregates and significantly biasing the number-average diameter. The fraction of particles that were permanently trapped (14% by volume) was consistent with the volume fraction of particles present as aggregates from DLS (11%), suggesting that we could permanently trap only the aggregates, while individual particles were merely hindered by the magnetized wires in the HGMS column.

Our inability to trap individual polymer-coated nanoparticles permanently is a limitation, as traditional HGMS requires permanent capture. The magnetic chromatography data suggest that the high capture efficiencies (~90%) observed for our batch HGMS filtrations (Figure 5-2) were probably an artifact of the low volumes passed through the column, in that many individual particles were merely retained in residual liquid inside the column instead of being permanently trapped on the wires. The calculated static buildup volumes shown in Figures 5-7 and 5-8 can explain the different behavior of individual particles and aggregates in the HGMS column. The smallest particles in the distribution (< 4.5 nm core diameter) cannot form a static buildup on the wires and so they are barely affected by the magnetic field, as we observed during magnetic chromatography. The average and larger sized individual particles do form a static buildup, but upstream water washes out the bulk liquid (outside of the buildup volume), resulting in a slow erosion of the particles due to the diffusion equilibrium. We hypothesize that permanent capture in the HGMS column can only occur if the limiting static buildup volume is sufficiently large that it occupies the entire void space in the column. In this case, any particle entering the column would be subjected to a magnetic force sufficient to overcome the dynamic equilibrium between particles trapped in the buildup volume and those in the outside fluid.

### 5.4.4 Comparison of Buildup with Void Space

Using the static buildup profiles from our model (Figures 5-7 and 5-8), we computed the individual particle and aggregate size at which the buildup volume becomes sufficiently large to occupy the entire void space in the column. Figure 5-10 illustrates the static buildup volume for both individual particles and aggregates in a

purely diffusion-limited case ($V_o \rightarrow 0$). Note that for individual particles we plot against the core diameter because in the diffusion limit, the buildup volume is essentially independent of the shell thickness. The buildup volume of the aggregates increases more slowly with diameter because they are less than 3 vol% magnetite due to the large polymer shell around the particles. In Figure 5-10, the void volume is represented as the horizontal dashed line, which was calculated from the 13.7 vol% packing fraction. In calculating the void volume, we accounted for the fact that the wire orientation in the HGMS column is essentially random in the plane perpendicular to the flow direction by assuming that approximately half of the wires are oriented parallel to the applied field,

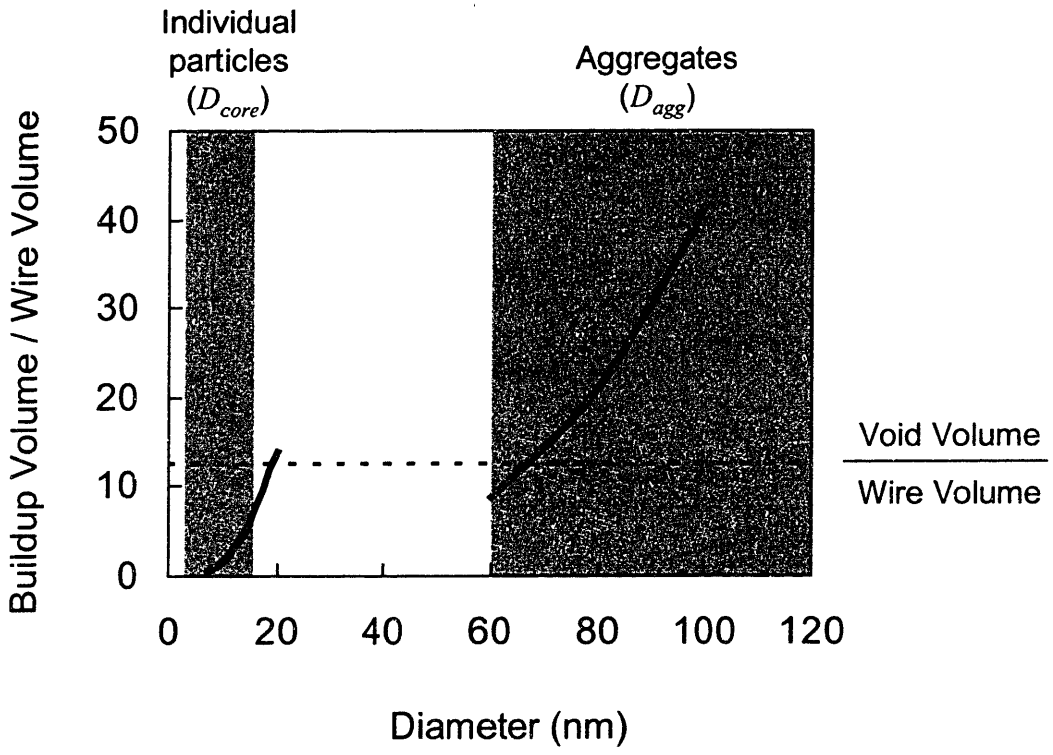


**Figure 5-10.** The static buildup volume of individual polymer-coated nanoparticles and particle aggregates compared to the void volume of the column. The solid lines represent the calculated limit of static nanoparticle buildup as $V_o \rightarrow 0$ (representative of the conditions used in our magnetic chromatography experiments) for individual particles of varying core diameter ($D_{core}$) and aggregates of varying total diameter ($D_{agg}$). The shaded regions represent the measured size range of the individual particles and the aggregates. The dashed line shows the void volume of the column. Permanent capture of particles or aggregates should occur when the static buildup volume of the particles around the wires exceeds the void volume of the column.

inducing no magnetic field gradients in the liquid as discussed in the theoretical development. Considering these wires as equivalent to dead space, the volume fraction of active wires (with the geometry shown in Figure 5-1) is closer to 6.9 vol%, which results in a normalized void volume of 12.6. All of the individual nanoparticles ($3 < D_{core} < 15$ nm) have a static buildup volume that occupies less than the void volume, so they should eventually be washed from the column by upstream liquid. The buildup volume of the aggregates, however, occupies all of the void space when the diameter exceeds ~70 nm. Since the aggregates seen from dynamic light scattering are 60-125 nm in diameter, the theory is consistent with our experimental observations of permanent aggregate capture during magnetic chromatography.

### 5.4.5 Comments on Capture of Individual Nanoparticles

For permanent capture of the individual nanoparticles in our HGMS column to be feasible, the particles would require a larger diffusion-limited buildup volume, determined by the value of $K_{md}$. Equation 5-27 shows that for a particle with a given core radius, the only practical methods for increasing this ratio are by increasing the magnetization of the packing material or particle core. As shown in Figure 2-8, at the applied field strength of 1.3 T used in our experiments, the particles are magnetically saturated, meaning that increases in the applied magnetic field will not increase $M_{core}$. Likewise, the stainless steel packing is saturated at 1.3 T,[1] and HGMS performance cannot be improved by further increases in the applied field.[6] One possibility would be to use cobalt nanoparticles (or wires) in the process, as cobalt has a higher magnetization; however, cobalt is less stable to oxidation and more costly than magnetite and stainless steel. Another strategy would be to increase the volume fraction of "active" wires in the column by using a structured packing.

## 5.5 Comparison with Phospholipid-Coated Particles

Magnetite nanoparticles coated with a surfactant-phospholipid bilayer and able to bind proteins selectively based on electrostatic charge have been discussed recently.[10] In contrast to the polymer-coated particles discussed above, the phospholipid-coated nanoparticles were successfully captured in preliminary bench scale studies.[10] To explain

why these particles were more easily captured, we applied our magnetic filtration theory to the results from a series of magnetic chromatography experiments at different flow velocities performed by Bucak et al.[10] The core size distribution and magnetization response of these phospholipid-coated particles were essentially identical to those of our polymer-coated nanoparticles that have been the focus of this thesis. The surfactant-phospholipid bilayer should form a 4 nm thick layer on the surface, but DLS results showed that these nanoparticles exist as small aggregates in the 25-50 nm size range, with a number-average diameter of 32 nm.[10] We estimate that an average aggregate would consist of approximately nine individual particles if the magnetite volume fraction in the aggregate is the same as for individual particles. Roughly 1-2 wt% of the particles exists as much larger aggregates and can be ignored for our purposes.[10]

Figure 5-11a shows the results of a magnetic chromatography experiment in which a pulse of the phospholipid magnetic fluid (1.36 wt% $Fe_3O_4$) was injected into the column while water was passed at three different velocities. In contrast to the polymer-coated nanoparticles, the majority of particles were permanently trapped in all cases regardless of the flow velocity. This result suggests that HGMS can be applied successfully to these particles after removing the small fraction that cannot be captured.[10] The fraction of escaping particles increased as the flow velocity increased, as shown in Figure 5-11b. The transition velocity between the diffusion- and fluid drag force-controlled regimes is predicted theoretically in Figure 5-12, which shows the limit of static buildup for the three different velocities. These profiles were calculated from Equations 5-24 and 5-25 assuming the nanoparticles were present as dense 32 nm diameter aggregates of particles with a 7.5 nm magnetite core and a 15.5 nm total shell diameter (that maintain the same volume fraction of magnetite as the individual particles). All other parameter values were identical to those used in the polymer-coated particle calculations, except $n_s/n_o$, which was calculated to be 22.5 for these aggregates at the initial concentration.

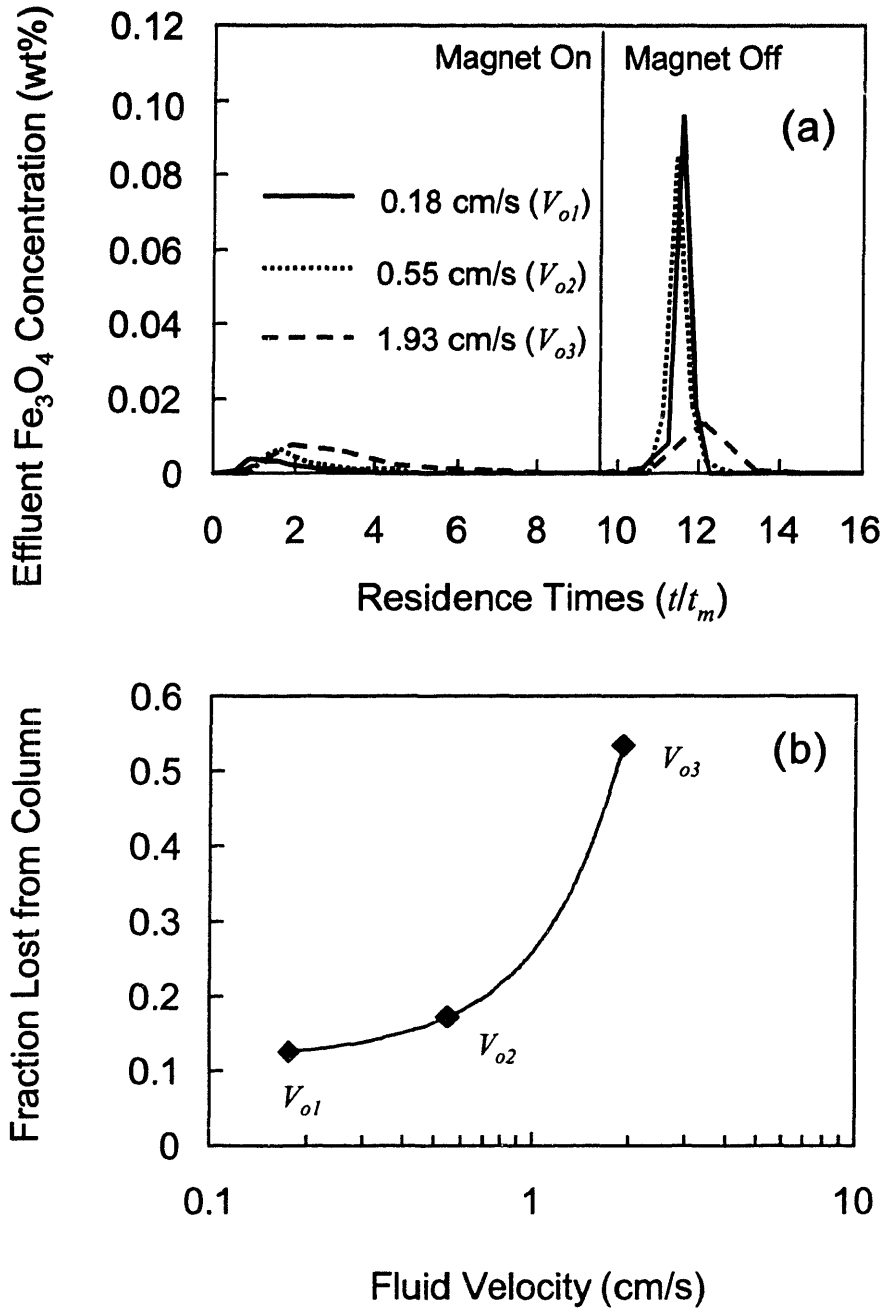


**Figure 5-11.** (a) Magnetic chromatography of the phospholipid-coated magnetic nanoparticles. In this experiment, 0.5 mL of 1.36 wt% magnetic fluid was injected into the column directly above the packing material while water was passed continuously at various flow velocities. The lines represent the concentration of particles in the effluent as a function of time (normalized by the mean residence time). (b) The calculated fraction of particles lost from the column.

Figure 5-12 shows that the three velocities used in the magnetic chromatography experiment were all conducted in the fluid drag force-limited regime. As expected, the drag force buildup limit increases in volume as the velocity decreases. This trend is consistent with the magnetic chromatography results in Figure 5-11 that show an increase in the fraction of particles lost from the column from $V_{o1}$ to $V_{o2}$ (13% to 17%) and again from $V_{o2}$ to $V_{o3}$ (17% to 53%). Figure 5-12 shows that the transition velocity below which HGMS of the phospholipid-coated particles becomes diffusion-controlled is close to $V_{o1}$ (0.18 cm/s), as the drag force buildup limit has nearly reached the diffusion limit, suggesting that there would be little further benefit of reducing the velocity below 0.18 cm/s.

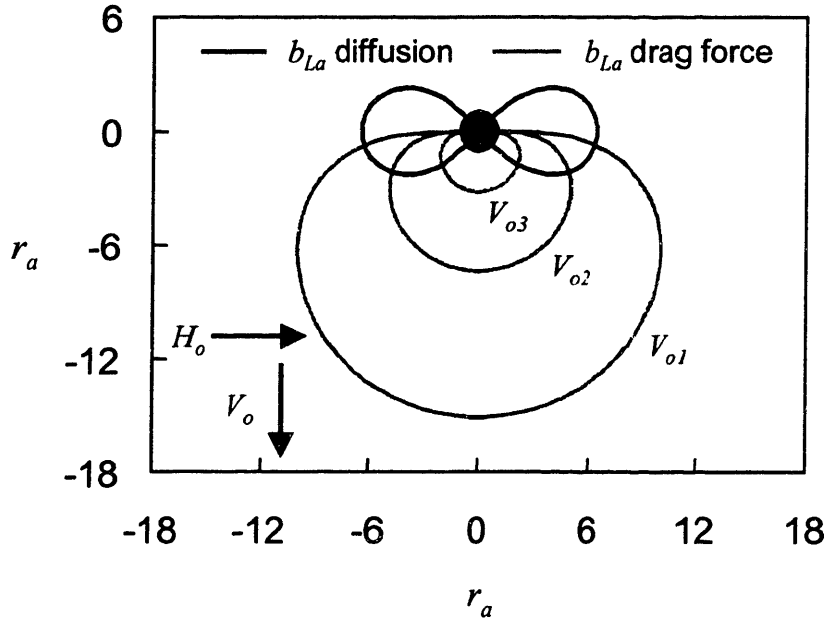


**Figure 5-12.** Predicted diffusion (black line) and drag force (gray line) limits of static buildup for the phospholipid-coated nanoparticle aggregates. The actual limit of static buildup at a given flow velocity is defined by the area inside both curves.

In the diffusion-controlled regime, the effect of particle size on capture is determined purely by the diffusion buildup limit. Using the assumption that $V_o \rightarrow 0$, the volume of the limit of particle buildup for phospholipid-coated aggregates of varying total diameter is shown in Figure 5-13. The void volume of the column is also shown in this figure as a horizontal line. The aggregate buildup volume exceeds the total void

space in the column (indicative of permanent capture) when the aggregate diameter exceeds approximately 40 nm. DLS showed that these aggregates span a range from 25-50 nm in diameter,[10] which explains why some aggregates are permanently captured while others are lost from the column. Our theoretical prediction of the minimum aggregate diameter for permanent capture (40 nm) is likely too high, as magnetic chromatography experiments (Figure 5-11b) showed that only 13% of the particles were lost from the filter at a low flow velocity, which DLS results suggest should occur if the cutoff diameter was 28 nm (i.e. 13% of the aggregates are less than 28 nm in diameter).[10] Our overprediction of the minimum aggregate diameter for capture could be a result of the aggregate being more densely packed than we assumed, which could occur if the phospholipid layer coated an aggregate instead of individual particles.

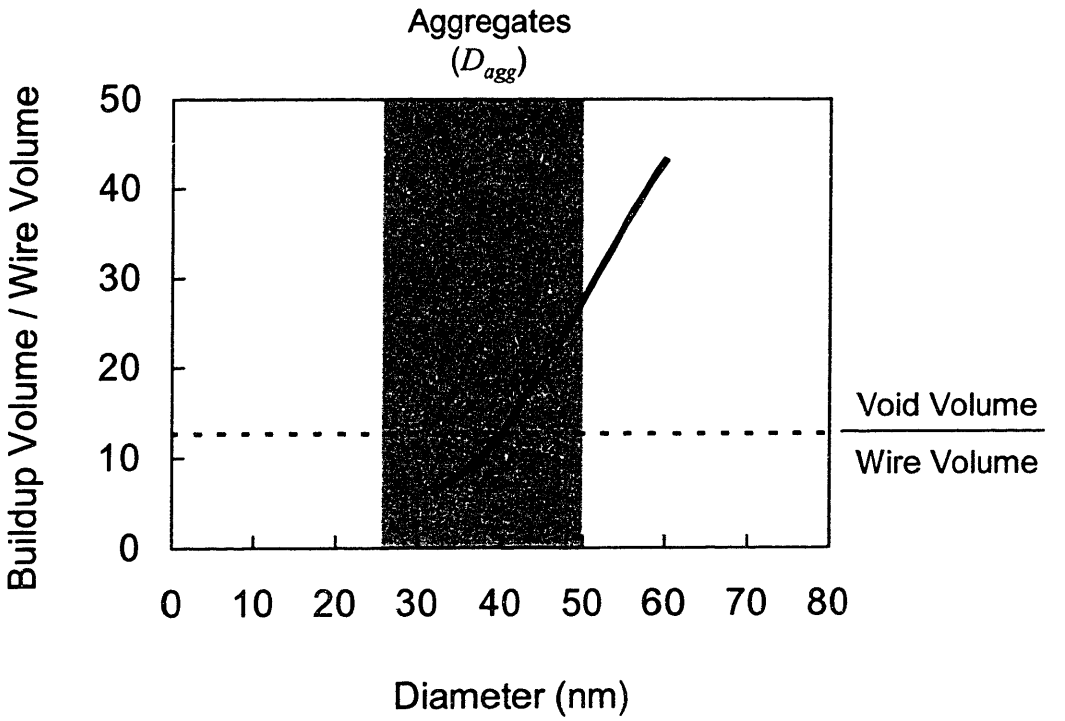


**Figure 5-13.** The static buildup volume of the phospholipid-coated particle aggregates compared to the void volume of the column. The solid line represents the calculated limit of static nanoparticle buildup as $V_o \rightarrow 0$ for aggregates of varying total diameter ($D_{agg}$), while the shaded region represents the measured size range of the aggregates. The dashed line shows the void volume of the column.

## 5.6 Aggregate Formation: A Preliminary Study

Experimental results and our model for particle buildup have indicated that small nanoparticle aggregates can be captured permanently in the HGMS column. The predicted minimum aggregate diameter for capture depended on the magnetite volume fraction in the aggregates and was estimated to be ~70 nm for our graft copolymer-coated magnetic fluids for organic separation. To increase the fraction of aggregates in these magnetic fluids, we attempted to form aggregates by performing the magnetite precipitation reaction in a mixture of our usual 16/0 graft copolymer and high molecular weight polyacrylic acid (PAA). The graft copolymer should bind to the particles just after nucleation and limit the size to ~10 nm, as it did in our usual magnetic fluids. The high molecular weight PAA also contains carboxylic acid groups and should bind to available sites on multiple particles, thereby forming crosslinks that should result in small aggregates. We varied the molecular weight and concentration of the PAA homopolymer but kept the 16/0 graft copolymer:magnetite mass ratio fixed at 1.25 throughout all experiments.

Dynamic light scattering was used to measure the hydrodynamic size of the aggregated magnetic fluids after synthesis. As with our original magnetic fluids, we observed a bimodal size distribution, but the size of the particles in both peaks was shifted to larger diameters when high molecular weight PAA was present. The dynamic light scattering results are summarized in Figure 5-14, which shows the weight-average hydrodynamic radius of the particles when PAA is added during the precipitation. In this figure, the weight-average diameter is plotted because we are interested in the size and relative amount of aggregates present. The data at zero added PAA represent our original 16/0 magnetic fluid, which had a weight-average diameter of 39 nm. The addition of PAA with a molecular weight of 100,000 g/mol resulted in a slight increase in the weight-average diameter to 65 nm when 0.2 g PAA/g $Fe_3O_4$ was added. Adding additional PAA did not significantly increase the diameter from this value. Adding PAA with a molecular weight of 250,000 g/mol resulted in a much larger increase in size, with the weight-average diameter increasing to 159 nm when 0.2 g PAA/g $Fe_3O_4$ was added. Similarly, there did not appear to be a strong effect of the amount of the PAA on the final

size. In both cases, it is uncertain whether the observed increase in size was due to crosslinking of particles or attachment of long PAA chains to single particles. Attaching PAA to individual particles should not significantly affect the HGMS collection efficiency in the diffusion-controlled regime.

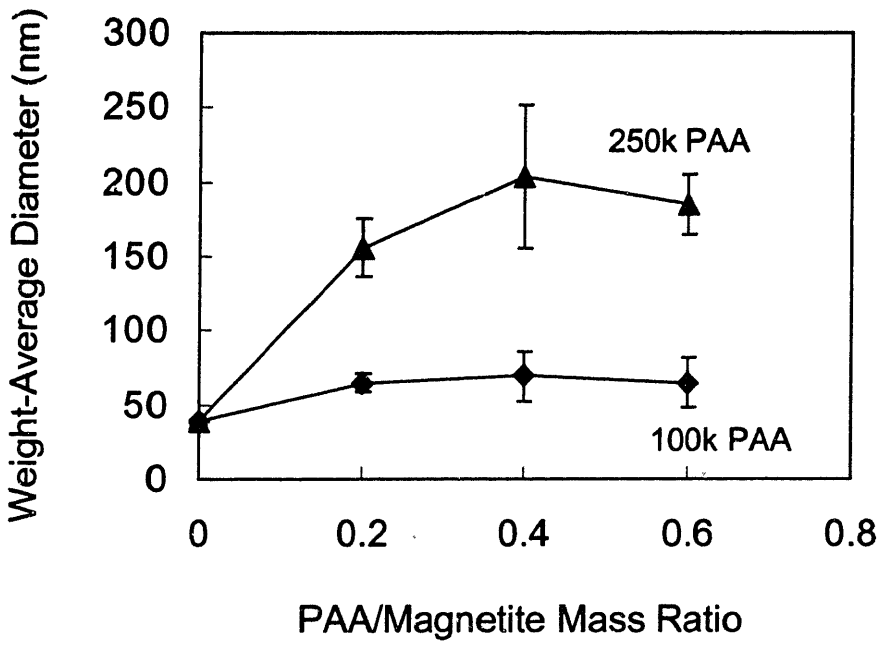


**Figure 5-14.** Weight-average hydrodynamic diameter of aggregated 16/0 magnetic fluids. Adding PAA during the synthesis increases the average size of the particles relative to the value of 39 nm for the original 16/0 magnetic fluids (i.e. zero added PAA). The final size is more strongly dependent on the molecular weight than on the amount of PAA.

We performed magnetic chromatography experiments on the aggregated 16/0 magnetic fluids to determine whether they were easier to capture in the HGMS column. Figure 5-15 shows the results of magnetic chromatography experiments with the original 16/0 magnetic fluid (no PAA), as well as magnetic fluids with 100,000 and 250,000 molecular weight PAA (0.2 g PAA/g $Fe_3O_4$). The flow velocity of the water in these experiments (0.1 cm/s) was sufficiently low that HGMS was diffusion-controlled. In all the runs, the magnet was on (at a maximum applied field of 1.3 T) when the magnetic

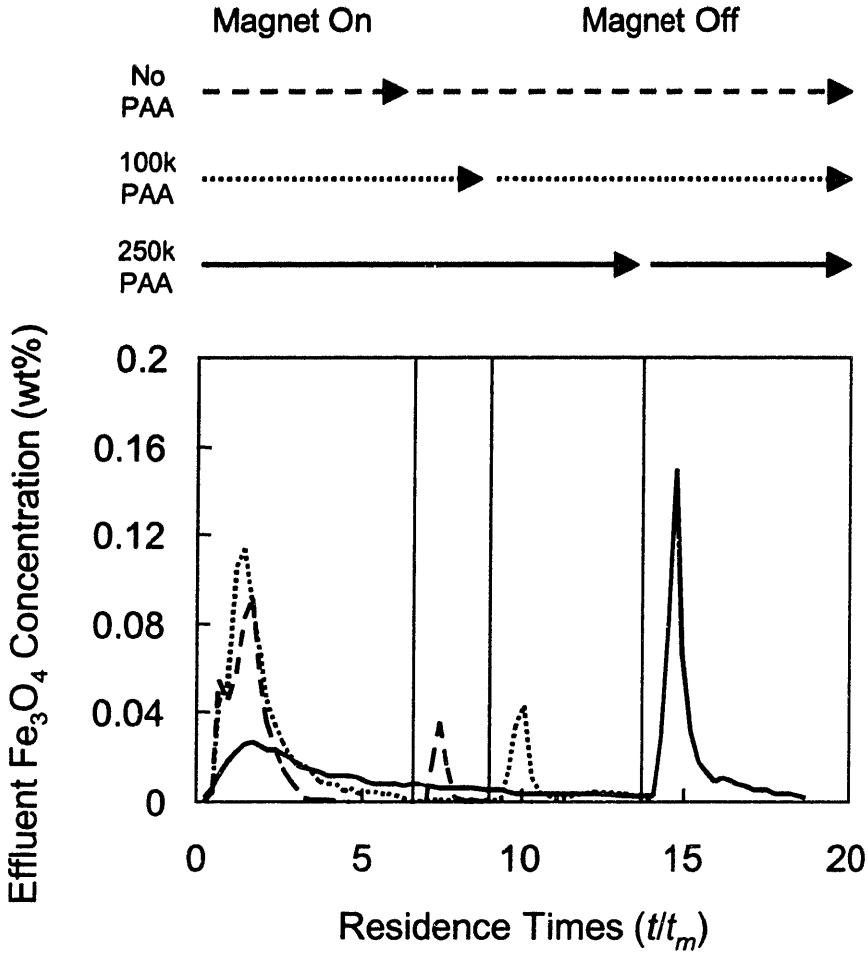


**Figure 5-15.** Magnetic chromatography of aggregated 16/0 magnetic fluids. In this experiment, 0.5 mL of 0.5 wt% magnetic fluid was injected into the column directly above the packing material while water was passed continuously at 0.1 cm/s. Data are shown for the original 16/0 magnetic fluid (dashed line), aggregated magnetic fluid with 100,000 molecular weight PAA at 0.2 g/g $Fe_3O_4$ (dotted line), and aggregated magnetic fluid with 250,000 molecular weight PAA at 0.2 g/g $Fe_3O_4$ (solid line). The arrows above the plot illustrate when the magnet was activated and deactivated.

fluid was injected at the start of the experiment and was deactivated when the particle concentration in the effluent reached essentially zero. The vertical lines in this figure represent the point at which the magnet was deactivated, which differed for the various magnetic fluids. These results show that all three magnetic fluids were significantly hindered in their flow through the HGMS column, as the particles took longer to elute than when no field was applied. Data for the run with the magnet off are not shown for clarity, but are characterized by a sharp peak centered at one residence time. The

addition of 100,000 molecular weight PAA during synthesis had only a small effect on the elution of particles in the column, as the particles required approximately three additional residence times to fully elute. In addition, the weight fraction of permanently trapped particles that eluted from the column only when the magnet was deactivated increased from 0.10 to 0.17. The addition of 250,000 molecular weight PAA during synthesis had a much greater effect on HGMS, in that the concentration of particles that escaped with the magnet on was reduced by a factor of approximately two. There was also a much longer elution tail that took approximately fourteen residence times before particles were no longer visibly detectable in the effluent. The weight fraction of permanently trapped particles was increased to 0.52, suggesting substantial aggregation in the magnetic fluid.

Using dynamic light scattering, we measured the size of both the particles that escaped the HGMS filter with the magnet activated and the permanently trapped particles. Size measurements of the lost and trapped particles were made on samples that eluted at the maximum concentration (i.e. approximately 1.5 residence for the particles that escaped the filter) and are shown in Table 5-1. Magnetic chromatography results are also summarized for magnetic fluids produced with PAA of both molecular weights at a higher concentration of PAA (0.4 g PAA/g $Fe_3O_4$). The addition of crosslinking PAA appeared to have no effect on the size of particles that escaped the filter, which did not change significantly from the value of 21 nm that we measured for the original 16/0 particles. This result suggests that even with the addition of PAA, many particles were completely coated by the 16/0 graft copolymer before the PAA could crosslink the particles. Table 5-1 also shows that the HGMS response of the particles is much more sensitive to the molecular weight of of the PAA than the concentration, as doubling the concentration of 100,000 molecular weight PAA during synthesis actually reduced the fraction of permanently trapped particles. A similar result was observed for the 250,000 molecular weight PAA, in that doubling the amount of PAA had no effect on HGMS collection efficiency. In general, the 100,000 molecular weight PAA was not an effective crosslinker, as it had little effect on HGMS capture, although it did increase slightly the hydrodynamic size of the trapped particles. This result suggests that it did bind to some of the particles but was not sufficiently long to bridge multiple particles. During the

particle synthesis at high pH, the PAA is ionized and the ionic strength of the solution is high. Under these conditions, the radius of gyration is estimated to be 14 and 24 nm for the 100,000 and 250,000 molecular weight PAA, respectively,[17] while the thickness of the 16/0 graft copolymer shell was estimated to be 9.4 nm (Section 2.3.5). We hypothesize that because of its smaller size and higher concentration, the graft copolymer probably coats the nanoparticles rapidly, while the larger PAA binds to available sites afterwards. In order to bridge two particles, the radius of gyration of the PAA must therefore be significantly larger than the shell thickness, as is the case for the 250,000 molecular weight PAA.

**Table 5-1.** HGMS results for aggregated 16/0 magnetic fluids

| PAA/Magnetite Mass Ratio | $M_w$ PAA (g/mol) | Diameter[a] of Lost Particles (nm) | Diameter[b] of Trapped Particles (nm) | Weight Fraction Trapped Permanently |
|---|---|---|---|---|
| - | - | 21 | 51 | 0.11 |
| 0.2 | 100k | 29 | 67 | 0.17 |
| 0.4 | 100k | 22 | 85 | 0.10 |
| 0.2 | 250k | 17 | 172 | 0.52 |
| 0.4 | 250k | 17 | 124 | 0.54 |

a) The number-average hydrodynamic diameter of the particles at the maximum effluent concentration with the magnet activated.
b) The number-average hydrodynamic diameter of the particles at the maximum effluent concentration with the magnet deactivated.

## 5.7 Summary

We have examined the feasibility of using high gradient magnetic separation to remove magnetic nanoparticles from water. We examined both our polymer-coated magnetic nanoparticles for organic removal from water and phospholipid-coated particles for protein separation. These tailored nanoparticles have potential advantages over traditional methods of organic removal due to their small particle size.[10,15]

Our magnetic fluids for the removal of organic compounds from water consisted of a magnetite core of 7.5 nm median diameter surrounded by a hydrated polymer coating

of 9.4 nm thickness; a small fraction (11-14%) of the particles was present as 60-125 nm aggregates. We observed that small volumes of these magnetic fluids could be passed through the HGMS column with ~90% recovery. Most of the particles that were lost were the smallest particles in the distribution, and after removing these, the particle recovery increased to approximately 98% for small volumes of magnetic fluid. However, the small volumes of magnetic fluid used in the batch filtration experiments probably biased these results, as magnetic chromatography experiments indicated that the individual nanoparticles in these magnetic fluids could not be trapped permanently by HGMS, even at a low flow velocity, while the aggregates could be captured permanently. Permanent capture is important, as a practical separation process would have to filter many column volumes of magnetic fluid before the HGMS column was regenerated.

HGMS was much more successful at capturing the phospholipid-coated particles synthesized by Bucak et al,[10] which consisted of 7.5 nm magnetite particles that form 25-50 nm aggregates. Approximately 87% of these aggregates were permanently trapped when the liquid was passed at a low flow velocity. After removing the small fraction that was not permanently captured by the magnet, the remaining aggregates could be captured effectively and would be suitable for use with HGMS.

We developed a theory, based on a development by Fletcher[5] with several modifications, that described the static buildup of nanoparticles around the collection wires in our HGMS column. This theory showed that magnetic filtration can be divided into two regimes: a high flow velocity regime in which fluid drag is the primary force opposing capture and a low flow velocity regime in which diffusion primarily acts against particle capture. The transition velocity between these two regimes has been determined theoretically and experimentally for our nanoparticles, with good agreement between theory and experiment. The model can also be used to give a theoretical estimate of the minimum particle size for permanent capture. We showed that individual $Fe_3O_4$ nanoparticles with a core diameter less than 20 nm could not be permanently captured in our HGMS column. Aggregates could be captured permanently because the entire void space of the column is inside the limit of static buildup around a collection wire. The minimum aggregate size for permanent capture was calculated to be 40 nm for

the phospholipid-coated particles and 70 nm for our polymer-coated nanoparticles for organic separation; this difference is due to the higher volume fraction of magnetite in the phospholipid aggregates.

In a preliminary attempt to improve the HGMS capture efficiency of the graft copolymer-coated nanoparticles, we incorporated bridging polyacrylic acid chains during synthesis to link particles together, thereby forming small aggregates that maintain a relatively high surface area for separation. Our results showed that the molecular weight of the polyacrylic acid was a key parameter that determined the size of the aggregates. Using polyacrylic acid with a molecular weight of 250,000 g/mol resulted in approximately 50% of the particles being present as 124-172 nm aggregates that could be captured permanently in the HGMS column. Aggregation of the particles resulted in a substantial increase in the fraction of particles that could be captured permanently, which was only 10% for the original 16/0 particles.

## 5.8 Bibliography


(1) Gerber, R.; Birss, R. R. *High Gradient Magnetic Separation*; Research Studies Press: London, United Kingdom, 1983.

(2) Hubbuch, J. J.; Thomas, O. R. T. High-Gradient Magnetic Affinity Separation of Trypsin from Porcine Pancreatin. *Biotechnol. Bioeng.* **2002**, *79*, 301-313.

(3) Leun, D.; Sengupta, A. K. Preparation and Characterization of Magnetically Active Polymeric Particles (MAPPs) for Complex Environmental Separations. *Environ. Sci. Technol.* **2000**, *34*, 3276-3282.

(4) Gerber, R.; Takayasu, M.; Friedlaender, F. J. Generalization of HGMS Theory: The Capture of Ultra-fine Particles. *IEEE Trans. Magn.* **1983**, *19*, 2115-2117.

(5) Fletcher, D. Fine Particle High Gradient Magnetic Entrapment. *IEEE Trans. Magn.* **1991**, *27*, 3655-3677.

(6) Takayasu, M.; Gerber, R.; Friedlaender, F. J. Magnetic Separation of Submicron Particles. *IEEE Trans. Magn.* **1983**, *19*, 2112-2114.

(7) Ebner, A. D.; Ritter, J. A.; Ploehn, H. J. Feasibility and Limitations of Nanolevel High Gradient Magnetic Separation. *Sep. Purif. Technol.* **1997**, *11*, 199-210.

(8) Cotten, G. B.; Eldredge, H. B. Nanolevel Magnetic Separation Model Considering Flow Limitations. *Sep. Sci. Technol.* **2002**, *37*, 3755-3779.

(9) Moyer, C.; Natenapit, M.; Arajs, S. Magnetic Filtration of Particles in Laminar-Flow through a Bed of Spheres. *J. Magn. Magn. Mater.* **1984**, *44*, 99-104.

(10) Bucak, S.; Jones, D. J.; Laibinis, P. E.; Hatton, T. A. Protein Separations using Colloidal Magnetic Nanoparticles. *Biotechnol. Prog.* **2003**, *19*, 477-484.

(11) Yoe, J. H.; Jones, L. Colorimetric Determination of Iron with Disodium-1,2-dihydroxybenzene-3,5-disulfonate. *Ind. Eng. Chem.* **1944**, *16*, 111-115.

(12) Ebner, A. D.; Ritter, J. A. New Correlation for the Capture Cross Section in High-Gradient Magnetic Separation. *AIChE J.* **2001**, *47*, 303-313.

(13) Ying, T. Y.; Yiacoumi, S.; Tsouris, C. High-Gradient Magnetically Seeded Filtration. *Chem. Eng. Sci.* **2000**, *55*, 1101-1113.

(14) Wangsness, R. K. *Electromagnetic Fields*; John Wiley and Sons: New York, NY, 1979.

(15) Moeser, G. D.; Roach, K. A.; Green, W. H.; Laibinis, P. E.; Hatton, T. A. Water-Based Magnetic Fluids as Extractants for Synthetic Organic Compounds. *Ind. Eng. Chem. Res.* **2002**, *41*, 4739-4749.

(16) Rosensweig, R. E. *Ferrohydrodynamics*; Dover Publications, Inc.: Mineola, NY, 1985.

(17) Reith, D.; Muller, B.; Muller-Plathe, F.; Wiegand, S. How Does the Chain Extension of Poly (Acrylic Acid) Scale in Aqueous Solution? A Combined Study with Light Scattering and Computer Simulation. *J. Chem. Phys.* **2002**, *116*, 9100-9106.

# Chapter 6

# Conclusions

## 6.1 Summary of Research

Magnetic fluids are colloidal dispersions of magnetic nanoparticles that are stable to sedimentation because of their small size. In this work, we have developed and characterized a novel class of water-based magnetic fluids for the removal of organic compounds from water. Because of their nanometer size, these materials possess a very large surface area for separation. Unlike activated carbon beads, which are currently the most widely used materials for organic separation, their large surface area is achieved without the incorporation of porous structures that introduce a high mass transfer resistance.

These magnetic fluids consist of an aqueous suspension of ~7.5 nm diameter magnetic $Fe_3O_4$ nanoparticles produced through the chemical coprecipitation of iron salts in aqueous solution in the presence of a PEO/PPO-PAA graft copolymer. The particles were coated with a ~9.4 nm bifunctional polymer layer comprised of an outer hydrophilic PEO region that stabilizes the particles against agglomeration and an inner hydrophobic PPO region that provides a favorable environment for organic extraction. The hydrophobicity of the polymer coating on the particles was controlled by selection of the PEO:PPO content of the graft copolymer. The magnetite core of the particles had a magnetization similar to that of bulk magnetite, suggesting the particles are good candidates for magnetic separation. In addition, these magnetic fluids were stable over a broad range of temperature, ionic strength, and pH, and so they should not flocculate even under relatively harsh process conditions.

To validate our conceptual model for the polymer shell, which consisted of an inner hydrophobic region and an outer hydrophilic region, we conducted neutron scattering experiments that were compared to the results of lattice calculations performed by Per Linse (University of Lund, Sweden). This analysis yielded the hydration structure

of the polymer shell, which suggested that the inner region of the polymer shell is similar in structure to that of compositionally similar Pluronic micelles that have been studied as organic separation agents. The interior region of the PPO-rich nanoparticle shells contains more PEO than the core of a Pluronic micelle, as the side chains are more constrained in the nanoparticles, but the amount of water is similar.

The comparison of our magnetic fluids with Pluronic micellar solutions was extended in a series of extraction experiments that measured the uptake of model organics into the polymer shell. Only when PPO side chains were present (which formed a hydrophobic domain or region) were organics solubilized in the polymer shell. We measured the solubility of substituted benzenes, polyaromatic hydrocarbons, and linear alkanes in the polymer shell. While the partition coefficient of the organics between the PPO and water was on the order of $10^3$ and $10^5$ for all of the organics, the particles were more selective for smaller aromatic species. Using a linear free energy relationship, the solubility trends were shown to be similar to data for Pluronic micelles, for which extensive solubility data already exist. We also observed the uptake of more dilute organics using fluorescence. These experiments showed that the magnetic fluids developed in this work seem promising as potential extractants for organic compounds in water.

Given the strong organic affinity of the particles, we conducted bench scale-high gradient magnetic separation (HGMS) experiments to analyze the feasibility of this process to remove nanoparticles form water. Results from these experiments were compared to predictions from a model that we developed for nanoparticle buildup around the collection wires in an HGMS column. Both our model and experiments showed that magnetic filtration of the nanoparticles could be divided into two regimes: a high flow velocity regime in which fluid drag is the primary force opposing capture and a low flow velocity regime in which diffusion primarily acts against particle capture. In addition, we observed that even when the liquid was passed at a low flow velocity, the individual nanoparticles in these magnetic fluids could not be trapped permanently by HGMS, unlike the ~10% of particles that were present as 60-125 nm aggregates that could be captured permanently. Our model indicated that the inability of our HGMS column to

capture individual particles was due to diffusion of the particles away from the wires. The model for nanoparticle buildup predicts that individual particles with a $Fe_3O_4$ core diameter of less than 20 nm cannot be captured permanently in our HGMS column at any flow velocity. Modification of the nanoparticles is therefore required before they could be applied in a practical separation process. Preliminary results showed that by incorporating bridging polymer chains during synthesis to link particles together, the fraction of permanently trapped particles could be increased from approximately 10% to 50%. This is closer to the HGMS performance of phospholipid-coated magnetite nanoparticles that have been used for protein separations, in which approximately 90% of the particles are captured permanently.[1]

## 6.2 Process Considerations

The fraction of particles captured permanently by HGMS would have to be increased substantially before the particles could be used for water purification, as the residual particle concentration would have to be at least below the visible detection threshold. Permanent capture of 100% of the synthesized particles is not required, however, as a preliminary fractionation step similar to our magnetic chromatography experiments could be performed to remove particles that escape the HGMS filter.[1] The discarded fraction would have to be improved from its current best-case value of approximately 50% (for the aggregated particles) before the particles could be considered as a feasible alternative to other water purification processes.

Provided that particle capture by HGMS could be improved, these magnetic fluids could be integrated into a water purification process involving intimate contacting of the nanoparticles with a contaminated water stream and the magnetic recovery of these particles, followed by their regeneration or disposal. In the contacting phase, a concentrated suspension of the $Fe_3O_4$ particles would be added to a contaminated water source, as shown in Figure 6-1. Due to their small size, the particles would disperse rapidly in the feed phase and absorb organics in their hydrophobic shells with minimal diffusional resistance. The organic-loaded particles would then be passed through the HGMS column, where the particles would be trapped, allowing purified water to exit the

filter. Depending on the dictates of process economics, the loaded particles would either be removed from the filter by deactivating the magnetic field and flushing with clear water for subsequent disposal by incineration or landfill, or they could be regenerated within the magnetic filter by, for example, steam stripping or solvent extraction. The regenerated particles could then be recycled to treat a fresh contaminated feed stream.

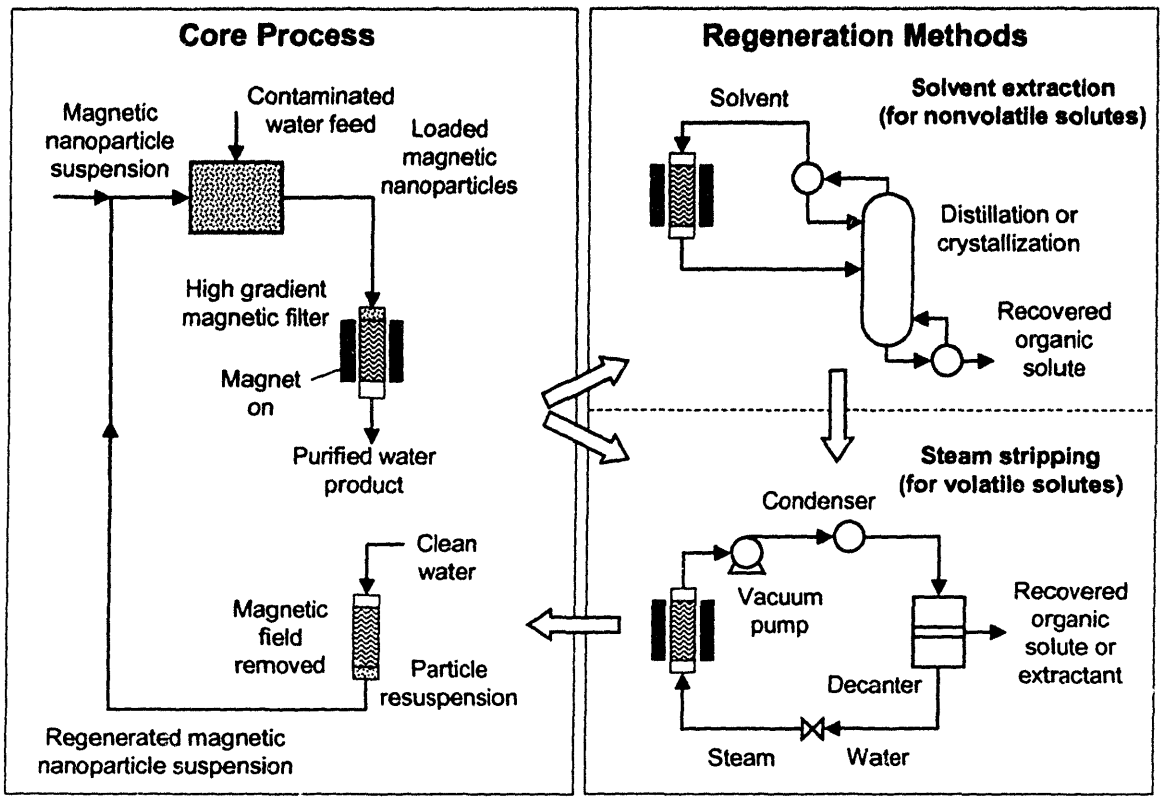


**Figure 6-1.** Integration of magnetic nanoparticles in a process to extract organic contaminants from water. After contacting the particles with a contaminated water stream, the loaded particles are removed with HGMS (left panel). When the magnetic filter is saturated with particles, the particles can be regenerated in the filter by steam stripping any volatile organics from the particles (lower right panel). If the absorbed organics are non-volatile, they can be removed by solvent extraction with a low molecular weight solvent (upper right panel) followed by steam stripping of the solvent (lower right panel). After regeneration, the particles are flushed from the filter with the magnet off to obtain a concentrated particle suspension that is recycled (left panel).

A possible process for the regeneration and recycle of the magnetic nanoparticles with recovery of the extracted organics is shown in the right panel of Figure 6-1. Solubilized organics that are volatile or semi-volatile could be removed from the trapped

particles by steam stripping.[2,3] Condensation of the collected vapor would produce a two-phase system of water, which could be recycled, and the organic, which could be removed by decantation or filtration. On completion of the steam stripping process, the magnet would be turned off and the particles resuspended in a nall volume of water to produce a regenerated magnetic fluid for recycle to the contacting phase. Heavy organics such as PCB that would be difficult to remove by steam stripping could be removed by solvent extraction in the HGMS column with a compatible low molecular weight solvent such as toluene. We have essentially demonstrated the feasibility of this latter process in our organic extraction experiments, in which organics were removed from the polymer shell by back-extraction into hexane. The heavy organics would be removed from the solvent by distillation or crystallization, and the solvent recycled. This process would saturate the polymer shell with the solvent, so steam stripping would subsequently be required to regenerate the particles before they could be recycled. Regardless of the regeneration method, the high concentration of organics in the nanoparticles would ensure low processing volumes during regeneration relative to those needed to treat the original volume of contaminated water.

The process illustrated in Figure 6-1 has several potential advantages over more traditional methods of organic removal. Our particles disperse readily in the contaminated water stream due to their nanoscale dimensions, and they can potentially be recovered by magnetic filtration. These magnetic fluids preconcentrate the organics, which allows techniques like solvent extraction and steam stripping to be applied more efficiently to much smaller volumes of material than if they were to be applied to the original feed phase. For example, with the process in Figure 6-1, the problems of phase disengagement and countercontamination of the feed with solvent are avoided. Moreover, the colloidal dispersion of nanoparticles in the feed phase is essentially a one-phase system, which can offer fluid handling advantages over conventional solvent extraction processes, in which one phase is distributed as a coarse dispersion in the other, and which can be plagued by flow maldistribution and channeling problems. In addition, the volume of steam required for steam stripping of the nanoparticles is much less than the original feed would require. Our nanoparticles also have potential advantages over adsorption techniques like activated carbon, in that they provide an extremely large

surface area of the polymer shell without the porous structures characteristic of activated carbon beads, which inherently have a high mass transfer resistance. This advantage allows for more rapid processing of contaminated streams. As an HGMS column has a relatively open structure, suspended solids could be passed without clogging, whereas activated carbon requires that streams be clarified before processing.[4] The electromagnets in an HGMS system can be cycled rapidly on and off to regenerate the filter, while activated carbon requires a time-consuming thermal treatment that can degrade the porous structure.[5] Finally, the high partition coefficient in the polymer shell means that effective separations can be achieved with relatively low concentrations of particles. For example, 1 wt% 8/8 particles (0.55 vol% on a dry basis) added to a contaminated water stream could reduce the free *o*-dichlorobenzene concentration by an order of magnitude.

## 6.3 Future Research Directions

Future research on these magnetic fluids should focus primarily on the need for particles with higher permanent capture efficiencies in the HGMS column. Our preliminary study showed that the fraction of permanently captured particles could be increased from approximately 10% to 50% by mixing high molecular weight PAA homopolymer with the graft copolymer during particle precipitation. The long-chain PAA acted as a crosslinking agent that led to the formation of small aggregates that were easier to capture. Aggregate formation was a strong function of the PAA molecular weight and future studies could examine this effect in more detail. Another alternative is to synthesize graft copolymers with extremely long PAA backbones. These long graft copolymers could be more successful at forming small aggregates than the mixture of low molecular weight graft copolymer and high molecular weight PAA used in our study. One limitation of synthesizing graft copolymers with long PAA backbones is that the extremely high viscosity of the melts makes the reaction difficult to carry out in the bulk. Activator chemistry, such as 1,3-dicyclohexylcarbodiimide (DCC) coupling could be used instead to drive the amidation reaction in an organic solvent.[6]

Another direction for future research is modification of the magnetic separation process. Development of a magnetic separation process capable of removing individual nanoparticles from water would allow a process to take full advantage of the high surface areas of these particles. Continuous magnetic separation processes based on field-flow fractionation techniques[7-9] have the potential to perform better than conventional HGMS, as diffusion makes techniques based on static trapping of nanoparticles extremely difficult. Feasible processes could involve staged magnetic separators with recycle loops as these processes generally involve physically splitting a magnetic fluid into rich and lean streams based on a particle concentration gradient that occurs in a magnetic field gradient.[7,8] Simulations of particle capture would be useful for rational design of processes for individual nanoparticle capture.

Other separation processes that currently face significant limitations are another potential area of future research on magnetic fluid-based separation schemes. The nature of magnetic fluids makes them particularly appropriate for systems where the target solute is present in very low concentration (i.e. less than 0.1 wt%) but either must be further reduced for environmental reasons or is sufficiently valuable to make recovery economically feasible. An example of this latter case is recovery of biological compounds such as proteins[1] or drugs from fermentation media. Another possible environmental application is the removal of sulfur compounds from fuel oils, which are often present in the 500-1000 ppm range but must be reduced to under 40 ppm in some states. The primary challenge in designing new magnetic fluids for these applications is obtaining a stabilizing layer that can provide stability in the dispersion medium but is also tailored to extract the target solute.

## 6.4 Bibliography

(1) Bucak, S.; Jones, D. J.; Laibinis, P. E.; Hatton, T. A. Protein Separations using Colloidal Magnetic Nanoparticles. *Biotechnol. Prog.* **2003**, *19*, 477-484.

(2) Ortiz-Del Castillo, J. R.; Guerrero-Medina, G.; Lopez-Toledo, J.; Rocha, J. A. Design of Steam-Stripping Columns for Removal of Volatile Organic Compounds from Water using Random and Structured Packings. *Ind. Eng. Chem. Res.* **2000**, *39*, 731-739.

(3) Dvorak, B. I.; Lawler, D. F.; Speitel, G. E. Niche for Steam Stripping in Treating Dilute SOC-Contaminated Waters. *J. Environ. Eng.* **1996,** *122*, 871-874.

(4) Smith, J. E. J.; Hegg, B. A.; Renner, R. C.; Bender, J. H. *Upgrading Existing or Designing New Drinking Water Treatment Facilities*; Noyes Data Corporation: Park Ridge, NJ, 1991; Vol. 198.

(5) Snoeyink, V. L.; Summers, R. S. Adsorption of Organic Compounds. In *Water Quality and Treatment*, 5th ed.; Letterman, R. D., Ed.; McGraw-Hill: New York, 1999.

(6) Wang, K. T.; Iliopoulos, I.; Audebert, R. Viscometric Behavior of Hydrophobically Modified Poly(Sodium Acrylate). *Polym. Bull.* **1988,** *20*, 577-582.

(7) Gerber, R. Magnetic Filtration of Ultra-Fine Particles. *IEEE Trans. Magn.* **1984,** *20*, 1159-1164.

(8) Kelland, D. R. Magnetic Separation of Nanoparticles. *IEEE Trans. Magn.* **1998,** *34*, 2123-2125.

(9) Tsukamoto, O.; Ohizumi, T.; Ohara, T.; Mori, S.; Wada, Y. Feasibility Study on Separation of Several Tens Nanometer-Scale Particles by Magnetic Field-Flow-Fractionation Technique Using Superconducting Magnet. *IEEE Trans. Appl. Supercond.* **1995,** *5*, 311-314.

# THESIS PROCESSING SLIP

**FIXED FIELD:** ill. _____ name _____

index _____ biblio _____

► **COPIES:** (Archives) Aero Dewey Barker Hum

Lindgren Music Rotch (Science) Sche-Ploug

**TITLE VARIES:** ► ☐ _____

_____

_____

**NAME VARIES:** ► ☐ / Duncan)

_____

**IMPRINT:** **(COPYRIGHT)** _____

_____

► **COLLATION:** _____

_____

► **ADD: DEGREE:** _____ ► **DEPT.:** _____

► **ADD: DEGREE:** _____ ► **DEPT.:** _____

**SUPERVISORS:** _____

_____

**NOTES:**

cat'r: date:

page:

► **DEPT:** Chem. Eng ▶ 340

► **YEAR:** 2003 ► **DEGREE:** Ph. D.

► **NAME:** MOEBER, Geoffrey D.